

Aihong Tang, Ph.D., May, 2002

NUCLEAR PHYSICS

ELLIPTIC FLOW IN AU + AU COLLISIONS AT  $\sqrt{s_{NN}} = 130$  GEV (113 pp.)

Director of Dissertation: Declan Keane

Elliptic flow holds much promise for studying the early-time thermalization attained in ultrarelativistic nuclear collisions. A related open issue is the extent to which hydrodynamic models and calculations which approach the low density (dilute gas) limit can describe the data. Among the effects that can complicate the interpretation of elliptic flow measurements are azimuthal correlations that are unrelated to the reaction plane (non-flow correlations). This study presents data from the STAR experiment at Brookhaven's Relativistic Heavy Ion Collider (RHIC) and contrasts two- and four-particle correlation results in order to estimate and eliminate these non-flow effects. It is found that four-particle correlation analyses can reliably separate flow and non-flow correlation signals, and the latter account for on average about 15% of the observed second-harmonic azimuthal correlation, with the largest relative contribution for the most peripheral and the most central collisions. The results are also corrected for the effect of flow variations within centrality bins. This effect is negligible for all but the most central multiplicity bin, where the correction to the elliptic flow is about a factor of two. A simple new method for two-particle flow analysis based on scalar products is described.

This work presents an investigation of  $v_2/\epsilon$  — elliptic flow in various centrality bins, divided by the initial spatial eccentricity for those centralities. Mapping centrality onto a scale of charged particle density enables us to study a broad range of this quantity, from peripheral collisions at a few GeV/nucleon, through CERN/SPS energies, and ending with central RHIC collisions. Within errors, the STAR data follow a smooth trend and show no evidence of predicted phase transition signatures.

The pattern of  $v_2/\epsilon$  being roughly proportional to particle density continues over the density range explored at RHIC, which is consistent with a general category of models which approximate the low density limit as opposed to the hydrodynamic limit. On the other hand,  $v_2/\epsilon$  at STAR is consistent with having just reached the hydrodynamic limit for the most central collisions. The present data contain no hint of the expected saturation of  $v_2/\epsilon$  at the hydrodynamic limit.

ELLIPTIC FLOW IN AU + AU COLLISIONS AT  $\sqrt{s_{NN}} = 130$  GEV

A dissertation submitted to  
Kent State University in partial  
fulfillment of the requirements for the  
degree of Doctor of Philosophy

by

Aihong Tang

May, 2002

Dissertation written by

Aihong Tang

B.S., Beijing University of Science and Technology, 1992

Ph.D., Kent State University, 2002

Approved by

\_\_\_\_\_, Chair, Doctoral Dissertation Committee

\_\_\_\_\_, Members, Doctoral Dissertation Committee

\_\_\_\_\_

\_\_\_\_\_

\_\_\_\_\_

Accepted by

\_\_\_\_\_, Chair, Department of Physics

\_\_\_\_\_, Dean, College of Arts and Sciences

## Table of Contents

List of Figures . . . . .	vii
List of Tables . . . . .	xi
<b>Acknowledgements</b> . . . . .	xii
<b>1 Introduction</b> . . . . .	1
<b>2 Probes for QGP</b> . . . . .	5
2.1 Direct photons and dileptons . . . . .	5
2.2 Charmonium suppression . . . . .	6
2.3 The Hanbury-Brown-Twiss effect . . . . .	6
2.4 Strangeness enhancement . . . . .	7
2.5 Thermodynamic variables . . . . .	8
2.6 High $p_t$ probes . . . . .	8
2.7 Anisotropic flow . . . . .	9
<b>3 Hydrodynamics of QGP</b> . . . . .	10
3.1 Basic parameters in the hydrodynamical description of QGP . . . . .	10
3.2 The energy-momentum tensor $T^{\mu\nu}$ . . . . .	10
3.3 The dynamics . . . . .	10
3.4 Summary . . . . .	12
<b>4 Introduction to Anisotropic Flow</b> . . . . .	13
4.1 Introduction . . . . .	13

4.2	Directed flow (Sideward flow)	14
4.3	Elliptic flow	19
4.3.1	Introduction	19
4.3.2	Centrality dependence of elliptic flow	19
4.3.3	Energy dependence	20
4.3.4	Elliptic flow from different particle species	22
<b>5</b>	<b>STAR Experiment</b>	<b>25</b>
5.1	The layout of the STAR experiment	25
5.2	STAR TPC	25
5.3	Ring Image Čerenkov Detector	32
5.4	Trigger	34
<b>6</b>	<b><math>dE/dx</math> Calibration</b>	<b>38</b>
6.1	Introduction	38
6.1.1	Bethe-Bloch function	38
6.1.2	Energy loss distribution	38
6.2	Calibration	41
6.2.1	Pad row variation	41
6.2.2	Drift distance dependence	42
6.2.3	$dx$ dependence	42
6.3	Truncation ratio optimization	43
6.4	Improvement on $dE/dx$ resolution	44
<b>7</b>	<b>Purity PID</b>	<b>46</b>
7.1	Purity	46
7.2	Bethe-Bloch calibration	46

7.3	Determine <i>sigma</i> of a single trial . . . . .	47
7.4	Multi-Gaussian fitting . . . . .	49
7.5	Electron contamination . . . . .	51
7.6	Purity result . . . . .	52
<b>8</b>	<b>Elliptic Flow</b> . . . . .	<b>54</b>
8.1	Introduction . . . . .	54
8.2	Two-particle correlation methods . . . . .	57
8.2.1	Correlation between flow angles from different subevents. Estimate of non-flow effects. . . . .	57
8.2.2	Weighting . . . . .	61
8.2.3	Scalar product flow analysis . . . . .	61
8.3	Four-particle correlations . . . . .	64
8.3.1	Motivation for Cumulants . . . . .	64
8.3.2	Four-subevent method . . . . .	67
8.3.3	Cumulant and generating function . . . . .	68
8.3.4	Simulations . . . . .	70
8.3.5	Results from STAR . . . . .	74
8.4	Elliptic flow fluctuations . . . . .	80
8.5	The centrality dependence of elliptic flow . . . . .	84
<b>9</b>	<b>Summary and Outlook</b> . . . . .	<b>89</b>
	References . . . . .	92
<b>A</b>	<b>The Quark Model</b> . . . . .	<b>99</b>
<b>B</b>	<b>Kinematic Variables</b> . . . . .	<b>102</b>

<b>C</b>	<b>Practical Guide to Cumulant Method in Flow Analysis</b> . . . . .	104
C.1	Integrated flow . . . . .	104
C.2	Differential flow . . . . .	105
<b>D</b>	<b>Author's Contributions to Collaborative Research</b> . . . . .	108
<b>E</b>	<b>List of Publications</b> . . . . .	110
<b>F</b>	<b>The STAR Collaboration</b> . . . . .	112



## List of Figures

1.1	Phase diagram of nuclear matter. . . . .	1
1.2	Space-time diagram of Heavy Ion Collision. . . . .	2
1.3	Reaction plane. . . . .	3
4.1	Major types of azimuthal anisotropies. . . . .	14
4.2	Schematic behavior of the magnitudes of directed flow and elliptic flow as a function of the bombarding kinetic energy per nucleon in the laboratory frame. . . . .	16
4.3	Reduction of the directed flow due to phase transition. . . . .	17
4.4	Results of transverse flow analyses, $v_1$ vs. $y/y_{cm}$ at 158A GeV show strong soften- ing. . . . .	18
4.5	Elliptic flow as a function of impact parameter in LDL limit and Hydro limit. . . . .	21
4.6	Elliptic flow as a function of beam energy per nucleon. . . . .	22
4.7	Elliptic flow as a function of $p_t$ from various particle species. . . . .	23
5.1	The layout of the STAR experiment. . . . .	26
5.2	Perspective view of the STAR Time Projection Chamber. . . . .	27
5.3	TPC pad plane layout. . . . .	29
5.4	Drift lines in a typical MWPC. . . . .	30
5.5	Equipotentials from drift volume to pad plane. . . . .	31
5.6	Schematic cross section of the RICH detector module. . . . .	33
5.7	Čerenkov radiation. . . . .	33
5.8	Central Trigger Barrel. . . . .	35
5.9	Zero Degree Calorimeters. . . . .	36

5.10	Correlation between pulse heights of Zero Degree Calorimeters and Central Trigger	
	Barrel in a minimum bias trigger. . . . .	36
6.1	Ionization energy loss of a function of $\beta\gamma$ . . . . .	39
6.2	Landau distribution. . . . .	40
6.3	$dE/dx$ as a function of index of pad row for sector # 2. . . . .	41
6.4	$dE/dx$ as a function of $z$ coordinate in TPC. . . . .	42
6.5	$dE/dx$ as a function of $dx$ in TPC. . . . .	43
6.6	The separation power as a function of truncation ratio. . . . .	44
6.7	$\sigma_{(dE/dx)/\langle dE/dx \rangle}$ versus number of points used in $dE/dx$ calculation. . . . .	45
7.1	$dE/dx$ versus $\beta\gamma$ . . . . .	47
7.2	$dE/dx$ versus momentum. . . . .	48
7.3	Multi-Gaussian fitting of $dE/dx$ for different momentum regions. . . . .	50
7.4	Amplitudes at the band center as a function of momentum. . . . .	51
7.5	$dE/dx$ versus $p$ for particles with identities assigned according to maximum purity .	52
8.1	Correlation between the event plane angles determined from pairs of subevents partitioned randomly , partitioned with opposite sign of pseudorapidity and partitioned with opposite sign of charge.The correlation is plotted as a function of centrality. .	59
8.2	The event plane resolution for full events as a function of centrality. . . . .	60
8.3	Elliptic flow signal $v_2$ as a function of centrality, from study of the correlation between particle pairs consisting of randomly chosen particles, particles with opposite sign of charge, particles with the same sign of charge and particles with opposite sign of pseudorapidity. . . . .	60
8.4	compare $p_t$ weighted $v_2$ with unit weighted $v_2$ in event plane method. . . . .	62
8.5	compare scalar product method with event plane method. . . . .	63

8.6	Reconstructed $v_2$ from the conventional method, from the 2nd-order cumulant method, and from the 4th-order cumulant method, for simulated events as a function of number of embedded back-to-back track pairs. . . . .	71
8.7	Reconstructed $v_2$ from the conventional method, from the 2nd-order cumulant method, and from the 4th-order cumulant method, for simulated events as a function of number of embedded back-to-back track pairs. . . . .	72
8.8	Elliptic flow from the conventional method, from the 2nd-order cumulant method, and from the 4th-order cumulant method, for simulated events as a function of azimuthal angle between the two tracks in each of 50 embedded pairs per event, with the 50 pairs each having random orientation relative to the event plane. . . . .	72
8.9	Elliptic flow from the conventional method, and from the 2nd-order, 4th-order, and 6th-order cumulant methods. . . . .	73
8.10	Measured elliptic flow versus centrality for Au + Au at $\sqrt{s_{NN}} = 130$ GeV. . . . .	74
8.11	Reconstructed $v_2$ versus pseudorapidity from the conventional method, from the 2nd-order cumulant method, and from the 4th-order cumulant method, in eight centrality bins. . . . .	76
8.12	Reconstructed $v_2$ versus $p_t$ from the conventional method, from the 2nd-order cumulant method, and from the 4th-order cumulant method, in eight centrality bins. . . . .	77
8.13	Elliptic flow versus pseudorapidity from the conventional method, from the 2nd-order cumulant method, from quarter-events, and from the 4th-order cumulant method, averaged over all centralities from bin 2 through 7 . . . . .	78
8.14	Elliptic flow versus transverse momentum from the conventional method, from the 2nd-order cumulant method, from quarter-events, and from the 4th-order cumulant method, averaged over all centralities from bin 2 through 7 . . . . .	79

8.15	The ratio of $v_2$ from the 4th-order cumulant divided by $v_2$ from the conventional method as a function of $p_t$ . . . . .	79
8.16	The ratio of $v_2$ from quarter-events divided by the conventional $v_2$ as a function of $p_t$ . . . . .	80
8.17	Measured $v_2$ from 4th-order cumulants versus centrality with $p_t$ weighting and unit weighting. . . . .	81
8.18	$v_2$ as a function of impact parameter based on measured data, using HIJING to infer the impact parameter. . . . .	83
8.19	$v_2/\epsilon$ as a function of charged particle density in Au + Au collisions. . . . .	86
A.1	Meson octet with $J^P = 0^-$ . . . . .	100
A.2	Baryon octet with $J^P = \frac{1}{2}^+$ . . . . .	100

## List of Tables

7.1	<i>sigma of a single trial</i> for different centralities. These numbers are for STAR P00hm data production. . . . .	49
7.2	<i>sigma of a single trial</i> for different centralities and different pseudorapidities. These numbers are for STAR P01he data production . . . . .	49
8.1	Tabulated values of observed charged particle multiplicity, centrality in terms of percent of total geometric cross section, impact parameter inferred from HIJING, the initial spatial anisotropy $\epsilon$ , and the final corrected elliptic flow based on 4th-order cumulants. . . . .	84
A.1	The six quark flavours and their masses . . . . .	99

## Acknowledgements

Personally, I would like to thank my family for their encouragement. Especially, I would like to thank my wife Yonghui Xie, for the sacrifice she's made in supporting of my Ph.D. work, for her patience and for her love.

Professionally, I extend my heartfelt thanks first of all to my advisor, Dr. Declan Keane, for his tremendous help covering from the overall guidance and constant encouragement of my Ph.D. research, to making sure my presentations going well. Declan is not only an advisor in physics but also a friend and a mentor in life. Thank you! My gratitude also goes to Art Poskanzer, Raimond Snellings and Sergei Voloshin, with whom I had stimulating discussions at numerous occasions which helped me understand the intricate details of flow physics in heavy ion collisions. It was a wonderful experience working with them. Special thanks to Nicolas Borghini, Jean-Yves Ollitrault, and Mai Dinh for helpful discussions and suggestions. Thanks are due to Nu Xu and Zhangbu Xu for discussions of various physics topics. Thanks to Richard Witt for his help on the particle identification part of this thesis.

Thanks to my pals for the joyfull time we had together at Brookhaven National Lab. They are, for example (in no particular order), Wensheng Deng, Fabrice Retiere, Hui Long, Kai Schweda, Matthew Lamont, Lee Barnby, Jinghua Fu, Eugene Yamamoto, Ian Johnson, Masashi Kaneta, Haibin Zhang, etc.

I would like to thank all my collaborators, there are hundreds of people who deserve acknowledgment for their part in making this study possible. Appendix F lists the STAR collaboration, whose immeasurable hard work over a decade resulted in the successful construction and operation of the STAR detector. Not listed in Appendix F are the hundreds of technicians, engineers, and other support personnel who were vital to the outcome of the physics program.

**Introduction**

It is believed that a Quark-Gluon Plasma (QGP)[1], a deconfined state of quarks (see Appendix A) and gluons, existed on the order of micro seconds after the Big Bang, when the universe was at a temperature of approximately 150 to 200 MeV (Fig.1.1). It is predicted that a hadron-quark phase transition, which is the same transition as happened at the very beginning of the universe but in the reverse direction, occurs in heavy-ion collisions at ultrarelativistic energies (Fig.1.2) .

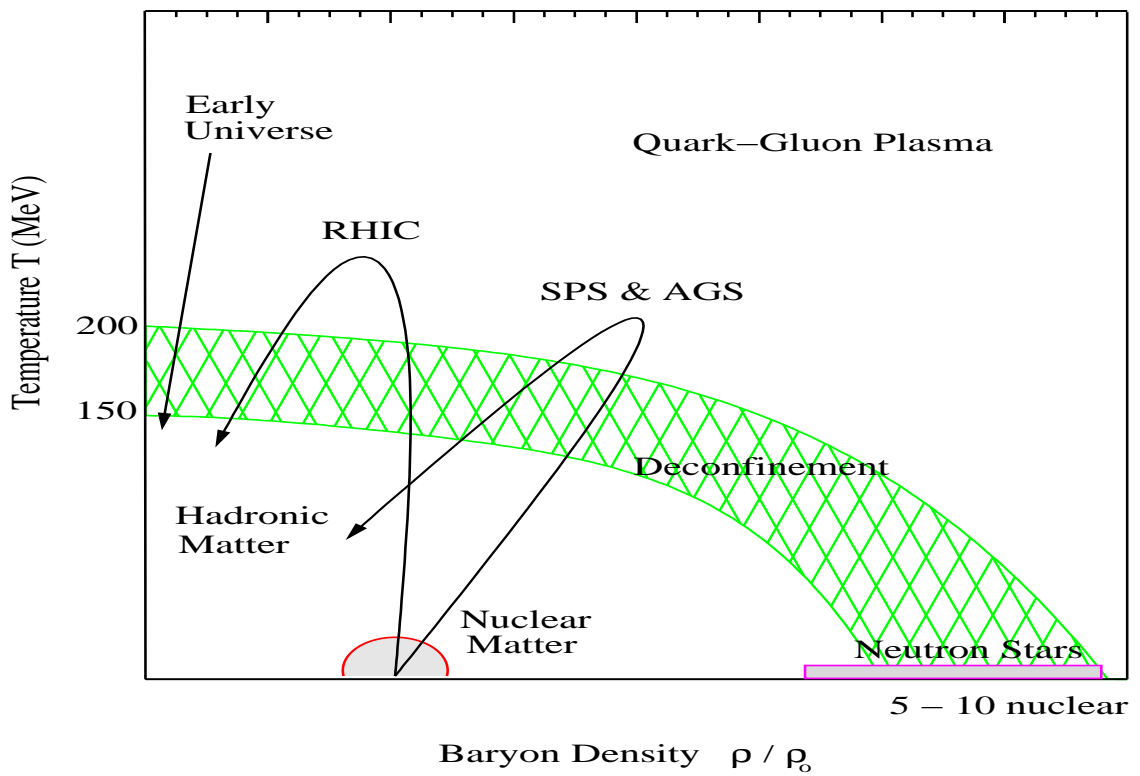


Figure 1.1: Phase diagram of nuclear matter.

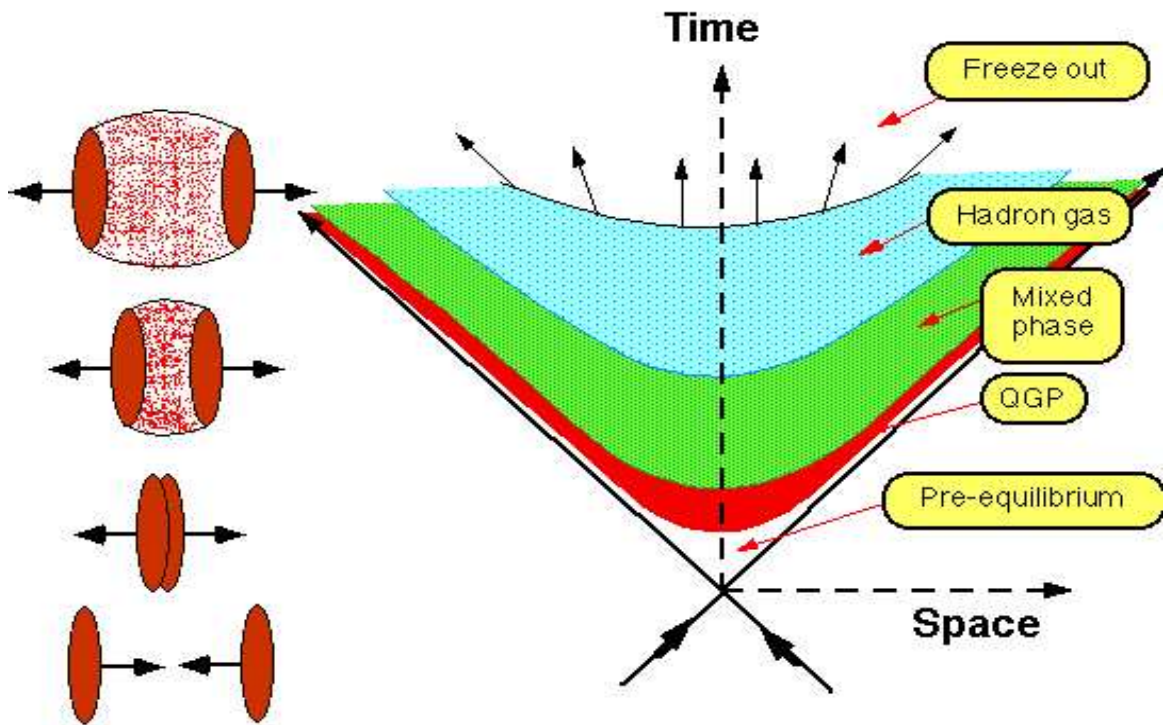


Figure 1.2: Space-time diagram of Heavy Ion Collision.

For the purpose of producing such an excited state of matter in the lab, the Relativistic Heavy-Ion Collider (RHIC) at Brookhaven National Laboratory has been constructed and is presently taking data. What we expect to get from RHIC is a better understanding of fundamental particles as well as the universe.

RHIC has been operating for physics experiments since June 2000. Reaction products are measured in a time projection chamber (TPC) in the STAR (Solenoidal Tracker At RHIC) detector, which is one of two large detectors along the RHIC ring. The TPC in STAR has been designed to focus primarily on hadronic observables and features a large acceptance for high precision tracking and momentum analysis at center of mass (c.m.) rapidity (see Appendix B for definition and discussion of rapidity). RHIC provides significantly increased particle production over any previous machine (thousands of particles produced).



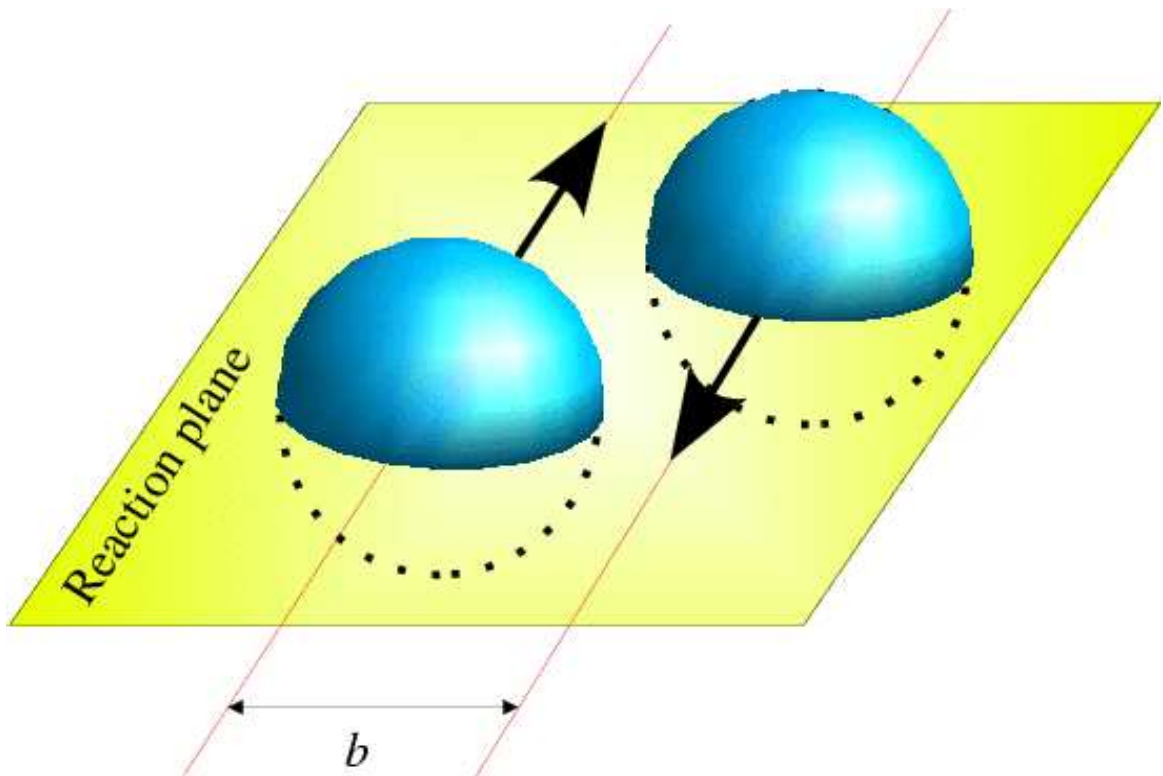


Figure 1.3: Reaction plane is defined by the initial direction of two colliding nuclei and the impact parameter ( $b$ ).

Anisotropic flow describes the azimuthal momentum distribution of particle emission with respect to the reaction plane (defined by the beam direction and the impact parameter ( $b$ ), see Fig. 1.3.) when nuclei collide at other than zero impact parameter (non-central collisions) [2, 3]. The initial spatial deformation due to geometry and the pressure developed early in the collision causes azimuthal momentum-space anisotropy. The measurement of flow can help provide insight into the evolution of this early stage of a relativistic heavy-ion collision. Elliptic flow is characterized by the second harmonic coefficient  $v_2$  of an azimuthal Fourier decomposition of the momentum distribution [4, 5, 6], and has been observed and extensively studied in Au + Au collisions from subrelativistic energies on up to RHIC. At incident energies above several GeV per nucleon, elliptic flow is inferred to be a relative enhancement of emission *in* the plane of the reaction, and provides

information about the early-time thermalization (local thermal equilibrium brought about by many rescatterings per particle during the system evolution) achieved in the collisions [7].

Sideward and elliptic flow are widely studied phenomena with a well-understood relationship to the event reaction plane [2, 3]. Generally speaking, large values of flow observables are considered signatures of hydrodynamic behavior, while smaller flow signals can have alternative explanations. Furthermore, there are several possible sources of azimuthal correlations which are unrelated to the reaction plane. Examples include correlations caused by resonance decays or dijets, by HBT (see section 2.3.) or Coulomb effects, by momentum conservation, etc. In the present type of study, it is not necessary to distinguish between the various possible effects in this overall category, and their combined effect is known as “non-flow” correlations.

Conventional flow analyses are equivalent to averaging over correlation observables constructed from pairs of particles, and there is no requirement for each event to contribute more than one pair. When such analyses are applied to relativistic nuclear collisions where particle multiplicities can be as high as a few thousand, the possible new information contained in higher multipliers remains untapped. A previous study of high-order flow effects focused on measuring the extent to which all fragments contribute to the observed flow signal [8]. Given that flow analyses based on pair correlations are sensitive to both flow and non-flow effects, the present work investigates correlation observables constructed from particle quadruplets, and it is confirmed that non-flow effects contribute at a negligible level to the quadruplet correlation.

## Probes for QGP

### 2.1 Direct photons and dileptons

Direct photons and dileptons are little affected by the later stages of the interaction, and they may provide a measure of the thermal radiation from a QGP. The most prominent processes for the creation of direct (thermal) photons in a QGP are  $q\bar{q} \rightarrow \gamma g$  (annihilation) and  $gq \rightarrow \gamma q$  (Compton scattering). The production rate and the momentum distribution of the photons depend on the momentum distributions of quarks, anti-quarks and gluons in the plasma.

The rapidity distribution of direct hard photons reflects the initial rapidity distribution of the produced mesons or directly the QGP[9]. If the hot thermal source is initially at rest and is accelerated by two longitudinal rarefaction waves propagating inwards with the velocity of sound, the photon rapidity distribution is strongly peaked around mid-rapidity. In contrast, a Bjorken-like boost invariant expansion [10] results in a roughly flat photon rapidity spectrum.

Another important piece of information can be obtained by studying the  $p_t$  distribution of direct photons. Hydrodynamical calculations show that the temperature of the photon spectrum is reduced in the event of a first order phase-transition to QGP[11, 12, 13].

Like direct photons, dileptons interact only electromagnetically so they can leave the hot and dense reaction zone undistorted. Dileptons may be created via quark-antiquark annihilation, or by a virtual photon. The parton cascade[14] and other models of an equilibration phase[15, 16] predict an excess of dileptons originating from an equilibrating QGP over the Drell-Yan background[17] in the mass range between 5 and 10 GeV. At lower invariant masses between 0.5 and 1 GeV, lepton pairs from hadronic sources are expected to dominate and provide information of possible medium modifications of hadrons at high density[18, 19]. The widths and positions of the  $\rho$ ,  $\omega$  and  $\phi$  peaks

in the lepton pair invariant mass spectrum are expected to be sensitive to medium-induced changes of the hadronic mass spectrum. A change in the  $K$ -meson mass would also affect the width of the  $\phi$  meson[20, 21]. A double  $\phi$  peak in the lepton pair spectrum would be indicative of a long-lived mixed phase[22, 23].

In fact, if the thermal fireball lives significantly longer than the  $\sim 1 \text{ fm}/c$  lifetime of the  $\rho$ -meson, then the strength of the  $\rho$ -meson in the lepton pair mass spectrum is expected to increase relative to the long-lived  $\omega$ . Thus, the  $\rho/\omega$  ratio could serve as a “clock” for the lifetime of the thermal fireball[24].

## 2.2 Charmonium suppression

The  $J/\psi$  has a very long lifetime and it decays into dileptons only when it is far from the collision zone. That makes  $J/\psi$  a good probe of the very early stages of the collisions.

In a quark-gluon plasma, the color charge of a quark is subject to screening due to the presence of quarks, anti-quarks, and gluons in the plasma. This phenomenon is called *Debye screening*, in analogy to the familiar Debye screening of an electric charge in condensed matter physics. If a  $J/\psi$  particle, which is a bound state of a charm quark  $c$  and a charm anti-quark  $\bar{c}$ , is placed in the plasma, the Debye screening will weaken the interaction between  $c$  and  $\bar{c}$ . Furthermore, the string tension between  $c$  and  $\bar{c}$  vanishes since quarks and gluons are deconfined. For the two combined reasons above, the production of  $J/\psi$  particles in QGP is predicted to be suppressed[25]. Less tightly bound excited states of the  $c\bar{c}$  system like  $\psi'$  and  $\chi_c$  are expected to become “dissolved” more easily, and thus their production will be suppressed even more than the  $J/\psi$ .

## 2.3 The Hanbury-Brown-Twiss effect

The probability of detecting two bosons at small relative momentum is affected by quantum mechanical interference between their wave functions. The interference effect depends on the

space-time extent of the boson-emitting source. This effect is commonly known as the *Hanbury-Brown-Twiss* (HBT) effect, which was first used by Hanbury-Brown and Twiss to measure the angular diameter of a star. The HBT measurements of particles emitted from the collision yields the longitudinal and transverse radii as well as the lifetime of the emitting source at the moment of thermal freeze out[26, 27, 28, 29, 30].

One can also study the correlation between non-identical particles. Such unlike-particle correlations also provide information about the space-time structure of the particle source and can even be used to determine the sequence of the emission of particles of different types[31].

A strong first order transition[29, 32] should result in a lower pressure, slower expansion and a long-lived evaporating droplet of QGP. Thus the space-time information from the HBT measurement is an important QGP signature.

#### 2.4 Strangeness enhancement

In proton-proton collisions, the production of particles containing strange quarks is strongly suppressed as compared to the production of particles with  $u$  and  $d$  quarks [33, 34], due to the higher mass of the  $s\bar{s}$  quark pair. The suppression increases with the strangeness content of the particles.

In the case of QGP, in which thermal equilibration and chemical equilibration is reached,  $s\bar{s}$  pairs can either be produced via the interactions of two gluons or  $q\bar{q}$  pairs. Leading order pQCD calculations suggest that the second process dominates only for  $\sqrt{s} \leq 0.6$  GeV[35]. The calculations also suggest that the time-scale of chemical equilibration of (anti-)strangeness due to gluon-gluon interaction is estimated to be about 3 to 6 fm/ $c$ , depending on the temperature of the plasma.

From the argument above, the yield of strange and multi-strange mesons and (anti-) baryons has been predicted to be strongly enhanced in the presence of a QGP as compared to a purely hadronic scenario at the same temperature[36, 37]. It has been shown[38, 39, 40] that an enhanced strangeness content cannot be destroyed nor generated by interactions during expansion

and freeze-out. However, the estimated equilibration times may not be sufficiently rapid to cause a saturation in the production of strange hadrons before QGP freeze-out.

## 2.5 Thermodynamic variables

In high energy collisions, a transverse kinetic energy distribution can be represented by a simple exponential function :  $e^{-m_T/T}$ . Here  $T$  is the slope parameter, and  $m_T$  is the transverse mass (see Appendix B). Kinetic equilibration is thought to be visible predominantly in the transverse degrees of freedom; therefore, transverse momentum or transverse mass distributions are used to extract temperatures from the spectral slopes. The magnitude of the slope parameter provides information on temperature (random motion in local rest frame) and collective transverse flow [41], and any deviation from the exponential distribution may signal new physics such as medium effect [42], etc.

It has been suggested that abnormal nuclear matter, e.g. a QGP, may be observed via a secondary, high temperature component in the particle spectra, or via a shoulder in the pion multiplicity distributions[43]. It has also been suggested that the equation of state (the energy density  $\epsilon$  vs. temperature  $T$ ) can be probed experimentally by plotting the mean transverse momentum  $\langle p_t \rangle$  vs. the rapidity density  $dN/dy$  or the transverse energy density  $dN/dE_T$ . If a phase transition occurs (i.e. a rapid change in the number of degrees of freedom), the saturation of  $\langle p_t \rangle$  during the mixed phase would cause a monotonically rising curve interrupted by a plateau. However, hydrodynamical studies[44, 45] show that the plateau could be washed out due to collective flow.

## 2.6 High $p_t$ probes

A fast charged particle in matter suffers energy loss either by excitation of the traversed medium or by radiation. Similar mechanisms happen for a fast quark or gluon traveling through dense matter.

The connection between energy loss of a quark and the color-dielectric polarizability of the medium can be established in analogy with the theory of electromagnetic energy loss[46, 47, 48]. Although radiation is a very efficient energy loss mechanism for relativistic particles, it is strongly

suppressed in a dense medium by the Landau-Pomeranchuk effect[49]. Adding the two contributions, the stopping power of a quark-gluon plasma is predicted to be higher than that of hadronic matter, and the high  $p_t$  spectra and elliptic flow is shown to be sensitive to initial gluon density [50].

## 2.7 Anisotropic flow

Anisotropic flow is the subject of many proposed signatures QGP formation. This dissertation focuses on elliptic flow, and details of the possible connections between flow and QGP are presented in later chapters.

## Chapter 3

### Hydrodynamics of QGP

#### 3.1 Basic parameters in the hydrodynamical description of QGP

Assuming that nuclear matter behaves as a perfect fluid, its evolution is determined by the equations of relativistic hydrodynamics until the mean free path of the particles is of the order of the dimensions of the system. The complete dynamics of a hydrodynamical system can be described by the energy density field  $\epsilon$ , the pressure field  $p$ , the temperature field  $T$ , and the 4-velocity field  $u^\mu = dx^\mu/d\tau$ , where  $x^\mu$  is the 4-vector coordinates and  $\tau$  is the proper time. The first three quantities above are related by the equation of state  $\epsilon = \epsilon(p, T)$ .

#### 3.2 The energy-momentum tensor $T^{\mu\nu}$

When a fluid element is at rest, the energy momentum tensor describes the energy density and the pressure. For example,  $T^{00} = \epsilon$ ,  $T^{11} =$  pressure in (2, 3) direction. In a frame in which the fluid element is moving with a 4-velocity  $u^\mu$ , the energy-momentum tensor is carrying out the transformation:

$$T^{\mu\nu} = (\epsilon + p)u^\mu u^\nu - g^{\mu\nu} p. \quad (3.1)$$

#### 3.3 The dynamics

From energy and momentum conservation, and neglecting viscosity and thermal conductivity, we have

$$\frac{\partial T_{\mu\nu}}{\partial x_\mu} = 0. \quad (3.2)$$



The equation 3.2 can be solved with certain simplifications assuming an equation of state (EOS). For example, if we consider only the longitudinal coordinate (beam direction in head-on heavy ion collisions) and the time coordinate, we can end up with (see Bjorken's hydrodynamic model [10])

$$\frac{\partial \epsilon}{\partial \tau} + \frac{(\epsilon + p)}{\tau} = 0. \quad (3.3)$$

In the case of an ideal gas of massless quarks and gluons, the energy density and the pressure are related by  $p = \epsilon/3$ , thus equation 3.3 becomes

$$\frac{d\epsilon}{d\tau} = -\frac{4}{3} \frac{\epsilon}{\tau}, \quad (3.4)$$

which has the solution

$$\frac{\epsilon(\tau)}{\epsilon(\tau_0)} = \frac{\epsilon(\tau)}{\epsilon_0} = \left(\frac{\tau_0}{\tau}\right)^{4/3}, \quad (3.5)$$

in which  $\tau_0$  and  $\epsilon_0$  are the proper time and energy density when the local equilibrium begins.

For the pressure we have

$$\frac{p(\tau)}{p(\tau_0)} = \left(\frac{\tau_0}{\tau}\right)^{4/3}. \quad (3.6)$$

For an ideal relativistic gas, the energy density and the pressure are proportional to  $T^4$ , where  $T$  now signifies temperature [51]. Then

$$\frac{T(\tau)}{T(\tau_0)} = \left(\frac{\tau_0}{\tau}\right)^{1/3}. \quad (3.7)$$

Other thermodynamic quantities such as entropy,  $S$ , can be obtained by [51]

$$dE = -pdV + TdS, \quad (3.8)$$

thus the entropy density is

$$s \equiv \frac{dS}{dV} = \frac{\epsilon + p}{T}. \quad (3.9)$$

From Eq. 3.5, 3.6 and 3.7, it follows that

$$\frac{s(\tau)}{s(\tau_0)} = \frac{\tau_0}{\tau}, \quad (3.10)$$

which means  $s(\tau)\tau$  is constant as a function of proper time.

As the volume element  $dV$  is given by  $dx_{\perp}^2 \tau dy$ , the last argument implies that

$$\frac{dS}{dx_{\perp}^2 dy} = \text{constant as a function of proper time}, \quad (3.11)$$

and it follows that

$$\frac{d}{d\tau} \left( \frac{dS}{dy} \right) = 0. \quad (3.12)$$

### 3.4 Summary

For a relativistic system in which local equilibrium is reached at  $\tau_0$  with initial energy density  $\epsilon_0$  and initial temperature  $T(\tau_0) \propto \epsilon_0^{1/4}$ , the energy density and the pressure decrease with proper time as  $\tau^{-4/3}$ , while the temperature drops as  $\tau^{-1/3}$ . The hydrodynamic motion of the fluid is characterized by a constant entropy per unit of rapidity.

## Introduction to Anisotropic Flow

### 4.1 Introduction

Anisotropic flow provides access to the *equation of state* of the hot and dense matter formed in the reaction zone since it is likely influenced by the the compression in the initial stages of the collision. It can help us understand processes such as thermalization, creation of the quark-gluon plasma, phase transitions, etc., and thus it is one of the important measurements in high energy heavy ion collisions and has attracted increased attention of both theoreticians and experimentalists[6].

Anisotropic flow is usually quantified by the Fourier coefficient of the particle distribution in emission azimuthal angle, measured with respect to the reaction plane, which can be written as:

$$E \frac{d^3 N}{d^3 p} = \frac{1}{2\pi} \frac{d^2 N}{p_t dp_t dy} \left(1 + \sum_{n=1}^{\infty} 2v_n \cos n\phi\right), \quad (4.1)$$

where the definition of  $p_t$  and  $y$  can be found in Appendix B,  $\phi$  denotes the angle between the particle and the (true) reaction plane (defined by the impact parameter and the beam axis) in momentum space. The sine terms which in general appear in Fourier expansions vanish due to the reflection symmetry with respect to the reaction plane. It follows that  $\langle \cos n\phi \rangle$  gives  $v_n$ :

$$\begin{aligned} \langle \cos n\phi \rangle &= \frac{\int_{-\pi}^{\pi} \cos n\phi E \frac{d^3 N}{d^3 p} d\phi}{\int_{-\pi}^{\pi} E \frac{d^3 N}{d^3 p} d\phi} \\ &= \frac{\int_{-\pi}^{\pi} \cos n\phi \left(1 + \sum_{m=1}^{\infty} 2v_m \cos m\phi\right) d\phi}{\int_{-\pi}^{\pi} \left(1 + \sum_{m=1}^{\infty} 2v_m \cos m\phi\right) d\phi} \\ &= \frac{\int_{-\pi}^{\pi} 2v_n \cos^2 n\phi d\phi}{2\pi} \\ &= v_n, \end{aligned} \quad (4.2)$$

where the orthogonality relation between Fourier coefficients  $\int_{-\pi}^{\pi} [\cos n\phi \cos m\phi]_{m \neq n} d\phi = 0$  has been used.

Anisotropic flow corresponding to the first two harmonics plays a very important role and we use special terms for them: directed flow and elliptic flow, respectively. The word “directed” (also called sideward flow) comes from the fact that such flow looks like a sideward bounce of the fragments away from each other in the plane of the reaction, and the word “elliptic” is due to the fact that the azimuthal distribution with non-zero second harmonic represents an ellipse (see Fig. 4.1).

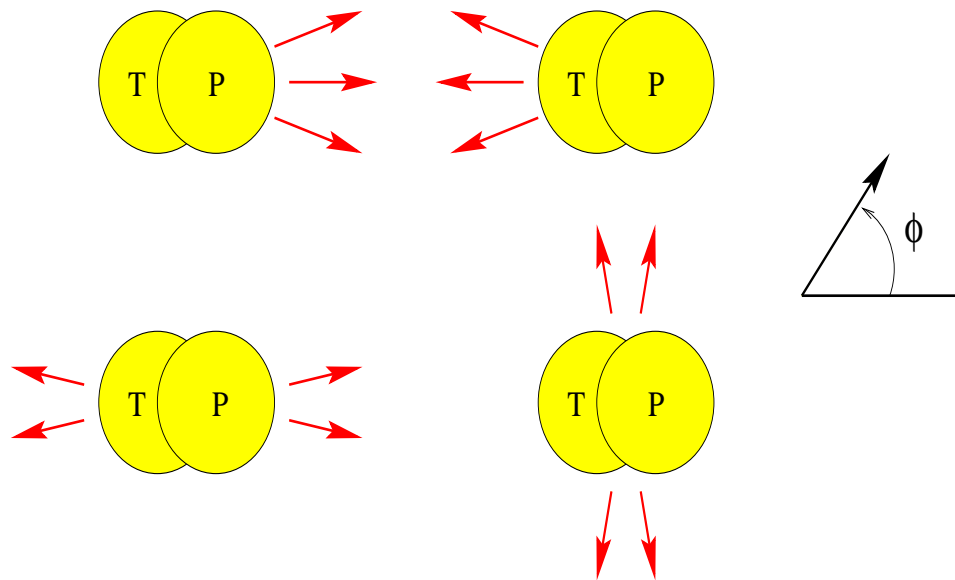


Figure 4.1: Major types of azimuthal anisotropies, viewed in the transverse plane. The target is denoted by T and the projectile by P. Top: Directed flow on the projectile side of midrapidity, positive (left) and negative (right). On the target side of midrapidity, the left and right figures are interchanged. Bottom: elliptic flow, in-plane or positive (left) and out-of-plane or negative (right). The plot is from [58].

#### 4.2 Directed flow (Sideward flow)

Directed flow most strongly affects particles at forward and backward rapidities. At low energies (below 100 A MeV), the interaction is dominated by the attractive nuclear mean field, which has two effects: first, projectile nucleons are deflected towards the target, resulting in negative directed flow [52]; second, the projectile and target form a rotating system, and the centrifugal force

emits particles in the rotation plane[53], producing in-plane elliptic flow[54, 55]. At higher energies, individual nucleon-nucleon collisions dominate over mean field effects. They produce a positive pressure, which deflects the projectile and target fragments away from each other in the center of mass frame (“bounce-off” and “sidesplash” effects [2]), resulting in positive directed flow. Furthermore, the participant nucleons, which are compressed in the region where the target and the projectile overlap (see Fig. 4.1), cannot escape in the reaction plane due to the presence of the spectator nucleons (“squeeze-out effect” [56]), producing out-of-plane negative elliptic flow.

At RHIC energies, the observed directed transverse flow pattern is established very early in the collision, since the affected particles quickly leave the central region where the transverse pressure acts. Its natural time scale is given by the passage time of the two colliding nuclei, which decreases at high collision energies; this causes a decrease at high collision energies (after an initial rise at low beam energies) of the directed flow (Fig. 4.2 ).

This decrease is amplified by a lack of thermalization during the earliest stage of the collision which prohibits fast enough buildup of transverse pressure and thus eventually invalidates the applicability of hydrodynamic concepts for calculating the directed flow. Such pre-equilibrium features may even cover up the phase transition signal in the excitation function of directed flow. It has been argued that the increased entropy density at the onset of QGP production should lead to a “softest point” in the nuclear equation of state [57]. In Ref[59], this softening was predicted to lead to a reduction of the directed flow, making the phase transition visible as a minimum in its beam energy dependence. A different manifestation of softening due to possible QGP formation was discussed by Csernai and Rohrich [60] (see Fig. 4.3).

The first evidence of directed flow at SPS was reported by the WA98 collaboration[61]. Further measurements were made by NA49[62] and CERES[63]. The strength of directed flow at SPS is significantly smaller than at AGS (Fig. 4.4), especially in the region not close to projectile and target rapidities.

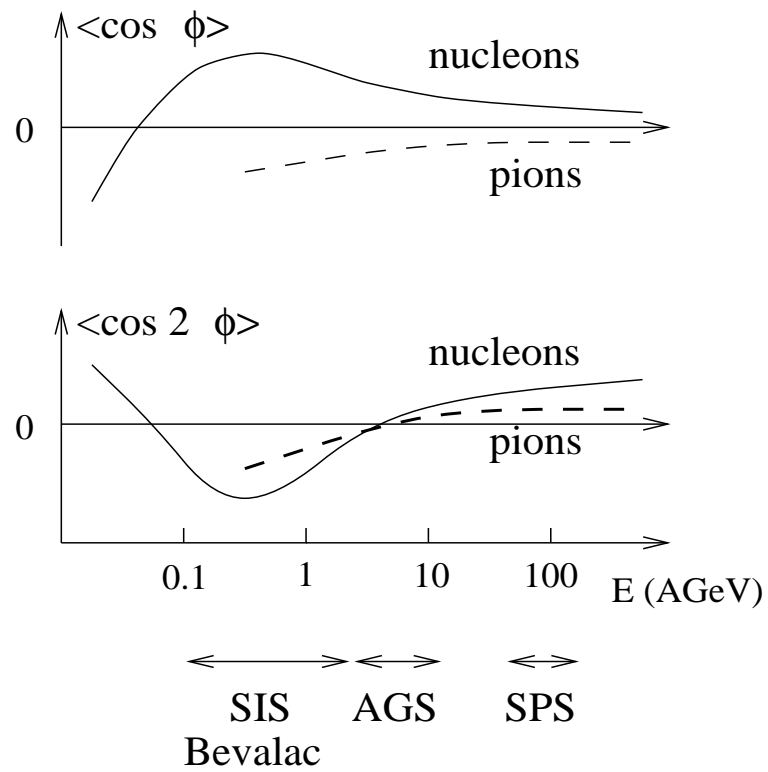


Figure 4.2: Schematic behavior of the magnitudes of directed flow (top) and elliptic flow (bottom) as a function of the bombarding kinetic energy per nucleon in the laboratory frame. Full lines: proton flow; dashed lines: pion flow. The plot is from [58].

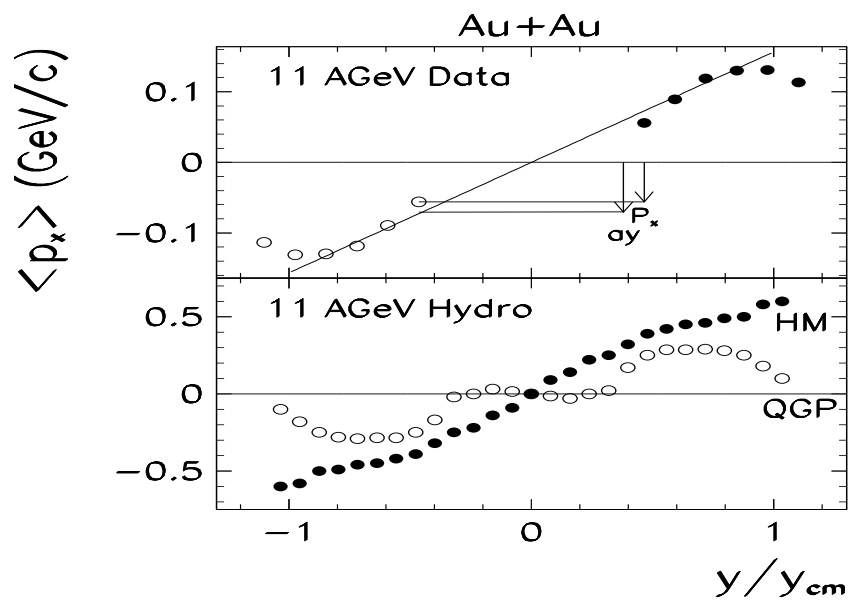


Figure 4.3: Upper part: Definition of the measure *softening*,  $S$ , describing the deviation of  $P_x(y)$  or  $v_1(y)$  from the straight line behavior,  $ay$ , around midrapidity.  $S$  is defined as  $|ay - P_x(y)|/|ay|$ . The lower figure shows a typical example for fluid dynamical calculations with Hadronic and QGP EOS. QGP leads to strong softening,  $\sim 100\%$ . The plot is from [60]

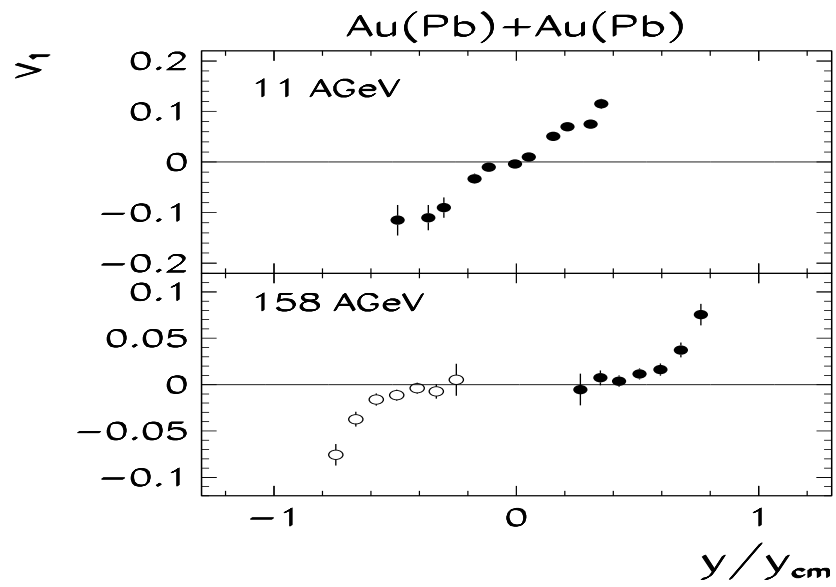


Figure 4.4: Results of transverse flow analyses,  $P_x$  vs.  $y/y_{cm}$  at 158A GeV results show strong softening. The plot is from [60]



Weak negative directed flow from pions has been observed in asymmetric collisions[64, 65, 66]. This is interpreted as a consequence of pion rescattering on spectator matter[67]. The same effect has been observed at AGS[68] and SPS[62].

### 4.3 Elliptic flow

#### 4.3.1 Introduction

Elliptic flow is caused by the initial geometric deformation of the reaction region in the transverse plane. At ultra-relativistic energies, the elliptic flow tends to act against its own cause by preferentially enhancing momenta along the direction of the smallest spatial extent of the source [69, 70]. Unlike directed flow, elliptic flow needs time for thermalization, thus it is generated later than directed flow.

Generally speaking, large values of collective flow are considered signatures of hydrodynamic behavior, while smaller flow signals can have alternative explanations.

#### 4.3.2 Centrality dependence of elliptic flow

The centrality dependence of elliptic flow is of special interest[71, 72]. In the low density limit(LDL), the mean free path is comparable to or larger than the system size, and the colliding nuclei resemble dilute gases. The final anisotropy in momentum space depends not only on the initial spatial eccentricity  $\epsilon$  (defined below), but also depends on the particle density, which affects the number of rescatterings. A more dilute system (less rescatterings) has more difficulty to transform spatial anisotropy to momentum anisotropy.

Thus in this limit, the final elliptic flow (see a more detailed formula in [74]) is

$$v_2 \propto \epsilon \frac{1}{S} \frac{dN}{dy}, \quad (4.3)$$

where  $dN/dy$  characterizes density in the longitudinal direction and  $S = \pi R_x R_y$  is the initial transverse area of the overlapping zone, with  $R_x^2 \equiv \langle x^2 \rangle$  and  $R_y^2 \equiv \langle y^2 \rangle$  describing the initial

geometrical dimensions of the system in the  $x$  and  $y$  directions, respectively. (The  $x - z$  axes lie in the reaction plane). The averages include a weighting with the number of collisions along the beam axis in a wounded nucleon [73] calculation. The spatial eccentricity is defined as

$$\epsilon = \frac{R_y^2 - R_x^2}{R_x^2 + R_y^2}, \quad (4.4)$$

and is roughly proportional to the impact parameter over a wide range.

As follows from Eq. 4.3, the elliptic flow increases with the particle density. Eventually, it saturates [58] at the hydro limit. In this region, the ratio of  $v_2$  to  $\epsilon$  is expected to be approximately constant [4] due to the complete thermalization (the mean free path is much less than the geometrical size of the system).

The value of  $(v_2/\epsilon)_{\text{hydro}}$  ranges from 0.27 – 0.35 according to Ollitrault's calculation [4], depending on the equation of state used (with or without QGP). More recent calculations by a different group [69, 75], by taking account of the effect of resonances, which tend to decrease the flow, give a smaller  $(v_2/\epsilon)_{\text{hydro}}$  centered on 0.195 in the case of energy densities of the order of those expected at RHIC.

Fig. 4.5[71] shows that the position of the maximum in  $v_2(b)$  shifts towards peripheral events as thermalization increases, i.e., moving from an LDL calculation to a hydrodynamic calculation.

### 4.3.3 Energy dependence

At AGS energies, the elliptic flow results from a competition between the early squeeze-out when compressed matter tries to move out in the unimpeded direction perpendicular to the reaction plane and the late-stage in-plane emission associated with the shape of the participant zone. The squeeze-out contribution to the elliptic flow depends, generally, on the pressure built-up early on, compared to the energy density, and on the passage time for the spectators. When the heated matter is exposed to the vacuum in the transverse direction, expansion happens more rapidly in the exposed

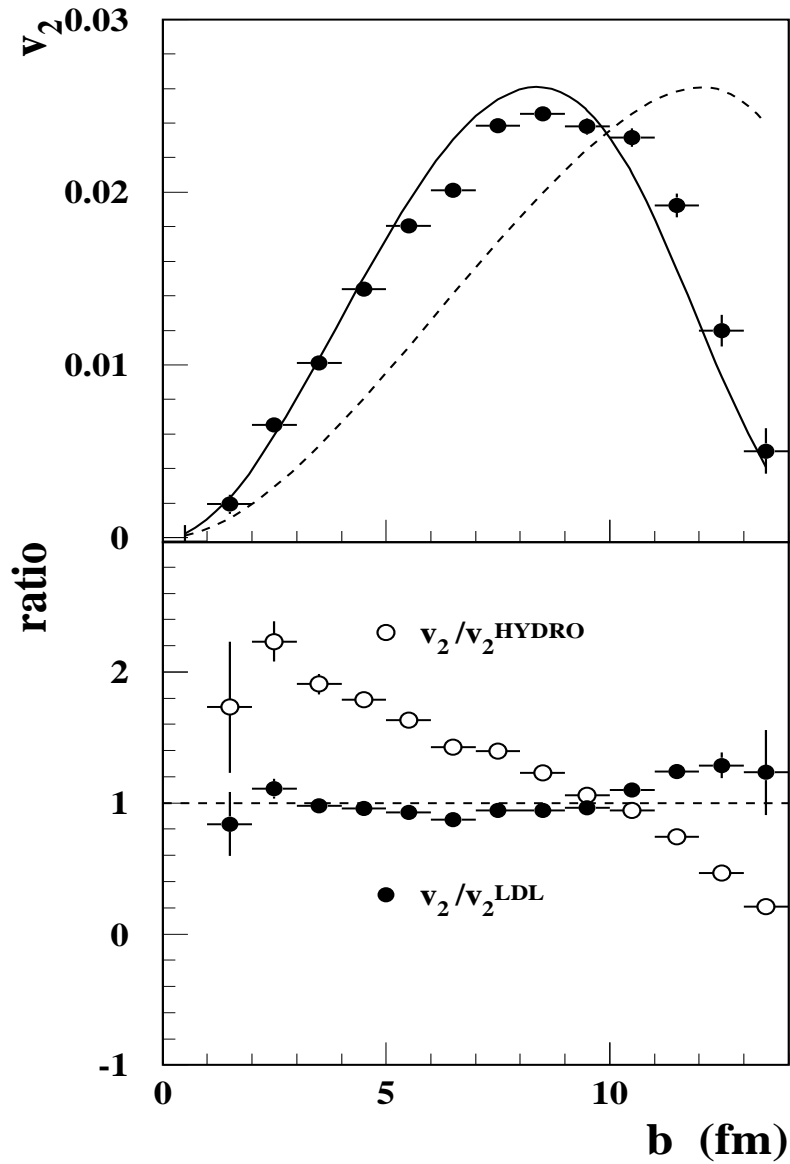


Figure 4.5: Top: comparison of elliptic flow,  $v_2$  as a function of impact parameter, for pions from RQMD version 2.3 (filled circles) with the dependence expected for the low-density limit (solid line) and that expected for the hydro limit (dashed line). Bottom: ratios of  $v_2/v_2^{LDL}$ , and  $v_2/v_2^{HYDRO}$ . The plot is from [71].

direction.

At relativistic energies, the Lorentz contracted spectators in the colliding nuclei pass by each other quickly (in a time of the order  $2R/\gamma$ , where  $R$  is the nuclear radius and  $\gamma$  is the Lorentz contraction factor). When this passage time is short enough, the in-plane (positive) component of elliptic flow dominates.

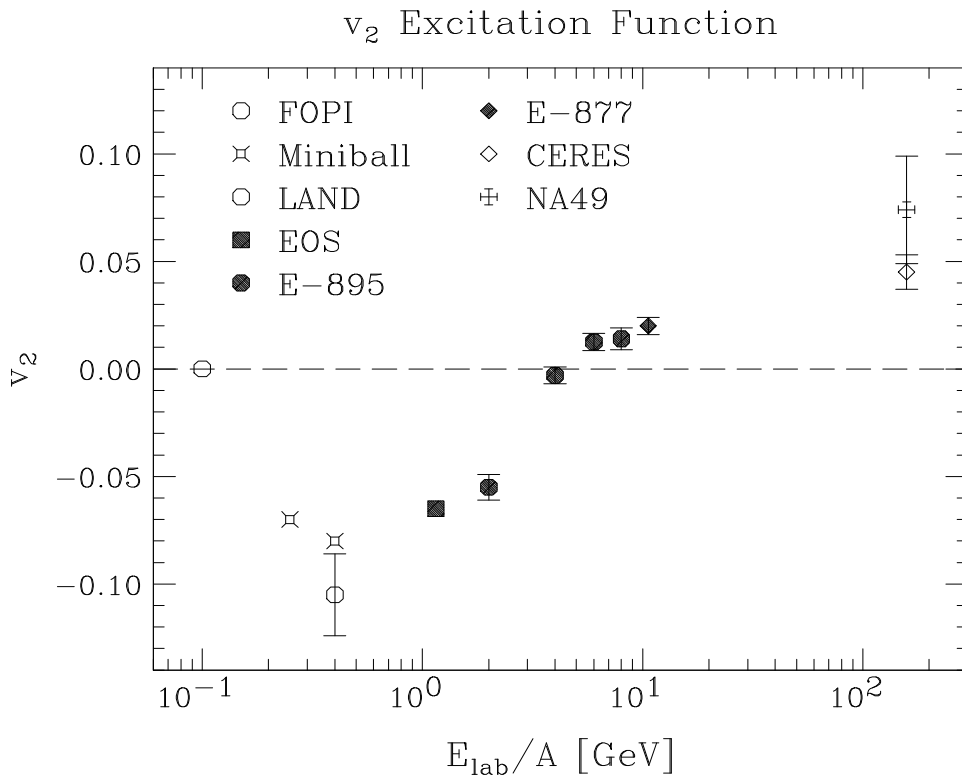


Figure 4.6: Elliptic flow as a function of beam energy per nucleon. The plot is from [76]

The measured  $v_2$  as a function of beam energy per nucleon is displayed in Fig. 4.6. Whether or not any changes in  $v_2$  with energy might be associated with a phase transition requires comparisons to model calculations to assess the magnitude of such possible changes.

#### 4.3.4 Elliptic flow from different particle species

Fig. 4.7 shows the differential momentum anisotropy  $v_2(p_t)$  for different hadron species in a thermal model incorporating a phase transition to QGP[75]. At a given value of  $p_t$ , the elliptic

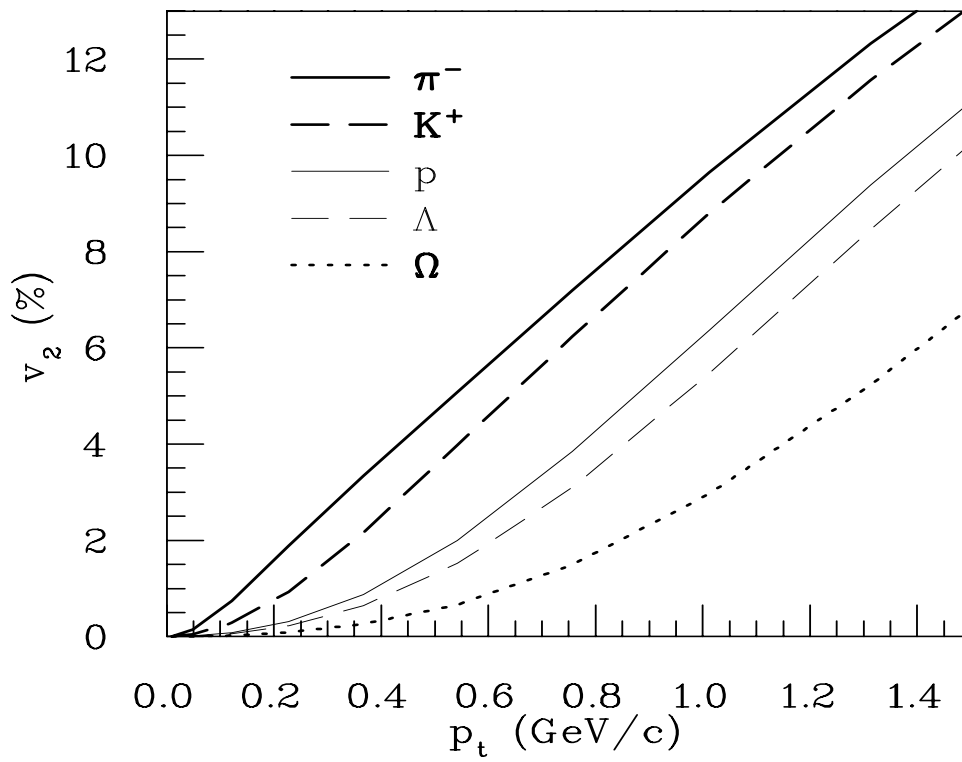


Figure 4.7:  $p_t$ -differential elliptic flow at midrapidity for various hadrons from minimum bias Au+Au collisions at  $\sqrt{s} = 130 A$  GeV for a thermal model with a QGP phase transition[77].

flow is seen to decrease with increasing particle mass. The pattern of the  $p_t$  differential elliptic flow decreasing with increasing particle mass comes from the energy conservation and radial flow, which shifts the  $p_t$ -distributions to larger value of  $p_t$ . If, as in the case of elliptic flow, the radial velocity is larger in  $x$  than in the  $y$  direction,  $|v_x| > |v_y|$ , if the energy distribution has to be isotropic, then having higher  $p_t$  in the  $x$  direction is compensated by having less particles going in the  $x$  direction, resulting in a decreased  $v_2$  for heavy particles, which have bigger  $p_t$ .

## STAR Experiment

### 5.1 The layout of the STAR experiment

The side-view of the STAR experiment is shown in Figure 5.1. The year-one configuration of the STAR experiment consist of a cylindrical Time Projection Chamber (TPC) 4m in diameter and 4m long covering  $|\eta| < 1.8$  and a Ring Imaging Čerenkov (RICH) detector covering  $|\eta| < 0.3$  and  $|\Delta\phi| < 20^\circ$ . The Central Trigger Barrel (CTB) and the Zero Degree Calorimeters (ZDC) together serve the purpose of triggering. The RICH and the ZDC are not shown in Figure 5.1, as the ZDC is far from the detector center and the RICH is under the TPC and obstructed from view in the figure. All components other than the ZDC were located in a 0.5 Tesla solenoidal magnetic field during year-one data taking.

### 5.2 STAR TPC

The TPC is a continuous tracking detector capable of handling events with thousands of tracks [78]. It determines the momenta of individual particles by tracing them through a solenoidal magnetic field and identifies many of them by making multiple energy loss measurements.

The major mechanical components of the TPC (Fig. 5.2) consist of the outer field cage (OFC), the inner field cage (IFC), the high voltage central membrane (CM) and some other support devices. Both end-caps have instrumented pad planes, with thin-gap, multi-wire proportional chambers (MWPC) in which the primary signal electrons are amplified by avalanche multiplication at the anode wires. Image charges are induced on an array of pads located behind the anode wires and are recorded as a function of time. For each track segment, the drift time provides one coordinate, while the induced signals on the pad arrays provide the coordinates in the plane of the MWPC.

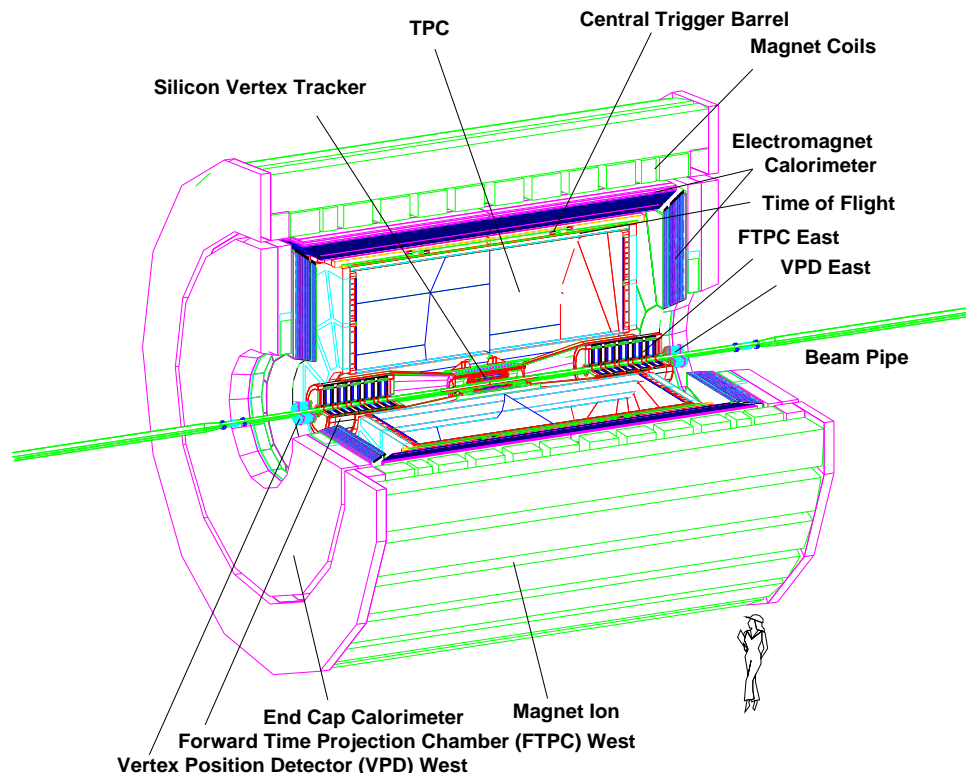


Figure 5.1: The layout of the STAR experiment.



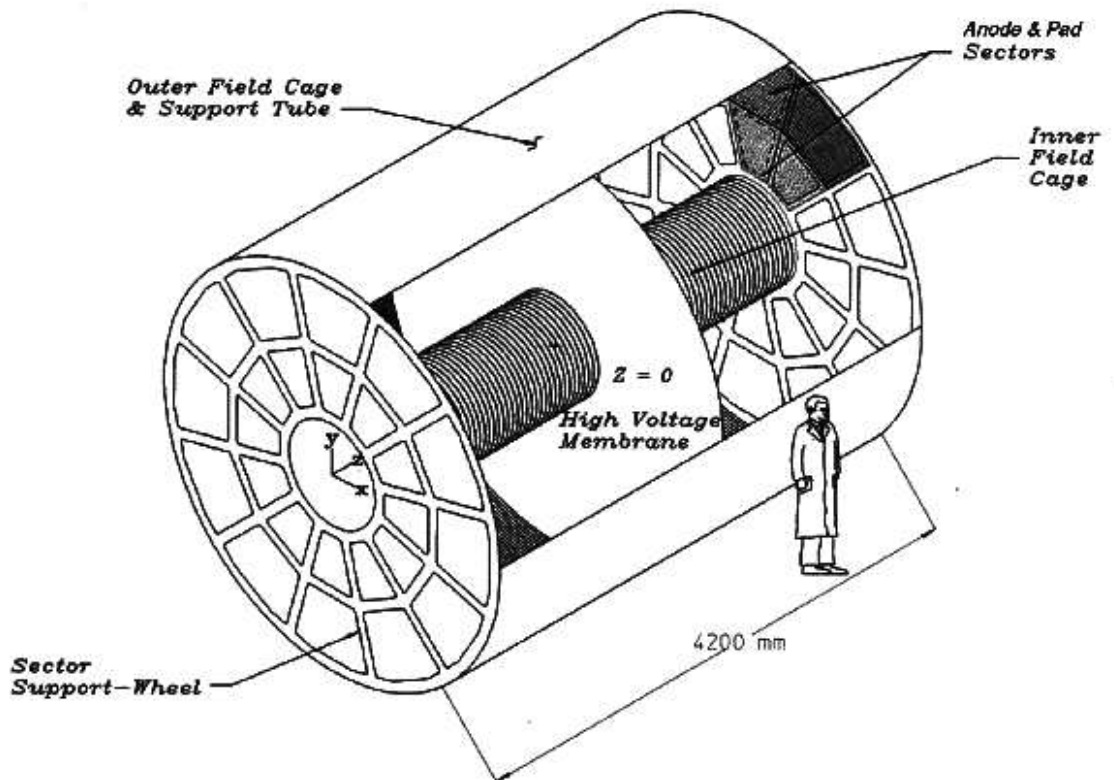


Figure 5.2: Perspective view of the STAR Time Projection Chamber.

The CM is located in the middle of the TPC and is held at high voltage ( $\sim 31$  kV for the year 2000). The OFC and the IFC define the active gas volume (see below), while their major function is to provide a nearly uniform electric field along the axis of the cylinder in which electrons drift to the anode plane, since any distortion in the field will result in a distortion of the recorded tracks.

The TPC is filled with a mixture of 90% Argon and 10% Methane gas. When a charged particle traverses the TPC volume, it ionizes gas atoms every few tenths of a millimeter along its path and leaves behind a trail of electrons. The ionization energy is supplied by the kinetic energy of the charged particle and is very small, typically a few keV per cm of gas under normal conditions. The electron clusters then drift to the end-caps under the influence of the externally applied electric field. The time of arrival and location of each electron cluster is recorded.

The end-cap at both ends of the TPC has anode wires and pad planes that are organized into sectors. There are 12 sectors on each of the two endcaps (see Fig. 5.3), each sector consists of an *inner* sector and an *outer* sector. The inner sector has 1,750 pads, with dimension of 11.5 mm along the radial direction and 2.85 mm along the tangential direction, while the outer sector has 3,940 pads with dimension of 19.5 mm (radial) x 6.2 mm (tangential). The inner sector pads are smaller in order to improve two-track resolution. However, there would be no advantage in making these pads even smaller, because of the diffusion limit of the TPC. Combining the inner and outer sectors, there are a total of 5,690 pads per sector, which corresponds to a total of 136,560 pads for all 24 sectors.

The bottom panel of Fig. 5.3 shows a cross-section view of the MWPC on the pad plane. The MWPC consists of three planes of wires and the pad plane. The first two are the gating grid and the ground grid, which together define the drift region of the TPC. The third wire plane is the anode wire plane, and it is set to a high voltage to provide the necessary electric field to avalanche the electrons from the primary ionization. Underneath the anode wires is a set of readout pads, on which the amplified signal from the primary ionization is collected.

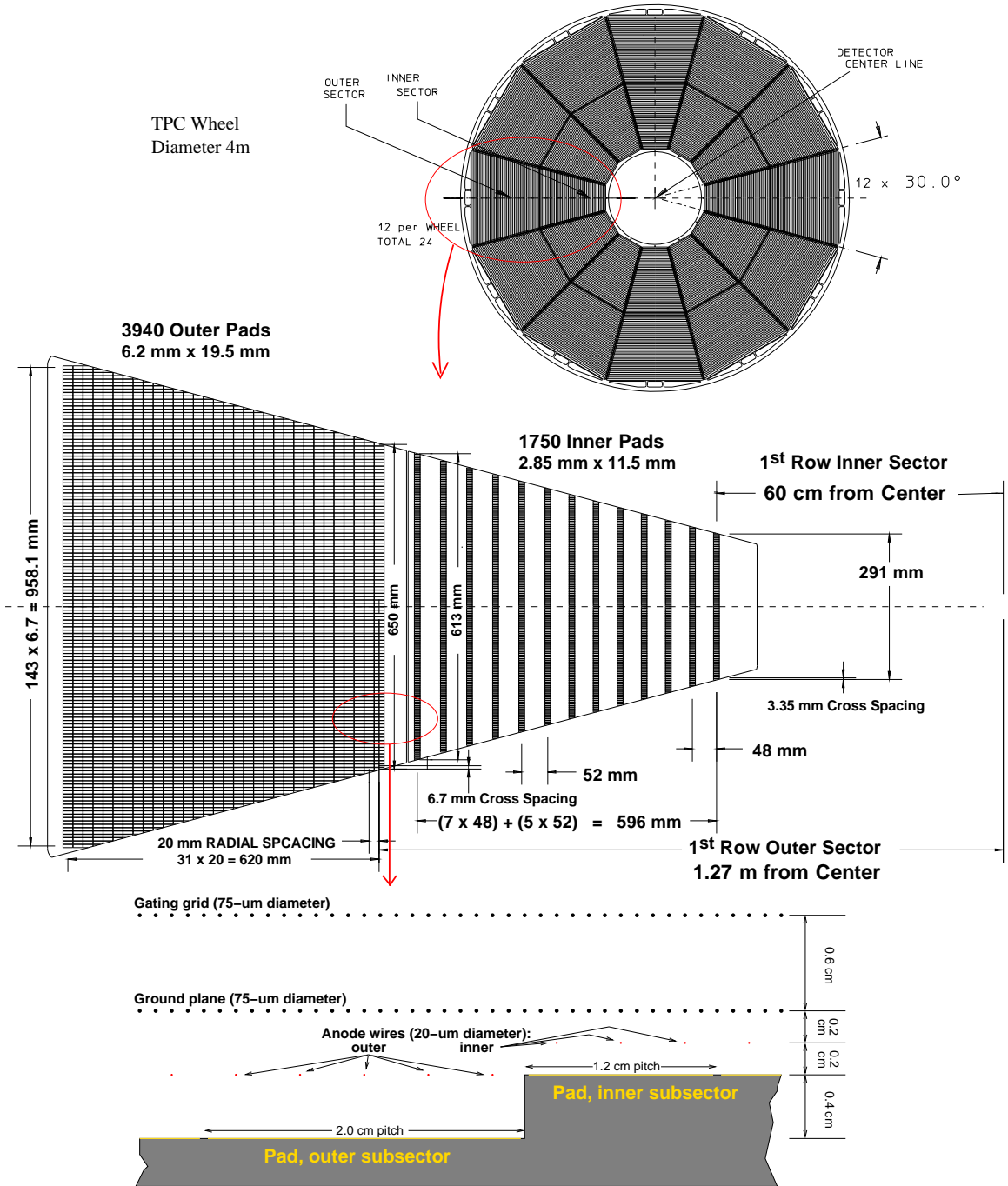


Figure 5.3: TPC pad plane layout. Top panel shows TPC endview of 24 sectors, the middle panel shows pad layout of one of them, the bottom panel shows the detail of wires above the pad plane.

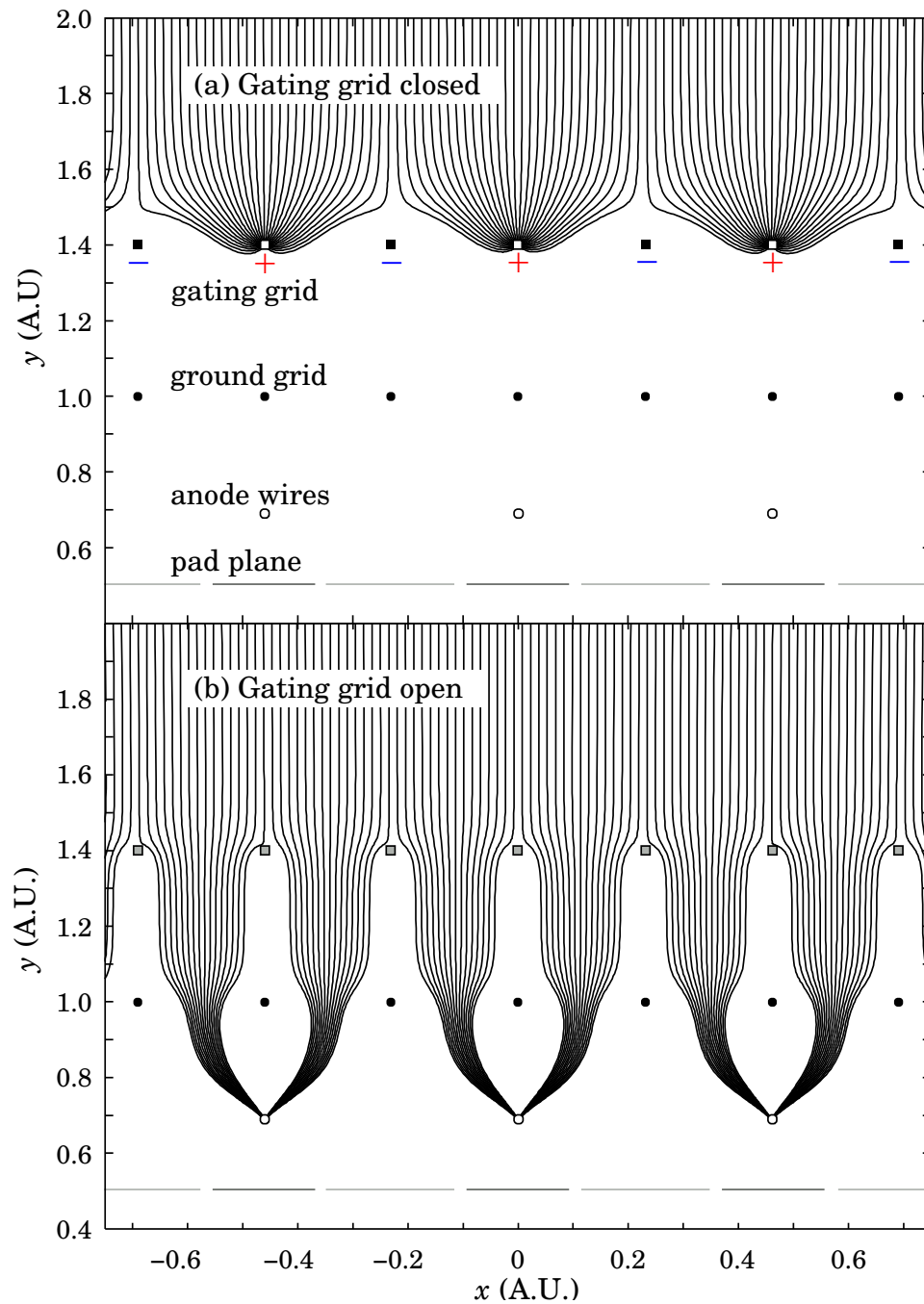


Figure 5.4: Drift lines in a typical MWPC. Drifting electrons are collected on the gating grid (a) until the gate is opened by a triggering event (b). The slow positive ions are blocked from entering the drift region by closing the gating grid after the electrons have drifted through. The motion of positive ions produced in the avalanche induces a signal on the segmented pad plane to provide precise measurements of ionization along the wire. This plot is from [85]

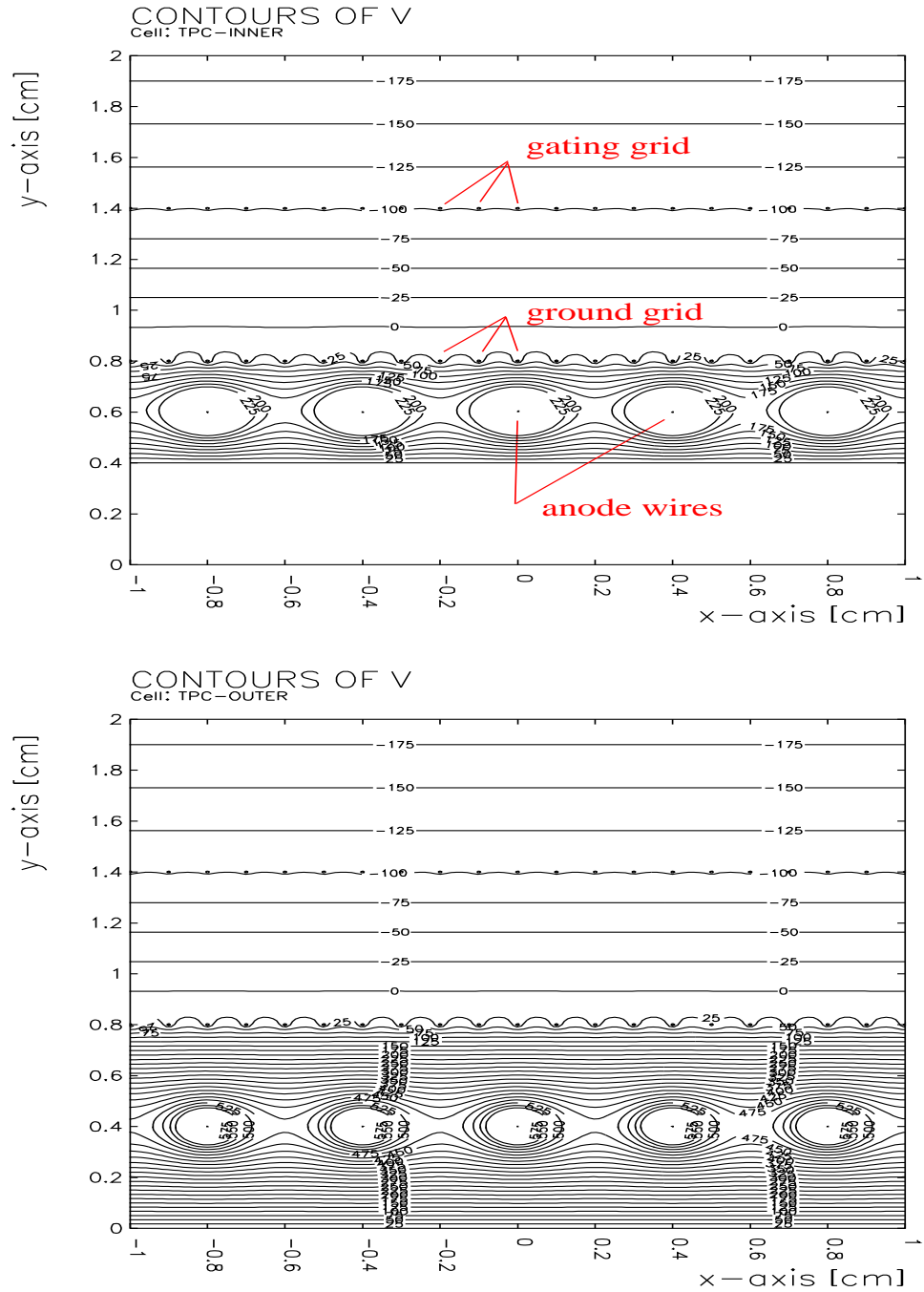


Figure 5.5: Equipotentials from drift volume to pad plane for an inner subsector (top) and an outer subsector (bottom). Equipotential lines indicate that the uniform drift field region starts at the cathode and almost extends to the gating grid. This is followed by a higher, still nearly uniform, field up to the ground wire plane. After that, the field increases up to the surface of the anode wires.

By biasing alternating wires on the gating grid positive and negative with respect to a reference voltage, the passage of ionization electrons is prohibited (see Fig. 5.4). When all wires are at the reference voltage, the nearby equi-potential lines (Fig. 5.5) are nearly parallel, allowing the passage of ionization electrons. The reference voltage on the gating grid is set such that when the grid is open, the grid is electrostatically transparent to drifting electrons. The gating grid is closed by shifting the voltages on alternate wires up or down symmetrically, leaving the average potential unchanged.

The induced signal on the pads is amplified/filtered by a set of CMOS integrated circuits consisting of a pre-amplifier and shaper circuit followed by a Switched Capacity Array (SCA) and a 10 bit Analog-to-Digital Converter (ADC). These circuits can sample the arrival of electrons into at most 512 time buckets. The position of the ionizing particle along the drift direction is reconstructed by converting the time bucket to position by knowing the drift velocity. The 512 time buckets together with the 136,560 channels on the sectors allow us to capture a 3-D image with a resolution of 70 megapixels.

The performance of the TPC during its year-one data-taking was found to meet the original design specifications[79]. For reference, the standard deviation of the position resolution for points along a track traversing the TPC parallel to the pad plane was found to be 0.5 mm. The momentum resolution was determined to be  $\delta p/p < 2\%$  for tracks with momentum  $p = 500 \text{ MeV}/c$ . The resolution in ionization energy loss ( $dE/dx$ ) was found to reach 8% for tracks measured over the entire radial dimension of the TPC.

### 5.3 Ring Image Čerenkov Detector

The Ring Image Čerenkov (RICH)[80, 81] module, schematically depicted in Fig. 5.6, consists of a liquid radiator and a photo-sensitive cathode with a 2-dimensional readout. It is placed at midrapidity and covers an area of  $1 \text{ m}^2$ .

A charged particle emits light in a medium if its velocity is greater than the local phase velocity

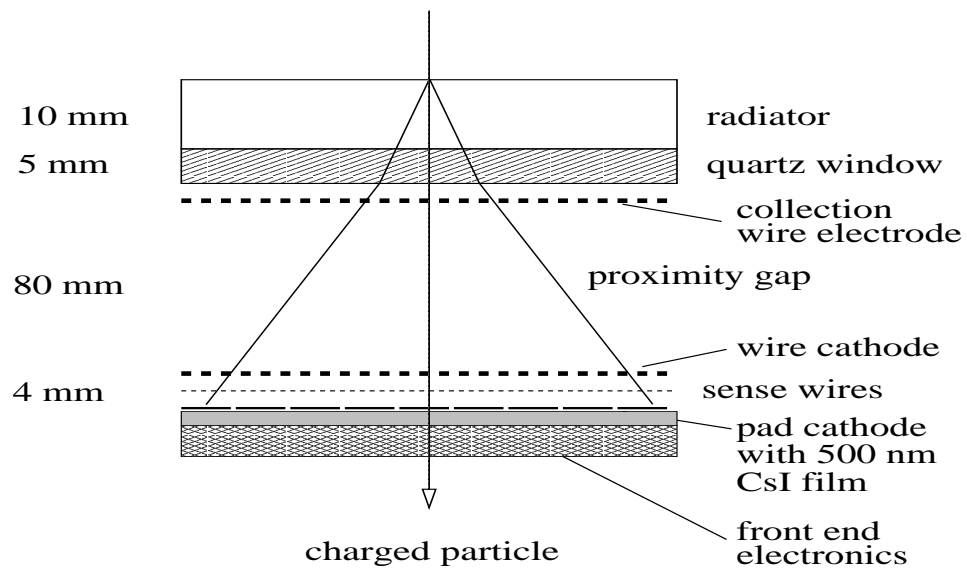


Figure 5.6: Schematic cross section of the RICH detector module.

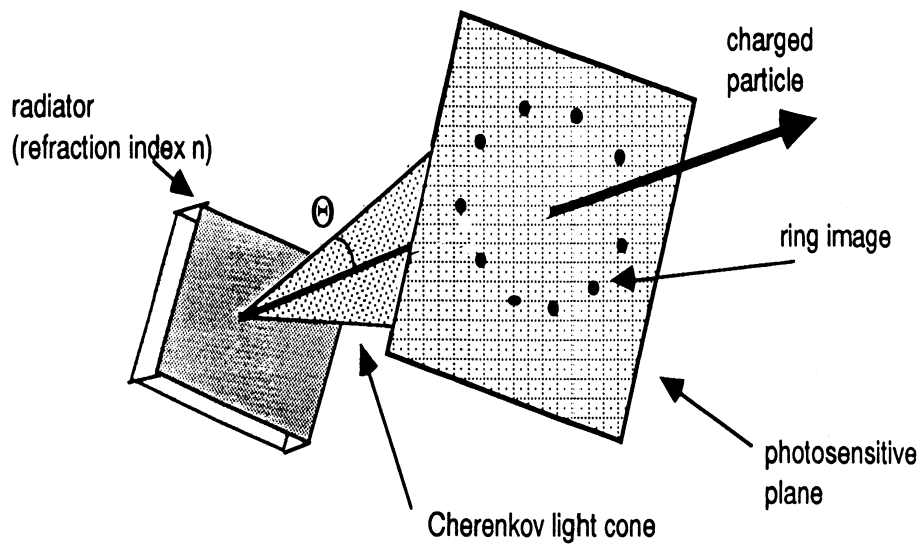


Figure 5.7: Čerenkov radiation.

of light [82, 83]. The ring image on the pad plane results from photoelectrons produced by the Čerenkov cone (Fig. 5.7) and the ring radius is related to the velocity of the particle. Knowing momenta from the TPC and velocity from RICH, the mass of the particle can be determined.

Year-one data from RICH shows that it performed well, extending the particle identification capabilities of STAR to  $\sim 3$  GeV/ $c$  for pions and kaons, and  $\sim 5$  GeV/ $c$  for protons - much higher than is possible using the  $dE/dx$  signal from the TPC alone. Data from RICH are not used in this dissertation because its solid angle coverage is too limited for the present type of elliptic flow studies.

#### 5.4 Trigger

The trigger must make decisions in less than one microsecond based on the total event multiplicity, coarse variations in multiplicity topology, event vertex location, and remnant nucleon multiplicities. During year-one data taking, the trigger was based on the CTB and the ZDC.

The CTB (Fig. 5.8) is a series of scintillator slats placed like barrel staves about the beam interaction point, and attached to the exterior of the STAR TPC. It consists of 240 slats (4 in  $\eta$  and 60 in  $\phi$ ). The scintillators are BC408 plastic 1 cm thick by 21 cm wide. In order to match the  $\eta$  coverage of the Electromagnetic Calorimeter (not installed in the year-one configuration), the scintillators were chosen to be 130 and 112.5 cm long, which gives an  $\eta$  coverage of  $0.0 < \eta < 0.50$  and  $0.50 < \eta < 0.97$ . The CTB was used to trigger on central events, as the signal is correlated to the multiplicity at mid-rapidity.

The ZDC consists of two hadronic calorimeters at  $\pm 18$  m from the detector center and at close to zero degrees ( $\theta < 2$  mrad) relative to the beam axis (Fig. 5.9). The ZDC are designed to measure neutrons emitted from nuclear fragments of the spectator matter.

Fig. 5.10 shows the correlation between ZDC and CTB. For large impact parameters, the signal in both ZDC and CTB is small because only a few spectator neutrons are produced and multiplicity in the central region is low. The CTB signal decreases continuously as the impact parameter



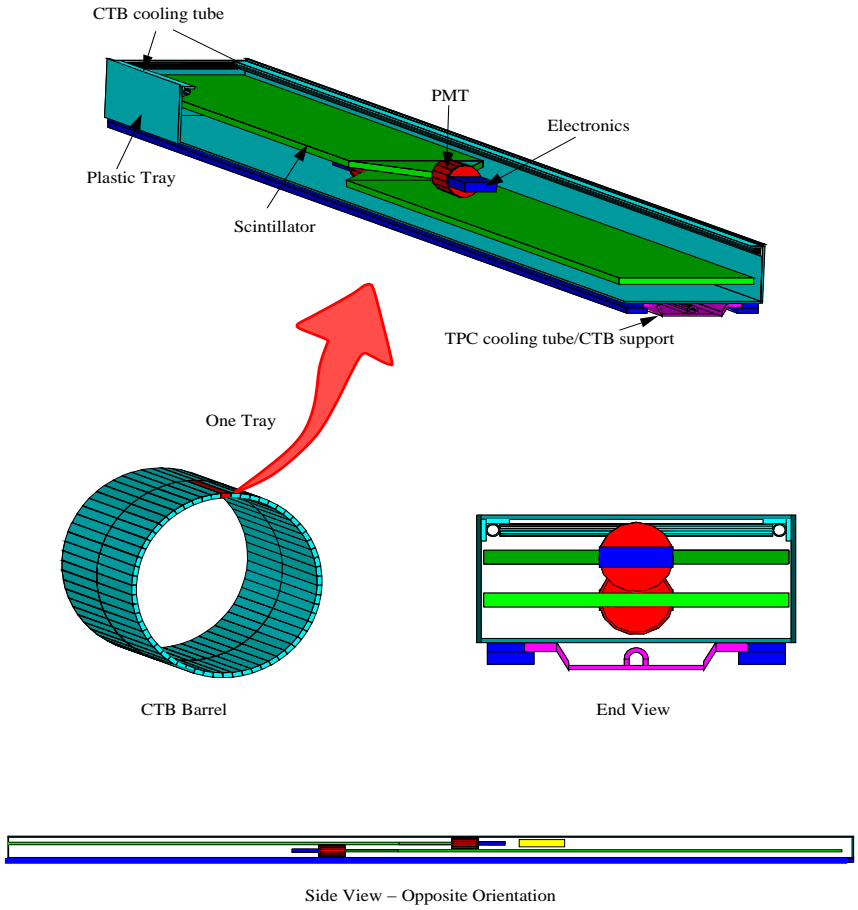


Figure 5.8: Central Trigger Barrel.

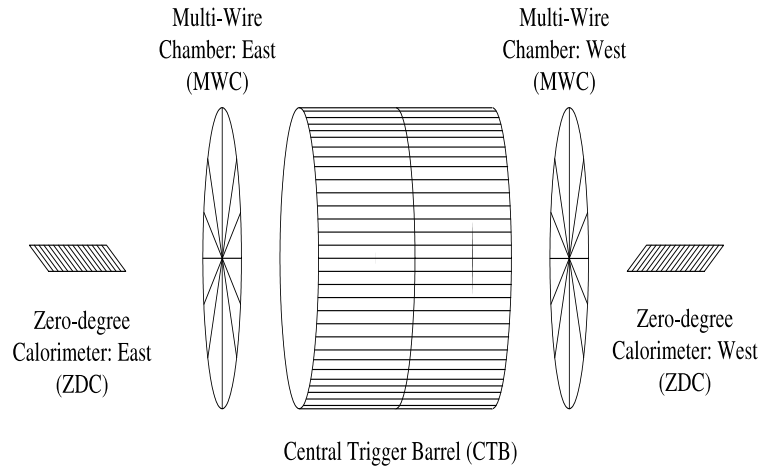


Figure 5.9: Zero Degree Calorimeters

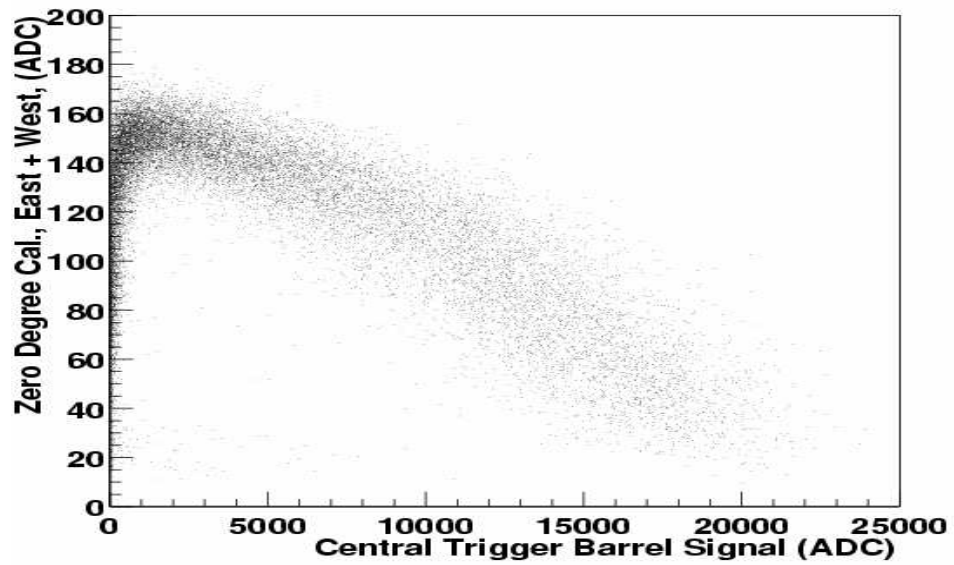


Figure 5.10: Correlation between pulse heights of Zero Degree Calorimeters and Central Trigger Barrel in a minimum bias trigger.

decreases while the ZDC signal increases to saturation, then decreases eventually for small impact parameters. The combined information can be used to provide a trigger for collision centrality.

## Chapter 6

### **dE/dx Calibration**

#### 6.1 Introduction

##### 6.1.1 Bethe-Bloch function

For a particle with charge  $Z$  (in units of  $e$ ) and speed  $\beta = v/c$  passing through a medium with density  $\rho$ , the mean energy loss it suffers can be described by the Bethe-Bloch formula:

$$-\left\langle \frac{dE}{dx} \right\rangle = 2\pi N_o r_e^2 m_e c^2 \rho \frac{Zz^2}{A\beta^2} \left[ \ln \left( \frac{2m_e \gamma^2 v^2 E_M}{I^2} \right) - 2\beta^2 \right]. \quad (6.1)$$

where  $N_o$  is Avogadro's number,  $m_e$  is the electron mass,  $r_e (= \frac{e^2}{m_e c^2})$  is the classical electron radius,  $c$  is the speed of light,  $z$  is the atomic number of the absorbing material,  $A$  is the atomic weight of the absorbing material,  $\gamma = 1/\sqrt{1-\beta^2}$ ,  $I$  is the mean excitation energy, and  $E_M (= 2m_e c^2 \beta^2 / (1-\beta^2))$  is the maximum transferable energy in a single collision.

Fig. 6.1 illustrates graphically the relation between  $dE/dx$  and  $\beta\gamma$ . In the low energy region (i.e.  $\beta\gamma < 0.5$ ), the energy loss is approximately proportional to  $\beta^{-2}$ . As one approaches the region where  $\beta\gamma = 1-3$ , all particle species go through a broad minimum ("minimum ionization"). As this region is passed, the ionization rate begins to increase roughly proportional to  $\log(\beta\gamma)$  ("relativistic rise region") then finally saturates ("Fermi plateau").

##### 6.1.2 Energy loss distribution

The ionization process of particles traveling in a medium can be modeled in terms of two components: primary and secondary interactions. Primary ionization is due to direct processes between the charged particle and the medium, while secondary processes involve the subsequent interactions

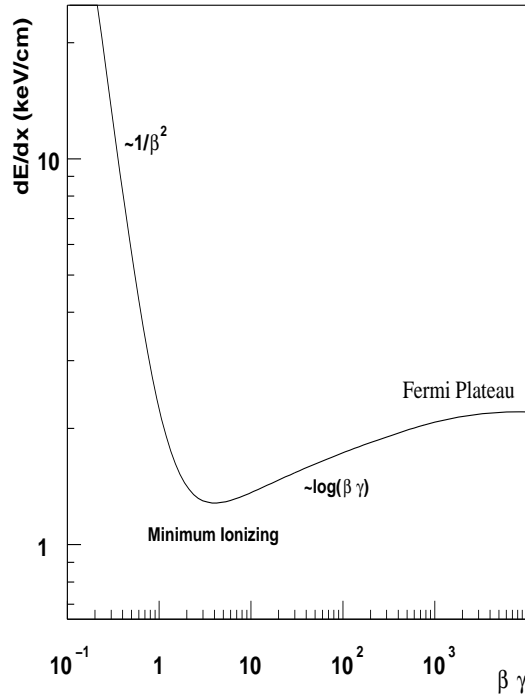


Figure 6.1: Ionization energy loss of a function of  $\beta\gamma$ .

of the primary ionization. The cross section for the primary ionization can be characterized by the Rutherford scattering formula,

$$(6.2) \quad \begin{aligned} w(E) &= \frac{2\pi z^2 e^4}{m_e v^2} N_o \frac{Z}{A} \frac{(1 - \beta^2 E/E_M)}{E^2}, \quad 0 \leq E \leq E_M, \\ w(E) &= 0, \quad E > E_M. \end{aligned}$$

Because the energy dependence is  $E^{-2}$  in the Rutherford cross section, the distribution is not bounded in the region  $0 \leq E \leq E_M$ . This causes a significant possibility for producing high energy primary electrons, which can produce additional ionization in subsequent interactions if their energy is sufficient (i.e., above the ionization potential of the medium). As a consequence of that, the final energy distribution is produced by the convolution of two distributions and has a shape which is characterised by a long tail (the ‘‘Landau tail [84]’’) at the high energy side, instead of a Gaussian shape.

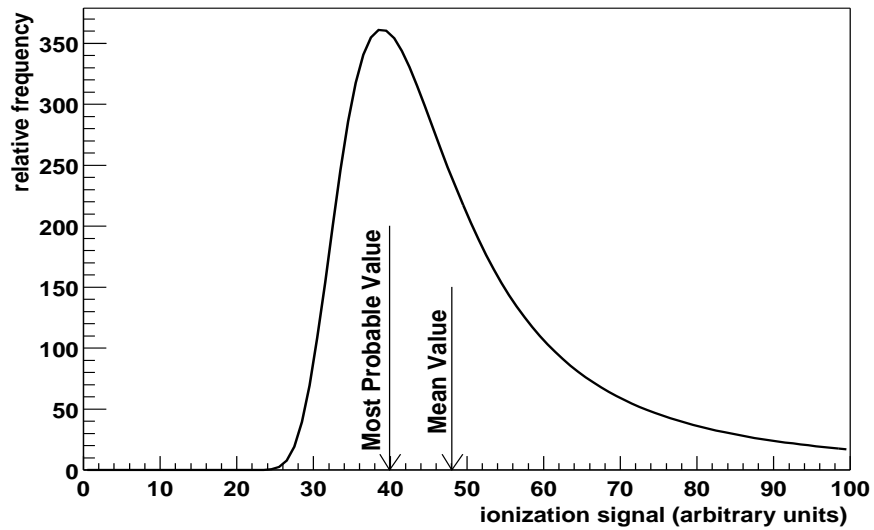


Figure 6.2: Landau distribution.

For a distribution of the Landau type, the *mean value* and the *most probable value* are not identical (Fig. 6.2). The mean is not a desirable parameter to measure in experiment, because it is quite sensitive to the number of counts in the tail of the distribution, and is subject to larger fluctuations than the peak of the distribution. The *most probable value* is a more robust observable and it is usually approximated by the truncated mean, defined as

$$\langle \frac{dE}{dx} \rangle_{trunc} = \frac{1}{M} \sum_{i=1}^M (\frac{dE}{dx})_i, \quad (6.3)$$

where  $(\frac{dE}{dx})_i$  are the  $N$  samples in order of increasing size, and  $M$  is an integer  $M \simeq fN$ , where  $f$  is a fraction typically between 0.50 and 0.85. Such an approach is the most common algorithm used in experiments. In the STAR TPC, the maximum possible number of  $dE/dx$  samples is  $N = 45$ , which is the number of pad rows in the TPC.

## 6.2 Calibration

### 6.2.1 Pad row variation

Due to variations in local gas pressure, gas gain, electronic gain etc., the final measured  $dE/dx$  could vary up or down by an arbitrary factor. To compensate for these variations,  $dE/dx$  samples for minimum ionization pion tracks are fitted to the Landau distribution for a given sector and pad row. The most probable values from the fitting are plotted as a function of pad row index (which runs from 1 to 45) and are shown in Fig. 6.3. The plot shows that the variation is on the order of 10% to 25 % (the variation depends on sector as well). Also, some pad rows with bad performance can be identified through a plot of this type.

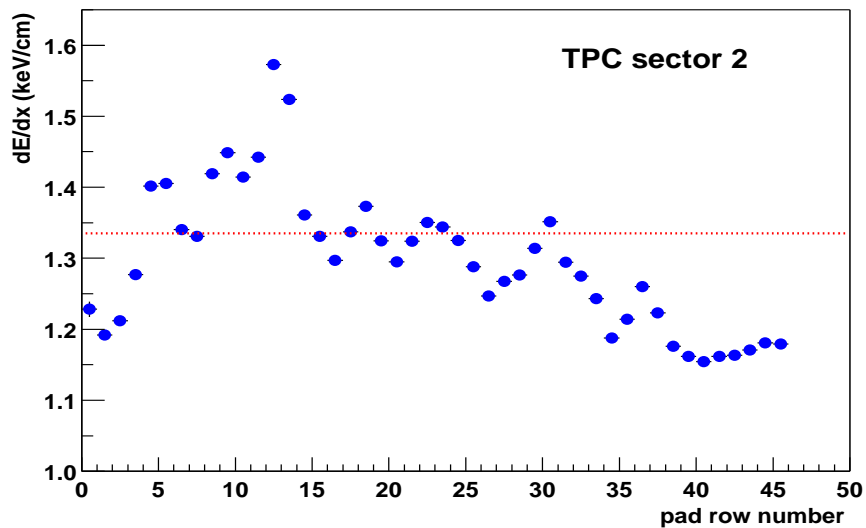


Figure 6.3:  $dE/dx$  as a function of index of pad row for sector # 2. The averaged value is drawn as a dotted line. Error bars are smaller than the symbol size.

These pad row variations can be reduced by making gain corrections. The resulting improvement in  $dE/dx$  resolution is on the order of 7% and will be shown later in this chapter.

### 6.2.2 Drift distance dependence

When ionization electrons drift towards the pad plane, the signal can be reduced by re-attachment of ions with opposite charge along the drift path. Such signal attenuation causes the  $dE/dx$  of clusters further away from the pad plane to appear smaller. Fig. 6.4 shows that the  $dE/dx$  decreases as the drift length increases (the maximum drift length corresponds to  $z = 0$  in the plot). The distortion caused by this effect can be cancelled out by application of the appropriate correction factor.

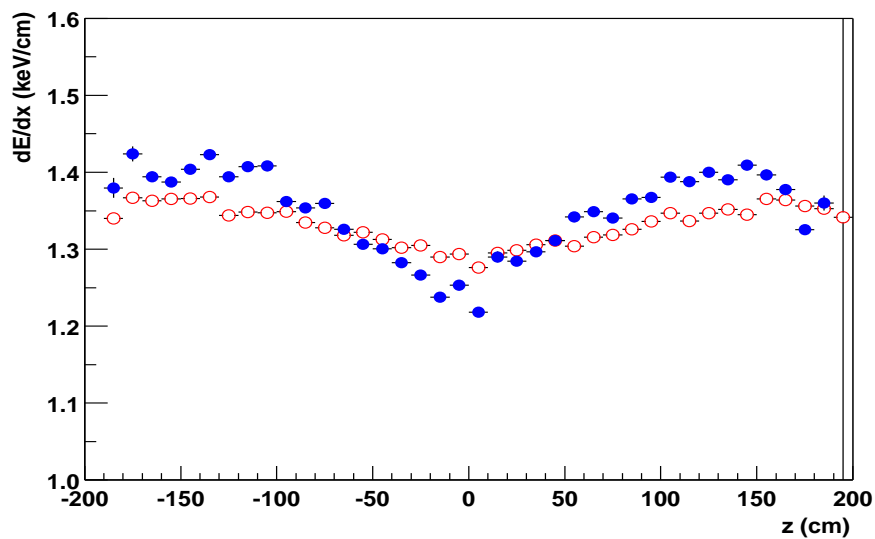


Figure 6.4:  $dE/dx$  as a function of  $z$  coordinate in TPC. Solid circles and open circles stand for inner sector and outer sector, respectively. The sample for this plot is the same sample as used in Fig. 6.3.

### 6.2.3 $dx$ dependence

$dE/dx$  versus  $dx$  is shown in Fig. 6.5.

We can see that  $dE/dx$  rises continuously as  $dx$  increases in the region  $dx < 2.5$  cm. That can be understood as follows: the width of the  $dE/dx$  distribution for samples with large  $dx$  is narrower than that of samples with small  $dx$  (just like more statistics reduces the error on a measurement). Then for a given amount of energy loss associated with the track, the *most probable value* (that is, the position of the peak of the Landau shape) for large  $dE/dx$  samples has to shift to a higher value



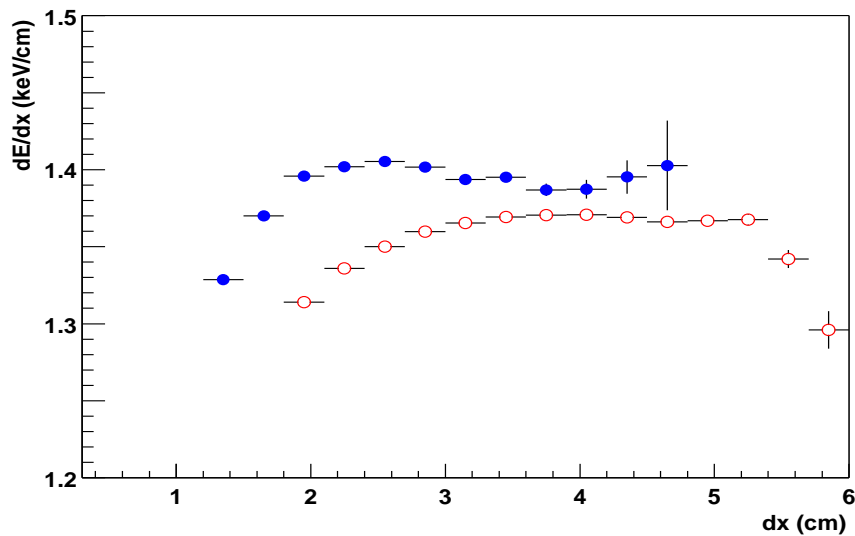


Figure 6.5:  $dE/dx$  as a function of  $dx$  in TPC. Solid circles and open circles stand for inner sector and outer sector, respectively. The sample for this plot is the same sample as used in Fig. 6.3.

in order to leave the total energy of ionization unchanged.

### 6.3 Truncation ratio optimization

What needs to be optimized for best Particle Identification (PID) is not the resolution but the particle separation power, which is defined as:

$$\begin{aligned} \text{separation power} &= \frac{\text{separation}}{\text{resolution}} \\ &= \frac{(dE/dx)_A - (dE/dx)_B}{\sigma(dE/dx)_{A,B}}, \end{aligned} \quad (6.4)$$

where  $\sigma(dE/dx)_{A,B}$  is the resolution from either A or B (both are normally the same).

To study the separation power as a function of truncation ratio, pions with momentum between 350 MeV/c and 450 MeV/c and protons with momentum between 600 MeV/c and 650 MeV/c were considered. Fig. 6.6 shows that 60% truncation (see Eq. 6.3) gives the best separation power.

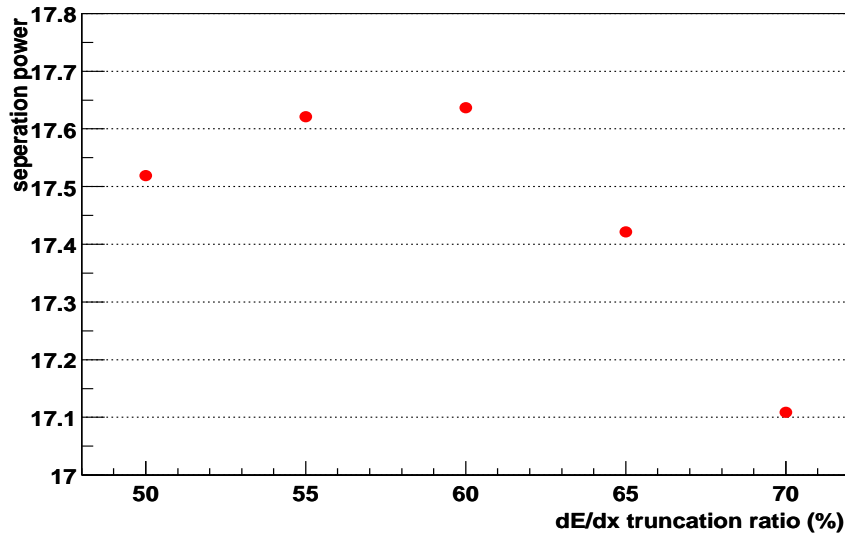


Figure 6.6: The separation power as a function of truncation ratio.

#### 6.4 Improvement on $dE/dx$ resolution

The  $dE/dx$  resolution is characterised by the *sigma of a single trial*, which is  $A$  in the following equation:

$$\sigma_{(dE/dx)/(dE/dx)} = \frac{A}{\sqrt{M}}, \quad (6.5)$$

where  $M$  is as defined in Eq. 6.3.

The relation between  $\sigma_{(dE/dx)/(dE/dx)}$  and  $M$  is shown in Fig. 6.7. The *sigma of a single trial* is improved by 9.6 % (drops from  $0.5169 \pm 0.0004$  to  $0.4675 \pm 0.0003$ ) by applying the various  $dE/dx$  calibrations mentioned in this chapter. If combined with truncation ratio optimization, the total improvement in  $dE/dx$  resolution is about 13% (*sigma of a single trial* drops from  $0.5168 \pm 0.0004$  to  $0.4675 \pm 0.0003$ ).

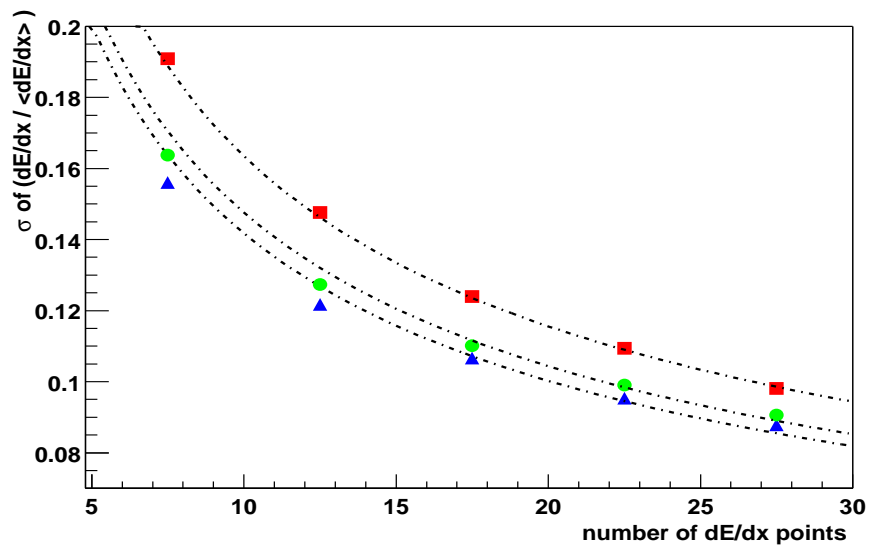


Figure 6.7:  $\sigma_{(dE/dx / \langle dE/dx \rangle)}$  versus number of points used in  $dE/dx$  calculation. Squares and circles stand for without  $dE/dx$  calibration, and with  $dE/dx$  calibration, respectively. Triangles stand for truncation ratio optimized for calibrated  $dE/dx$ .

## Purity PID

### 7.1 Purity

The purity for identifying a particle as belonging to a specific particle type is defined as that particle's yield divided by the sum of yields for all particles at the same  $dE/dx$ . To get the purity, multi-Gaussian fitting of  $dE/dx$  distributions in a momentum range must be applied. The quality of the fitting directly affects the PID, especially in the momentum region where  $dE/dx$  bands are close to each other. Additional constraints are used in order to extend the multi-Gaussian fitting towards the region of band merging, namely: 1) the use of pre-calibrated Bethe-Bloch formulae allows us to constrain the expected  $\langle dE/dx \rangle$  for each particle type, and 2) the use of pre-calculated resolution allows us to constrain the  $\sigma$  of the various Gaussians.

It is observed that  $dE/dx$  resolution depends on centrality and pseudorapidity (the *sigma of a single trial* increases  $\sim 11\%$  from peripheral events to central events, and increases  $\sim 18\%$  between  $0.9 \leq |\eta| \leq 1.0$  and  $0. \leq |\eta| \leq 0.1$ ). So in the Bethe-Bloch calibration, resolution calculation and multi-Gaussian fitting are done with different cuts according to centralities, pseudorapidities, etc.

### 7.2 Bethe-Bloch calibration

To obtain a good set of samples for the Bethe-Bloch calibration, pions, kaons and protons from the well-separated region on the plot of  $dE/dx$  versus  $p$  were selected. Fig. 7.1 shows  $dE/dx$  versus  $\beta\gamma$  from the combination of different particle types. The fact that all particle types lie on a single universal curve confirms that calibration of the  $dE/dx$  signal and the various systematic effects arising from the detector are under control.

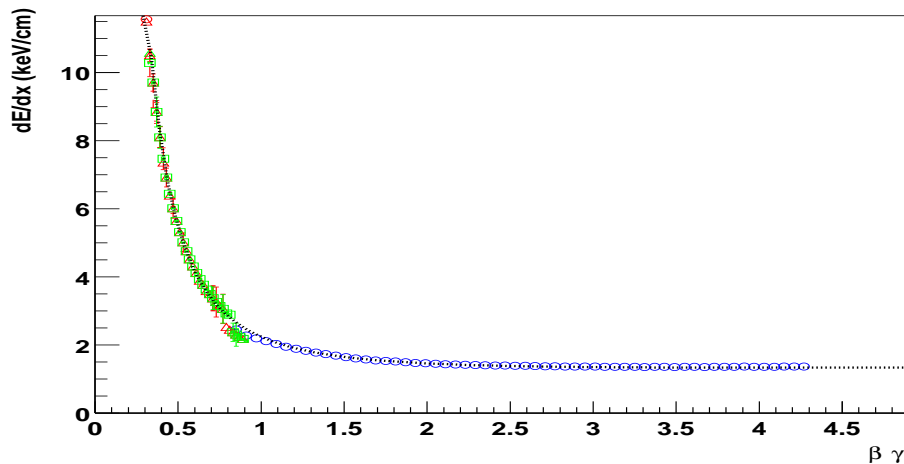


Figure 7.1:  $dE/dx$  versus  $\beta\gamma$ . The circles, triangles and squares represent pions, kaons and protons, respectively.

Fig. 7.2 shows the  $dE/dx$  versus  $p$  for all particles with the expected value from the calibrated Bethe-Bloch function.

### 7.3 Determine *sigma of a single trial*

The *sigma of a single trial* (see Chapter on  $dE/dx$  Calibration) is obtained by fitting  $\sigma_{(dE/dx)/\langle dE/dx \rangle}$  versus number of points used in the  $dE/dx$  calculation for minimum ionizing pions. STAR has different data “productions” due to the continuous software revision and significant change in  $dE/dx$  calibration happened between production P00hm and P01he.

Table 7.1 lists the *sigma of a single trial* for data production P00hm, from which we can see the resolution (which is characterised by the *sigma of a single trial*) degrades for increasing event multiplicity. This can be understood as being related to the difficulty of track reconstruction as the hit density increases in the detector.

For data production P01he, a clear dependence of resolution on pseudorapidity is observed. Such a dependence maybe due to tracks with high dip angle tending to have more hits with larger

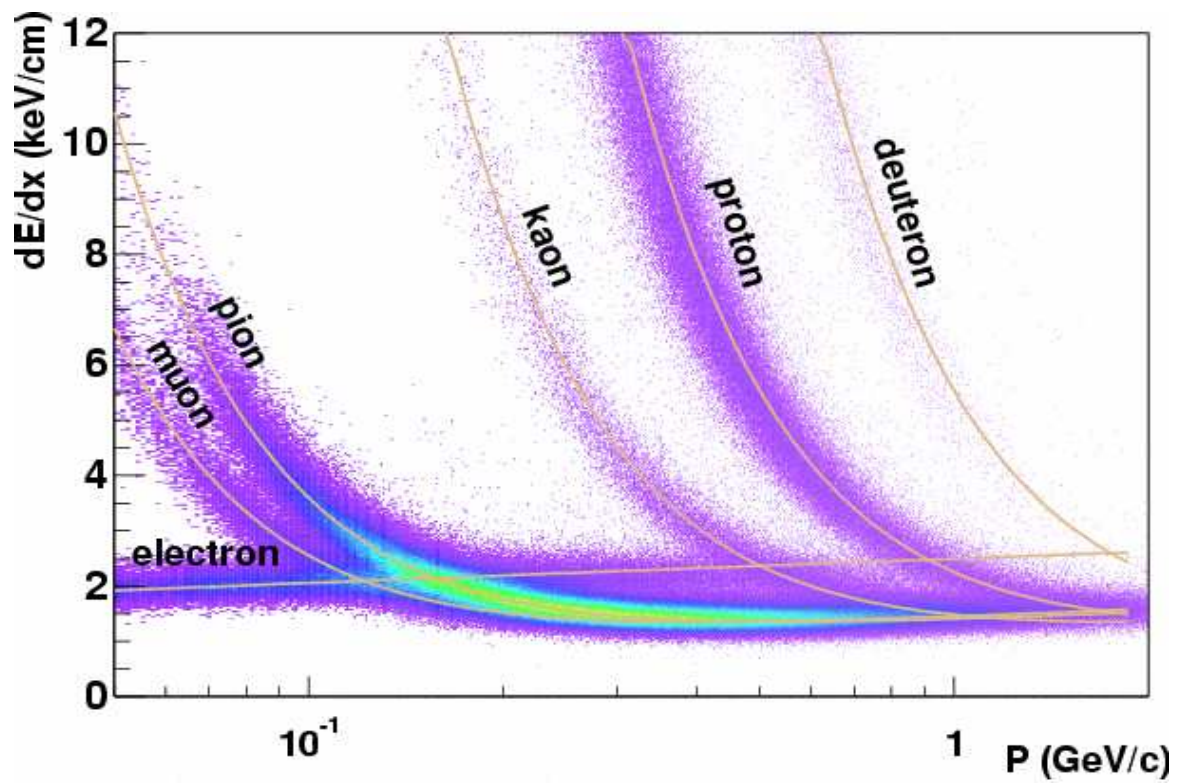


Figure 7.2:  $dE/dx$  versus momentum. Curves are based on the calibrated Bethe-Bloch formula.

< 26%	26% – 10%	top 10%
0.527	0.554	0.586

Table 7.1: *sigma of a single trial* for different centralities. These numbers are for STAR P00hm data production.

$dx$ , which can reduce the width of the  $dE/dx$  distribution.

Table 7.2 lists *sigma of a single trial* for STAR data production P01he .

$ \eta $	< 26%	26% – 10%	top 10%
0.0 – 0.1	0.497981	0.514528	0.550111
0.1 – 0.2	0.495237	0.535365	0.545285
0.2 – 0.3	0.495062	0.50982	0.536676
0.3 – 0.4	0.472484	0.518347	0.550063
0.4 – 0.5	0.465823	0.498163	0.513364
0.5 – 0.6	0.45885	0.489383	0.509784
0.6 – 0.7	0.448218	0.464715	0.480572
0.7 – 0.8	0.435925	0.472486	0.476077
0.8 – 0.9	0.425025	0.445808	0.459282
0.9 – 1.0	0.41713	0.451734	0.449447

Table 7.2: *sigma of a single trial* for different centralities and different pseudorapidities. These numbers are for STAR P01he data production

#### 7.4 Multi-Gaussian fitting

In the momentum region where particles are well separated, the multi-Gaussian fitting is straightforward. As the fitting extends to the semi-merged region, two constraints were used. 1. The  $\sigma$  is constrained by the pre-calculated resolution, which should be a constant over the momentum range 0-4 GeV/ $c$  (confirmed by studying the  $dE/dx$  of charged kaons identified through decays in flight to a muon and a neutrino). 2. The expected band center is constrained by the pre-calibrated Bethe-Bloch curve. Fig. 7.3 shows multi-Gaussian fits for central events at  $|\eta| \leq 0.1$ .

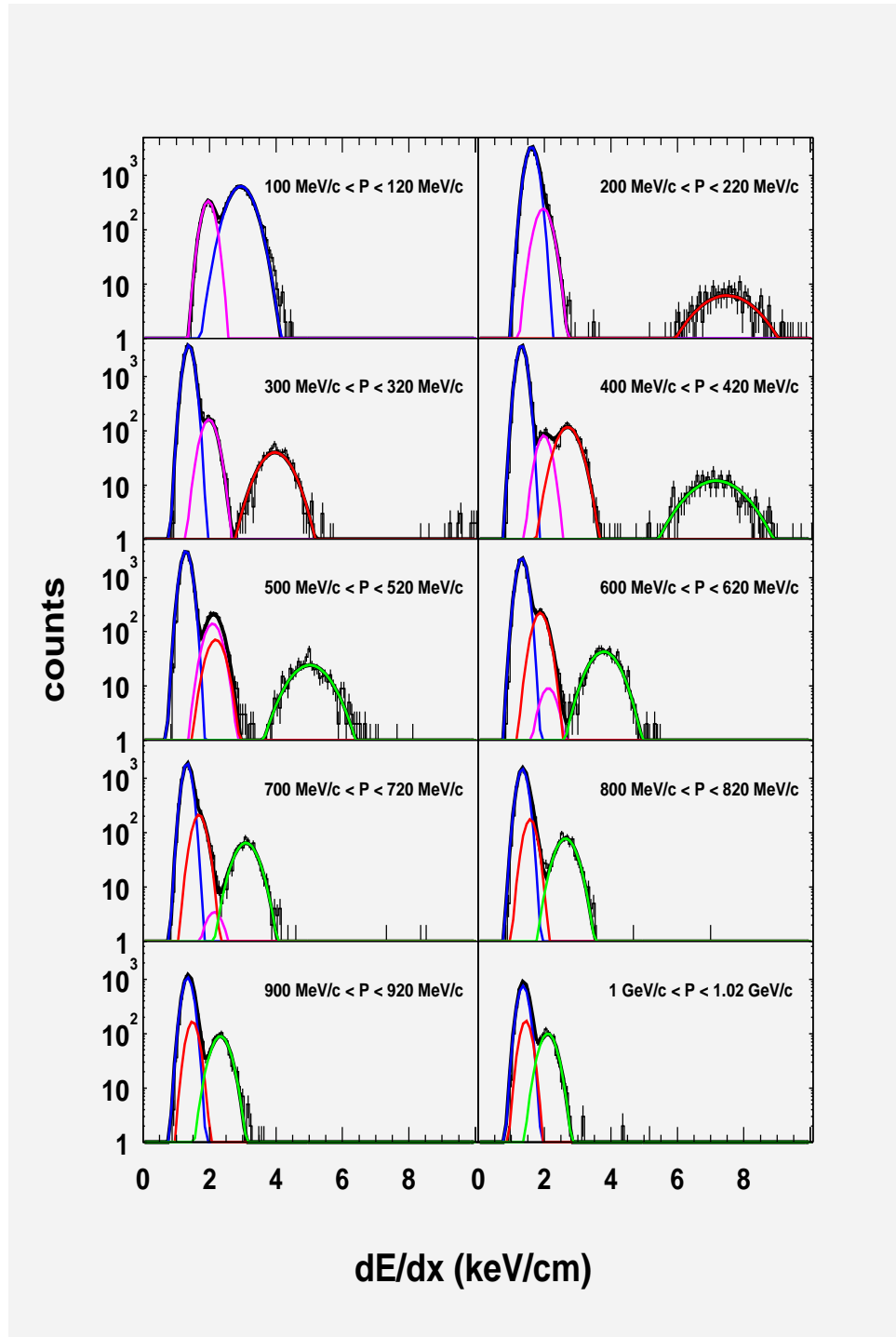


Figure 7.3: Multi-Gaussian fitting of  $dE/dx$  for different momentum regions.



### 7.5 Electron contamination

In regions where bands for different particles merge together, the  $dE/dx$  fitting is less reliable. A notable case in point is electron contamination. To solve this problem, for each particle type, amplitudes at the band center (heights of the Gaussians from the multi-Gaussian fitting) were re-fitted as a function of momentum. Fig. 7.4 shows such a fitting. In the plot, the amplitude of the electron band center in the clean region ( $0.2 < p < 0.4 \text{ GeV}/c$ ) is fitted by an exponential function, then extrapolated to the merged region ( $0.1 < p < 0.2$  and  $0.4 < p < 0.6 \text{ GeV}/c$ ). For the region where  $p < 0.1 \text{ GeV}/c$ , the electron band and pion band are well separated, so their PID can be performed by simply cutting on  $dE/dx$ .

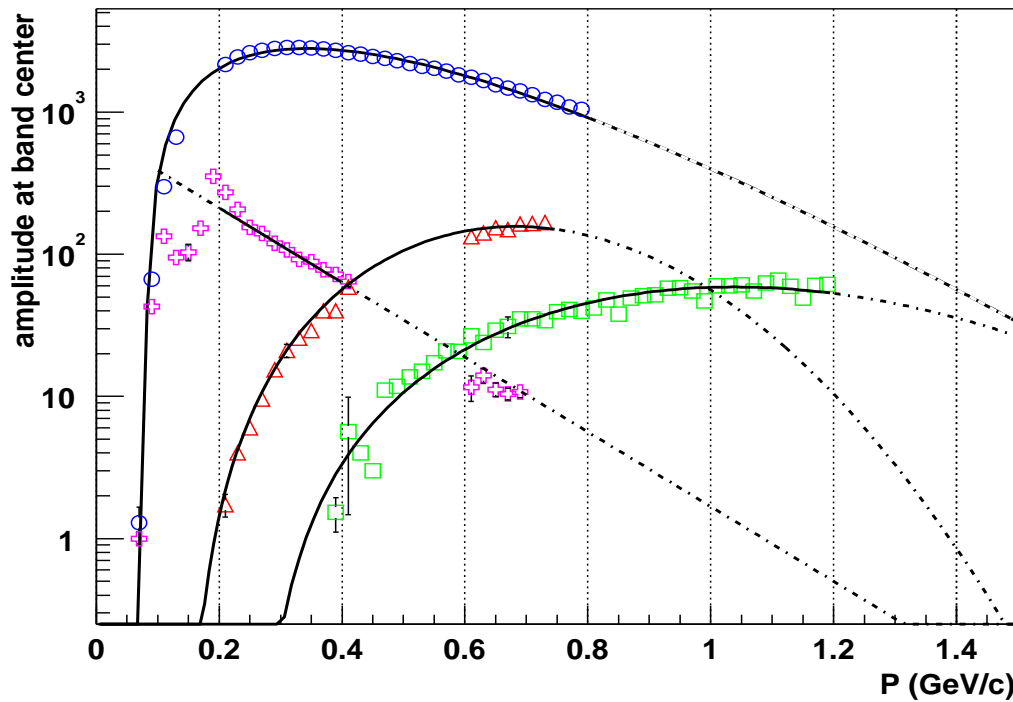


Figure 7.4: Amplitudes at the band center as a function of momentum. The circles, crosses, triangles and squares represent pions, electrons, kaons and protons, respectively. Dotted lines show the extrapolation. Amplitudes of electrons in the region  $0.6 < p < 0.7 \text{ GeV}/c$  are from multi-Gaussian fits between the kaon band and the proton band. These result demonstrate that the extrapolation of electron band amplitudes is reliable.

## 7.6 Purity result

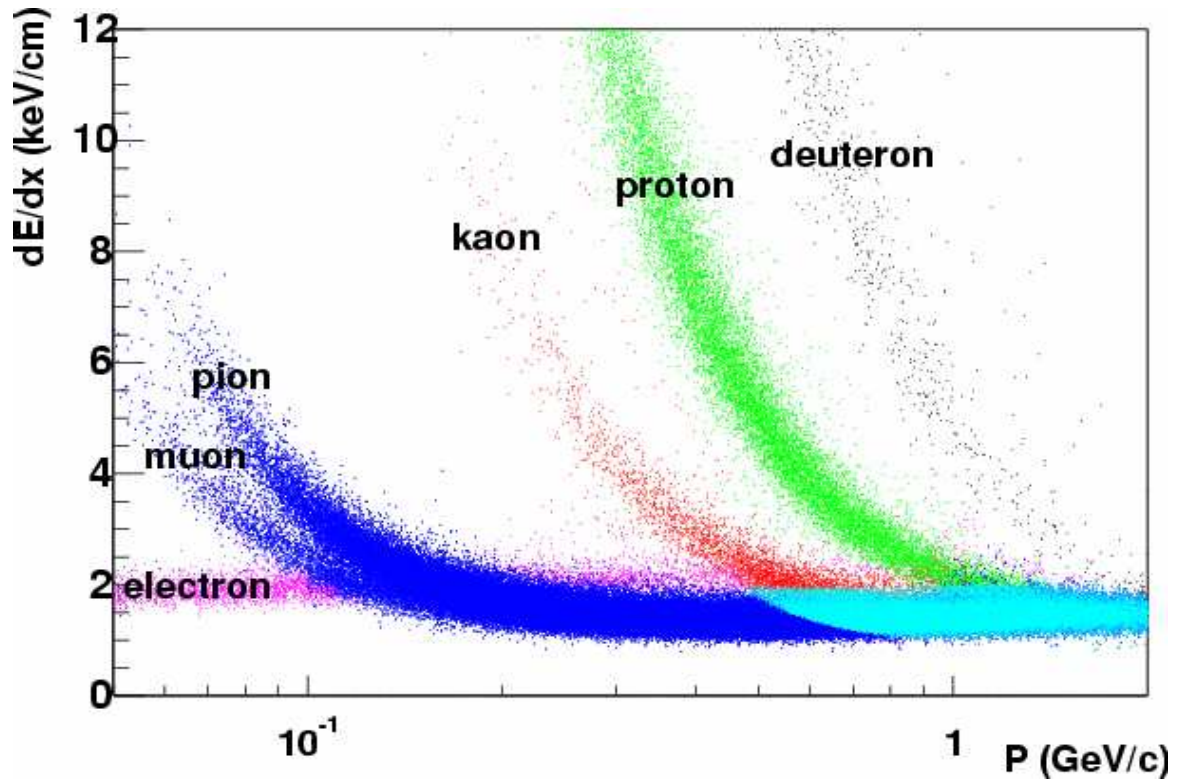


Figure 7.5:  $dE/dx$  versus  $p$  for particles with identities assigned according to maximum purity .

Fig. 7.5 shows the  $dE/dx$  versus  $p$  plot for identified particles with different colors representing different particle types. Particles in the region where the kaon band, proton band and pion band merge together are mostly identified as pions but the PID is based on extrapolation, so a different color (shade if black/white) is used to distinguish them from pions identified without extrapolation.

Fig. 7.5 is based on minimum bias events, and the multi-Gaussian fittings were done for each cell in the following parameter space:

- 1.) 3 centrality bins: (100% – 26%, 26% – 10%, > 10% central).
- 2.) 2 dca bins: (0 – 3 cm, > 3 cm).
- 3.) 2 charge bins: (+, –).
- 4.) 100 equally-spaced momentum bins covering 0 GeV/ $c$  to 2GeV/ $c$ .

5.) 10 equally-spaced pseudorapidity bins covering 0 to 1. If  $|\eta| > 1.0$ , it was taken as belonging to the last bin.

6.) 6 equally-spaced intervals of  $N$  (number of  $dE/dx$  samples) covering 0 to 30. If  $N > 30$ , it was taken as belonging to the last bin.

If  $p_t$  cuts are chosen instead of  $p$  cuts when applying the multi-Gaussian  $dE/dx$  fitting, a narrow  $\eta$  cut together with the  $p_t$  cut is necessary because switching to  $dE/dx$  versus  $p_t$  makes the resolution worse. In Fig. 7.5, no  $p_t$  cuts were used. In order to make the result reliable if a conversion from  $p$  to  $p_t$  is needed when using the PID result, fine binning in  $p$  was used (20 MeV/ $c$  per  $p$  bin), as well as fine binning in  $\eta$  (0.1 per bin).

## Elliptic Flow

### 8.1 Introduction

In non-central heavy-ion collisions, the initial spatial deformation due to geometry and the pressure developed early in the collision causes azimuthal momentum-space anisotropy, which is correlated with the reaction plane [2, 3, 58, 86]. Measurements of this correlation, known as anisotropic transverse flow, provides insight into the evolution of the early stage of a relativistic heavy-ion collision [87]. Elliptic flow is characterized by the second harmonic coefficient  $v_2$  of an azimuthal Fourier decomposition of the momentum distribution [4, 5, 6], and has been observed and extensively studied in nuclear collisions from sub-relativistic energies on up to RHIC. At top AGS and SPS energies, elliptic flow is inferred to be a relative enhancement of emission *in* the plane of the reaction.

Elliptic flow is developed mostly in the first fm/ $c$  after the collision and thus provides information about the early-time thermalization achieved in the collisions [7]. Generally speaking, large values of flow are considered signatures of hydrodynamic behavior [4]. Models in which the colliding nuclei resemble interacting volumes of dilute gas — the low density limit (LDL) — represent the limit of mean free path that is the opposite of hydrodynamics. It remains unclear to what extent the LDL picture can describe the data at RHIC, and valuable insights can be gained from mapping out the conditions under which hydrodynamic and LDL calculations can reproduce the measured elliptic flow.

Anisotropic flow refers to correlations in particle emission with respect to the reaction plane. The reaction plane orientation is not known in experiment, and anisotropic flow is usually reconstructed from the two-particle azimuthal correlations.

But there are several possible sources of azimuthal correlations that are unrelated to the reaction plane — examples include correlations caused by resonance decays, (mini)jets, strings, quantum statistics effects, final state interactions (particularly Coulomb effects), momentum conservation, etc. The present study does not distinguish between the various effects in this overall category, but classifies their combined effect as “non-flow” correlations.

Conventional flow analyses are equivalent to averaging over correlation observables constructed from pairs of particles. When such analyses are applied to relativistic nuclear collisions where particle multiplicities can be as high as a few thousand, the possible new information contained in multiplets higher than pairs remains untapped. A previous study of high-order flow effects focused on measuring the extent to which all fragments contribute to the observed flow signal [8], and amounted to an indirect means of separating flow and non-flow correlations. Given that flow analyses based on pair correlations are sensitive to both flow and non-flow effects, the present work investigates correlation observables constructed from particle quadruplets. The cumulant formalism removes the lower-order correlations which are present among any set of four particles, leaving only the effect from the so-called “pure” quadruplet correlation. The simplest cumulant approach, in terms of both concept and implementation, partitions observed events into four subevents. In the present study, the four-subevent approach is demonstrated, but our main focus is on a more elaborate cumulant method, developed by Borghini, Dinh and Ollitrault [88, 89]. There are indications that non-flow effects contribute at a negligible level to the four-particle cumulant correlation, making it unnecessary to continue to even higher orders for the purpose of separating the flow and non-flow signals.

Fluctuations in measured observables invariably are reflected in the statistical errors on the measurements, but in most cases, the symmetry of the fluctuations is such that the measurements are not systematically biased to higher or lower values by the fluctuations. However, there is a potential for observables under investigation in this dissertation to suffer bias under the influence of impact

parameter fluctuations within the studied centrality bins. In particular, the observed multiplicity of charged particles within the detector acceptance is used to characterize centrality, and especially within the bin of highest multiplicity, it is clear that the elliptic flow signal must vary over a wide range, depending on the impact parameter. In the present study, a correction is applied to reduce this bias to an insignificant level.

The present study begins with a review of the standard pair correlation method, and provides details concerning the approach adopted in earlier STAR publications [7, 90] for treating non-flow correlations. A new method of pair flow analysis using the scalar product of flow vectors also is introduced. In the conventional method, a flow coefficient is calculated by the mean cosine of the difference in angle of two flow vectors. In the scalar product method, this quantity is weighted by the lengths of the vectors. The new method offers advantages, and is also simple to apply.

Measurements presented in this dissertation are based on Au+Au data at  $\sqrt{s_{NN}} = 130$  GeV recorded by STAR (Solenoidal Tracker At RHIC) during the summer of 2000. A detailed description of the detector in its year-one configuration can be found elsewhere [78, 7]. The analysis is based on 170k events corresponding to a minimum bias trigger. Events with a primary vertex beyond 1 cm radially from the beam or 75 cm longitudinally from the center of the Time Projection Chamber (TPC) were excluded. Within the selected events, tracks were used for the estimation of the flow vector if all five of the following conditions were satisfied: they passed within 2 cm of the primary vertex, they had at least 15 space points in the TPC, the ratio of the number of space points to the expected maximum number of space points was greater than 0.52, pseudorapidity  $|\eta| < 1.3$ , and transverse momentum  $0.1 < p_t < 2.0$  GeV/ $c$ . Particles over a wider range in  $\eta$  and  $p_t$  were correlated with this flow vector as shown in the graphs below. Centrality is characterized in eight bins of charged particle multiplicity,  $n_{ch}$ , divided by the maximum observed charged multiplicity,  $n_{max}$ , with a more stringent cut  $|\eta| < 0.75$  imposed only for this centrality determination. The above cuts are essentially the same as used in the previous STAR studies of elliptic flow [7, 90].

## 8.2 Two-particle correlation methods

Anisotropic transverse flow manifests itself in the distribution of  $\phi' = \phi - \Psi$ , where  $\phi$  is the measured azimuth for a track in detector coordinates, and  $\Psi$  is the azimuth of the estimated reaction plane in that event. The observed anisotropies are described by a Fourier expansion,

$$dN/d\phi' \propto 1 + 2v_1 \cos \phi' + 2v_2 \cos 2\phi' + \dots \quad (8.1)$$

Each measurable harmonic can yield an independent estimate  $\Psi_n$  of the event reaction plane via the event flow vector  $Q_n$ :

$$\begin{aligned} Q_n \cos n\Psi_n &= \sum_i w_i \cos n\phi_i, \\ Q_n \sin n\Psi_n &= \sum_i w_i \sin n\phi_i, \end{aligned} \quad (8.2)$$

where the sums extend over all particles in a given event, and the  $w_i$  are weights adjusted to optimize the event plane resolution [92, 6].

Below we also use the representation of the flow vector as a complex number. Real and imaginary parts are equal to the  $x$  and  $y$  components defined in Eq.8.2:

$$Q_n = \sum_i w_i u_i, \quad (8.3)$$

where  $u_i = e^{in\phi_i}$  is a unit vector associated with the  $i$ -th particle.

### 8.2.1 Correlation between flow angles from different subevents. Estimate of non-flow effects.

In order to report anisotropic flow measurements in a detector-independent form, it is customary to divide each event into two subevents and determine the resolution of the event plane by correlating the  $Q_n$  vector for the subevents [91, 6]. In order to estimate the contribution from different non-flow effects, one can use different ways of partitioning the entire event into two subevents. The partitioning into subevents where all particles in the same subevent have the same charge ensures that no pair within that subevent can come from neutral resonance decay. The partition using two

(pseudo)rapidity regions separated by  $\Delta y \geq 0.1$  should greatly suppress the contribution from quantum statistics effects and Coulomb (final state) interactions.

Another important observation for the estimate of the non-flow effects is their dependence on centrality. The correlation between two subevent flow angles is

$$\begin{aligned}
\langle \cos(2(\Psi_2^{(a)} - \Psi_2^{(b)})) \rangle &\approx \left\langle \frac{\sum_{i=1}^{M_{sub}} u_i}{\sqrt{M_{sub}}} \cdot \frac{\sum_{j=1}^{M_{sub}} u_j^*}{\sqrt{M_{sub}}} \right\rangle \\
&= \frac{M_{sub} M_{sub}}{M_{sub}} \langle u_i u_j^* \rangle \\
&\propto M_{sub} (v_2^2 + g),
\end{aligned} \tag{8.4}$$

where  $M_{sub}$  is the multiplicity for a sub-event,  $g$  denotes the non-flow contribution to two-particle correlations. For correlations due to small clusters, which are believed responsible for the dominant non-flow correlations, the strength of the correlation should scale in inverse proportion to the total multiplicity [88]. The subevent multiplicity is proportional to the total multiplicity,  $g = \tilde{g}/M_{sub}$ .

Collecting terms, we arrive at

$$\langle \cos(2(\Psi_2^{(a)} - \Psi_2^{(b)})) \rangle \propto M_{sub} v_2^2 + \tilde{g}. \tag{8.5}$$

What is important is that the non-flow contribution to  $\langle \cos(2(\Psi_2^{(a)} - \Psi_2^{(b)})) \rangle$  is approximately independent of centrality. The typical shape of  $\langle \cos(2(\Psi_2^{(a)} - \Psi_2^{(b)})) \rangle$  for flow (see, for example, Fig. 8.1) is peaked at mid-central events due to the fact that for peripheral collisions,  $M_{sub}$  is small, and for central events,  $v_2$  is small. In the previous estimates [7, 90] of the systematic errors, we have set the quantity  $\tilde{g} = 0.05$ . The justification for this value was the observation of similar correlations for the first and higher harmonics (we have investigated up to the sixth harmonic). One could expect the non-flow contribution to be of similar order of magnitude for all these harmonics, and HIJING [93, 94] simulations support this conclusion. Given the value  $\tilde{g} = 0.05$ , one simply estimates the contribution from non-flow effects to the measurement of  $v_2$  from the plot of  $\langle \cos(2(\Psi_2^{(a)} - \Psi_2^{(b)})) \rangle$  using Eq.(8.5).



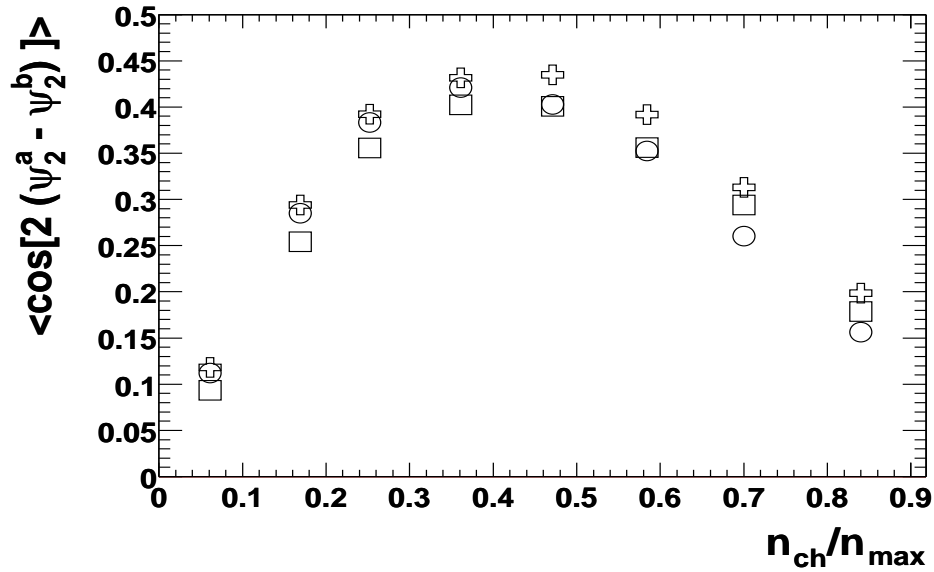


Figure 8.1: Correlation between the event plane angles determined from pairs of subevents partitioned randomly (circles), partitioned with opposite sign of pseudorapidity (squares) and partitioned with opposite sign of charge (crosses). The correlation is plotted as a function of centrality, namely charged particle multiplicity  $n_{ch}$  divided by the maximum observed charged multiplicity,  $n_{max}$ .

Fig. 8.1 shows the event plane correlation between two subevents, for each of three different subevent partitions. In central events, it is seen that the correlation is stronger in the case of subevents with opposite sign of charge compared to subevents partitioned randomly. This pattern might be due to resonance decays to two particles with opposite charge. The spread of the results for different subevent partitions is about 0.05, which is in accord with the number used for the estimates of the systematic errors.

The event plane resolution for full events with  $p_t$  weighting can reach as high as 0.8, as shown in Fig. 8.2. The  $v_2$  as a function of centrality is shown in Fig. 8.3, using different prescriptions to partition the particles into subevents. Again, partitioning into subevents with opposite sign of charge yields the highest elliptic flow signal, presumably because of neutral resonance ( $\rho^0$ , etc.) decay.

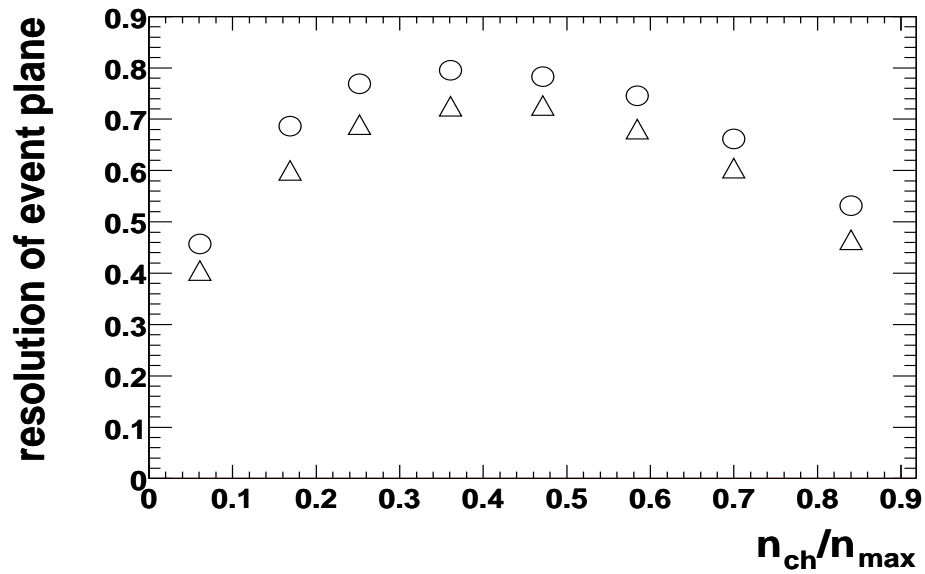


Figure 8.2: The event plane resolution for full events as a function of centrality, using randomly partitioned subevents with (circles) and without (triangles)  $p_t$  weight.

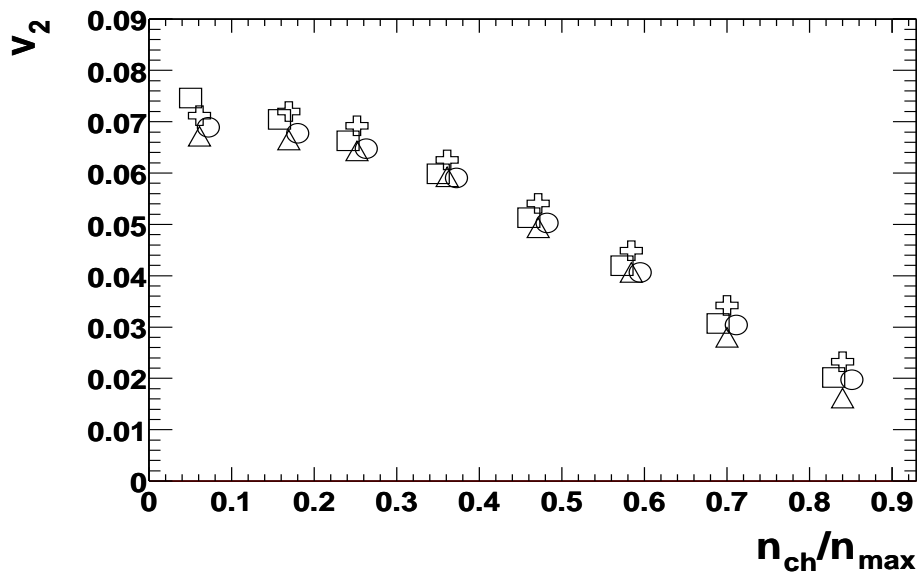


Figure 8.3: Elliptic flow signal  $v_2$  as a function of centrality, from study of the correlation between particle pairs consisting of randomly chosen particles (circles), particles with opposite sign of charge (crosses), particles with the same sign of charge (triangles) and particles with opposite sign of pseudorapidity (squares).

### 8.2.2 Weighting

The best weight  $w_i(\eta, p_t)$  is  $v_2(\eta, p_t)$  itself. In practice, since we know that  $v_2$  is approximately proportional to  $p_t$  up to about 2 GeV/ $c$ , it is convenient to use  $p_t$  as the weight. It is found that  $p_t$  weighting can reduce the statistical error significantly, as demonstrated in Fig. 8.4.

Some detectors have substantial asymmetry in their response as a function of azimuth in detector coordinates, in which case it is necessary to employ one of two possible compensation methods [6] to avoid distortion of the measured flow signals. In the present study, no noticeable difference is observed with and without compensation for detector asymmetry, as expected in light of the excellent azimuthal symmetry of the STAR TPC. All plots in this dissertation are made without compensation for detector asymmetry.

### 8.2.3 Scalar product flow analysis

In a new scalar product method [95], each event is partitioned into two subevents, labeled by the superscripts  $a$  and  $b$ . The correlation between two subevents is

$$\langle \mathbf{Q}_n^a \cdot \mathbf{Q}_n^b \rangle = \langle v_n^2 M^a M^b \rangle, \quad (8.6)$$

where  $M^a$  and  $M^b$  are the multiplicities for subevents  $a$  and  $b$ , respectively. The vectors  $\mathbf{Q}_n^a$  and  $\mathbf{Q}_n^b$  are constructed for the appropriate subevent as per Eq. (8.2).

Given the above, the flow relative to the true reaction plane can be readily calculated from unit momentum vectors  $\mathbf{u}(\eta, p_t)$  for the analyzed tracks by using Eq. (8.6) for the particle relative to the  $2M$  other particles, and then dividing by the square root of Eq. (8.6) for the subevents. This gives

$$v_n(\eta, p_t) = \frac{\langle \mathbf{Q}_n \cdot \mathbf{u}(\eta, p_t) \rangle}{2\sqrt{\langle \mathbf{Q}_n^a \cdot \mathbf{Q}_n^b \rangle}}. \quad (8.7)$$

Auto-correlations are removed by subtracting particle  $i$  in the calculation of  $\mathbf{Q}$  when taking the scalar product with  $\mathbf{u}_i$ . Note that this method weights events with the magnitude of the  $\mathbf{Q}$  vector,

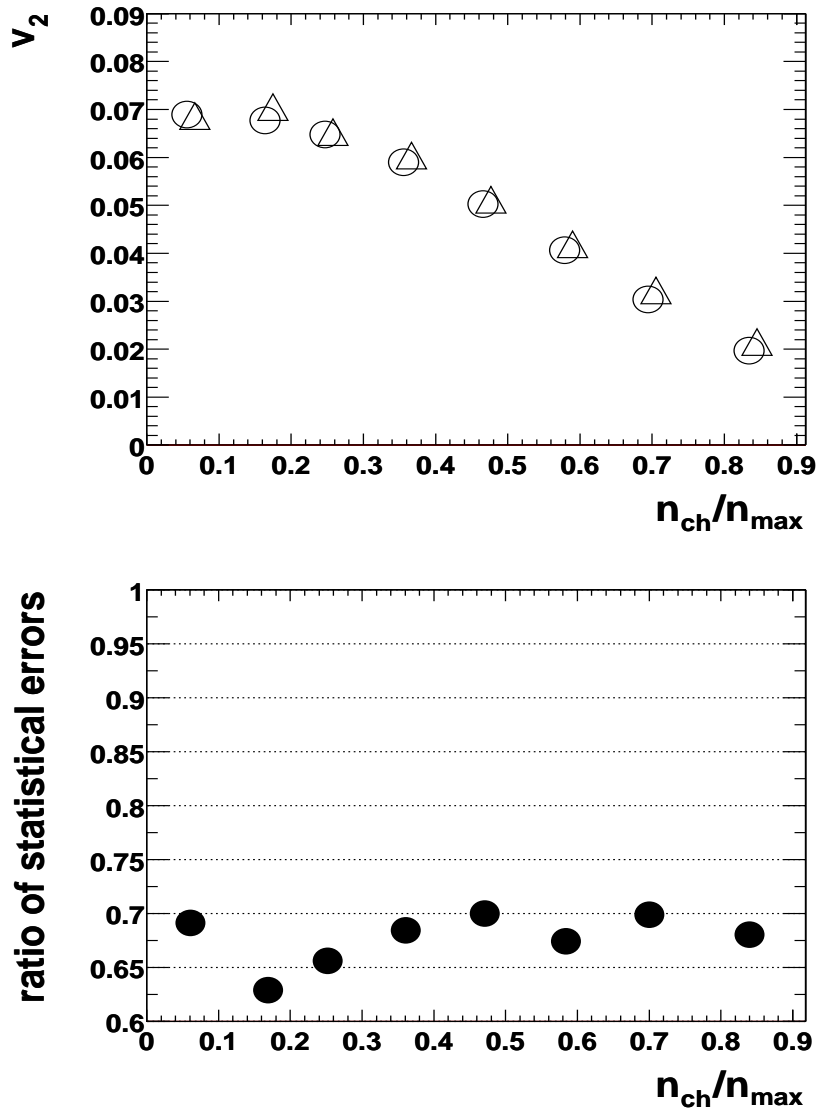


Figure 8.4: The upper panel shows  $v_2$  versus centrality using the conventional method, where the circles and triangles represent  $v_2$  with and without  $p_t$  weighting, respectively. The statistical error is smaller than the symbol size. The lower panel shows the statistical error on  $v_2$  with  $p_t$  weighting divided by the same without weighting.

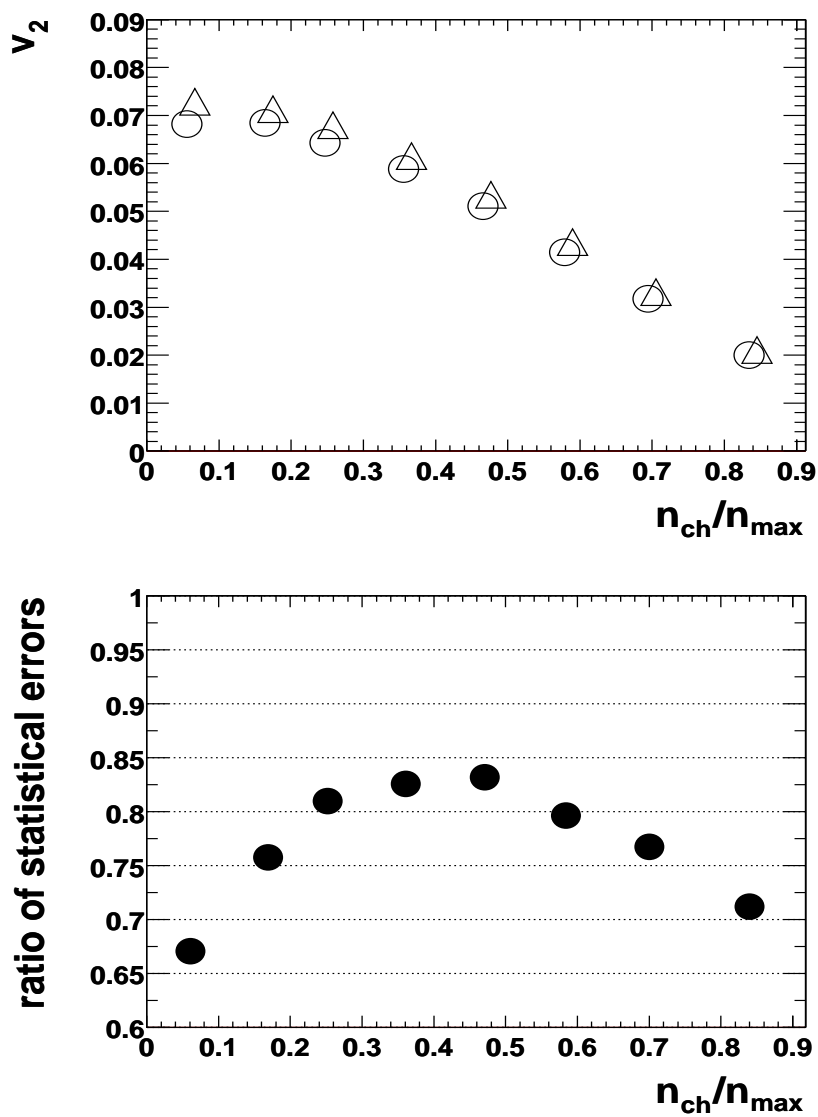


Figure 8.5: The upper panel presents  $v_2$  versus centrality from the scalar product method (triangles) and the conventional random subevent method (circles). All statistical errors are smaller than the symbol size. The statistical error for the scalar product method divided by that for the conventional method is shown in the lower panel.

and if  $\mathbf{Q}_n$  is replaced by its unit vector, the above reduces to  $\langle \cos n(\phi - \Psi) \rangle$ , the conventional correlation method.

Fig. 8.5 demonstrates that the scalar product method gives the same result as the conventional method. In this calculation, the subevents are generated by random partitioning. Monte Carlo studies indicate that the statistical error from the scalar product method is smaller than that from the conventional method if the event plane resolution is not very large. In the case of Au + Au at  $\sqrt{s_{NN}} = 130$  GeV, the event plane resolution is such that the scalar product method yields a smaller statistical error over all centrality bins compared to the conventional method, with the largest improvement being obtained for the most central and most peripheral events, where the resolutions are lowest. In addition to the benefit of reduced statistical errors, the scalar product method is very simple to implement.

### 8.3 Four-particle correlations

#### 8.3.1 Motivation for Cumulants

In experiments, it is necessary to rely on correlations between particles to determine the event plane since the reaction plane is not a direct observable. The assumption underlying conventional pair correlation analyses (including the scalar product method discussed in section 8.2.3 above) is that non-flow correlations of the type mentioned in section 8.1 are negligible compared to the flow, or at most, are comparable to other systematic uncertainties. In past studies [6, 96, 97], non-flow correlations have been discussed with specific reference to their origin, such as momentum conservation, HBT, Coulomb effect, jets, resonance decays, etc. In the first two studies of elliptic flow in STAR [7, 90], the non-flow effect was partly cancelled and partly estimated as explained in section 8.2.1. This estimate played a role in determining the systematic error on the published measurements.

Anisotropic flow is a genuine multiparticle phenomenon, which justifies use of the term *collective flow*. It means that if one considers many-particle correlations instead of just two-particle correlations, the relative contribution of non-flow effects (due to few particle clusters) should decrease. Considering many-particle correlations, one has to subtract the contribution from correlations due to lower-order multi-particles. Formally, it means that one should use cumulants [98, 99, 100, 96, 88] instead of simple correlation functions. Let us explain this with an example for four-particle correlations. The correlation between two particles is

$$\langle u_{n,1} u_{n,2}^* \rangle \equiv \langle e^{in\phi_1} e^{-in\phi_2} \rangle = v_n^2 + \delta_n, \quad (8.8)$$

where  $n$  is the harmonic, and the average is taken over all pairs of particles in a given rapidity and transverse momentum region, and over all events in an event sample. The  $\delta_n$  represents the contribution to the pair correlation from non-flow effects. Correlating four particles, one gets

$$\langle u_{n,1} u_{n,2} u_{n,3}^* u_{n,4}^* \rangle = v_n^4 + 2 \cdot 2 \cdot v_n^2 \delta_n + 2 \delta_n^2. \quad (8.9)$$

In this expression, two factors of “2” in front of the middle term correspond to the two ways of pairing (1,3)(2,4) and (1,4)(2,3) and account for the possibility to have non-flow effects in the first pair and flow correlations in the second pair and vice versa. The factor “2” in front of the last term is due to the two ways of pairing. The pure four-particle non-flow correlation is omitted from this expression — see the discussion below about the possible magnitude of such a contribution. What is remarkable is that if one subtracts from the expression (8.9) twice the square of the expression (8.8), one is left with only the flow contributions

$$\begin{aligned} & \langle \langle u_{n,1} u_{n,2} u_{n,3}^* u_{n,4}^* \rangle \rangle \\ & \equiv \langle u_{n,1} u_{n,2} u_{n,3}^* u_{n,4}^* \rangle - 2 \langle u_{n,1} u_{n,2}^* \rangle^2 = -v_n^4, \end{aligned} \quad (8.10)$$

where the notation  $\langle \langle \dots \rangle \rangle$  is used for the *cumulant*. The cumulant of order two is just  $\langle \langle u_{n,1} u_{n,2}^* \rangle \rangle = \langle u_{n,1} u_{n,2}^* \rangle$ .

In flow analysis, one is interested not only in so-called “global” flow values, but also in differential flow as function of rapidity and transverse momentum. In a four-particle correlation approach, this also can be done in a similar manner, now correlating a particle, for example in a particular  $p_t$  bin, with three particles from a common “pool”. Assuming that the particle “b” is the one from a particular bin, one gets for a differential flow study

$$\langle u_{n,b} u_{n,1}^* \rangle = v_{n;b} v_n + \delta_{n;b}, \quad (8.11)$$

where we have introduced the notation  $v_{n;b}$  for the flow value corresponding to the bin under study, and  $\delta_{n;b}$  for the corresponding non-flow contribution. Then for the correlation with three particles from the pool,

$$\begin{aligned} \langle u_{n,b} u_{n,1} u_{n,2}^* u_{n,3}^* \rangle = \\ v_{n;b} v_n^3 + 2 \cdot v_n^2 \delta_{n;b} + 2 \cdot v_n v_{n;b} \delta_n + 2 \delta_n \delta_{n;b}. \end{aligned} \quad (8.12)$$

In this case, in order to remove the non-flow contribution, one has to subtract from (8.12) twice the product of expressions (8.8) and (8.11).

$$\begin{aligned} \langle u_{n,b} u_{n,1} u_{n,2}^* u_{n,3}^* \rangle - 2 \langle u_{n,b} u_{n,1}^* \rangle \langle u_{n,1} u_{n,2}^* \rangle = \\ -v_n^3 v_{n;b}. \end{aligned} \quad (8.13)$$

Assuming that the average flow value for the particles in the pool is known, one gets the desired differential flow value for the particular bin under study.

In Eq.(8.9), we have neglected the contribution from the pure four-particle correlations due to non-flow effects. Let us now estimate the upper limit for such a contribution. Assume that *all* particles are produced via four-particle clusters. All daughters of the decay of such a cluster could in principle be within 1–2 units of rapidity from each other. Then the contribution would be

$$f/M^3, \quad (8.14)$$



where  $M$  is the *total* multiplicity within those 1–2 units of rapidity, and  $f$  is  $\langle (\cos 2(\phi_1 - \phi_2))^2 \rangle$  averaged over all cluster decay products. Assuming a perfect alignment,  $f = 1$ , and multiplicity  $M = 1000$ , this would give us the possible error in  $v_2$  measurements of the order of

$$\delta v \sim (v_2^4 + 1/1000^3)^{1/4} - v_2, \quad (8.15)$$

which would give only 2% relative error on  $v_2$  signal of 0.01, and drops very rapidly with increasing real  $v_2$  signal. Note that this calculation is for the case of 100% of the particle production via four-particle clusters and a perfect alignment of decay products. A more realistic scenario would give a much smaller estimate.

### 8.3.2 Four-subevent method

In order to apply the four-particle correlation approach to the analysis of real data, one should perform an average over all possible quadruplets of particles in a given event. Bearing in mind that the average multiplicity in a central STAR event is well beyond a thousand, it becomes a nontrivial task. The simplest way to proceed is the four-subevent method where one partitions all tracks (for example, randomly) into four groups (subevents) and calculates a flow vector for each of the groups,

$$Q_n = \sum_i u_i, \quad (8.16)$$

where the sum is over all particles in the group. Using these subevents, the problem becomes much simpler computationally. For example,

$$\langle u_{n,1} u_{n,2} u_{n,3}^* u_{n,4}^* \rangle = \langle Q_{n,1} Q_{n,2} Q_{n,3}^* Q_{n,4}^* / (M_1 M_2 M_3 M_4) \rangle, \quad (8.17)$$

where  $M_i$  are the corresponding subevent multiplicities. The cumulant calculation is straightforward:

$$\begin{aligned} \langle \langle u_{n,1} u_{n,2} u_{n,3}^* u_{n,4}^* \rangle \rangle &= \\ \langle \frac{Q_{n,1} Q_{n,2} Q_{n,3}^* Q_{n,4}^*}{M_1 M_2 M_3 M_4} \rangle & \\ - 2 \left( \langle Q_{n,1} Q_{n,2}^* / (M_1 M_2) \rangle \right)^2 &. \end{aligned} \quad (8.18)$$

The four-subevent method is relatively simple, both in logic and in implementation. The price for these benefits is lower statistical power, because the method does not take into account all possible quadruplets. A more general cumulant formalism, based on the cumulant generating function [96, 88] offers advantages for a four-particle analysis in the context of the present limited sample size.

### 8.3.3 Cumulant and generating function

The cumulant and generating function approach offers a formal and convenient way to study flow and non-flow contributions systematically. Following the method of Ref. [88], the cumulant to order four is defined by

$$\begin{aligned} \langle\langle u_1 u_2 u_3^* u_4^* \rangle\rangle &\equiv \langle u_1 u_2 u_3^* u_4^* \rangle - \\ &\langle u_1 u_3^* \rangle \langle u_2 u_4^* \rangle - \langle u_1 u_4^* \rangle \langle u_2 u_3^* \rangle, \end{aligned} \quad (8.19)$$

where, as above, the double angle bracket notation represents the cumulant expression shown explicitly on the right-hand side, and from here on, the index for the harmonic order  $n$  in the subscript of  $u$  is omitted.

The cumulant  $\langle\langle u_1 u_2 u_3^* u_4^* \rangle\rangle$  involves only pure four-particle correlations, since the two-particle correlations among the quadruplets have been explicitly subtracted away.

In the presence of flow, the cumulant becomes

$$\langle\langle u_1 u_2 u_3^* u_4^* \rangle\rangle = -v_n^4 + O\left(\frac{1}{M^3} + \frac{v_{2n}^2}{M^2}\right), \quad (8.20)$$

where  $M$  is the multiplicity of the events, the term of order  $1/M^3$  represents the remaining four-particle non-flow effects, and the term of order  $v_{2n}^2/M^2$  is the contribution of the  $2n$  higher harmonic. The cumulant to higher orders and the corresponding generalization has also been determined [88]. Likewise, the cumulant of order two reduces to the equivalent of a pair correlation analysis of the conventional type. Statistical uncertainties associated with a cumulant analysis increase with increasing order. We find that statistics from STAR year-one data are adequate for study

of the 4th-order cumulant, but it is not yet feasible to investigate orders higher than four.

The definition of the cumulant is simple, but it is tedious to calculate the moments term-by-term on the right-hand side of Eq. (8.19). Fortunately, the cumulant can be computed more easily from the generating function [88],

$$G_n(z) = \prod_{j=1}^M \left( 1 + \frac{z^* u_j + z u_j^*}{M} \right), \quad (8.21)$$

where  $z \equiv |z|e^{i\alpha}$  is an arbitrary complex number, and  $z^*$  denotes its complex conjugate.

The generating function itself has no direct physical meaning, but the coefficients of the expansion of  $\langle G_n \rangle$  in powers of  $z, z^*$  yield the correlations of interest:

$$\begin{aligned} \langle G_n \rangle &= 1 + \left\langle \frac{M-1}{M} \right\rangle |z|^2 \langle u_1 u_2^* \rangle \\ &+ \left\langle \frac{(M-1)(M-2)(M-3)}{4M^3} \right\rangle |z|^4 \langle u_1 u_2 u_3^* u_4^* \rangle + \dots \end{aligned} \quad (8.22)$$

One can use these correlations to construct the cumulants. In the limit of large  $M$ ,  $\langle G_n \rangle$  can be used to obtain the cumulant generating function directly:

$$\begin{aligned} M \cdot \left( \langle G_n(z) \rangle^{1/M} - 1 \right) &= \\ \sum_k \frac{|z|^{2k}}{(k!)^2} \langle \langle u_1 \dots u_k u_{k+1}^* \dots u_{2k}^* \rangle \rangle. \end{aligned} \quad (8.23)$$

The left-hand side of Eq. (8.23) is what is measured, and in order to extract the cumulants on the right,  $k$  equations of the form of Eq. (8.23) are needed to solve for  $k$  undetermined parameters. This can be accomplished by repeating the process with  $k$  different values of  $|z|$ . It is found that suggested magnitudes of  $|z|$  in Ref. [88], namely  $r_0 \sqrt{p}$  with  $r_0 = 1.5$  and  $p = 1, \dots, k$ , are fairly good, since results from optimized values [101] of  $r_0$  show almost no difference. Results in this dissertation are by default calculated with  $r_0 = 1.5$ .

For experimental analysis, it is sufficient to take the first three terms in Eq. (8.23). Once the cumulant has been computed, extracting the integrated flow value is straightforward because, for instance,  $v_n^4 = -\langle \langle u_1 u_2 u_3^* u_4^* \rangle \rangle$ .

When a non-unit weight is used, the integrated flow value described above becomes  $\langle w \cos n\phi' \rangle$ , which is not exactly  $v_n$  but an approximation. However, the differential flow can be calculated exactly (see below) no matter what weight is used. The integrated flow with non-unit weight can be obtained by integrating the differential flow. All integrated flow results in this dissertation (except for results from the four-subevent method) are obtained by integrating over the differential flow.

For differential flow (flow in a bin of  $\eta$  and/or  $p_t$ ), Eq. (8.23) is replaced by

$$\frac{\langle u_d G_n(z) \rangle}{\langle G_n(z) \rangle} \equiv \sum_{k,l} \frac{z^{*k} z^l}{k! l!} \langle \langle u_d u_1 \dots u_k u_{k+1}^* \dots u_{k+l}^* \rangle \rangle. \quad (8.24)$$

where  $u_d$  is the unit vector for a particle in the selected bin. Following a similar procedure as in the case of the integrated flow, the cumulant  $\langle \langle u_d u_1 u_2^* u_3^* \rangle \rangle$  is computed, but it now contains the angle of the one particle of interest and three other particles from the pool. Then the differential flow is [88]

$$v_n = - \frac{\langle \langle u_d u_1 u_2^* u_3^* \rangle \rangle}{(-\langle \langle u_1 u_2 u_3^* u_4^* \rangle \rangle)^{3/4}}. \quad (8.25)$$

Please note that Eq. 8.25 is for unit weight. It can be easily generalized for non-unit weight, and the formula still holds.

#### 8.3.4 Simulations

In order to test the cumulant method as well as the analysis procedure, the MEVSIM event generator [102] has been used to make events with various mixtures of flow and non-flow effects. In all cases, the number of simulated events in a data set is 20k, and the multiplicity is 500. Fig. 8.6 shows one such set of simulations. Nine data sets with  $v_2 = 0.10$  were produced, then a simple non-flow effect consisting of embedded back-to-back track pairs was introduced at various levels, ranging from zero up to 80 pairs per simulated event. These pairs simulate resonances which decay to two daughters with a large energy release. In Fig. 8.6, we consider the scenario where the embedded pairs themselves are correlated with the event plane with the same  $v_2 = 0.10$ . Fig. 8.6 shows

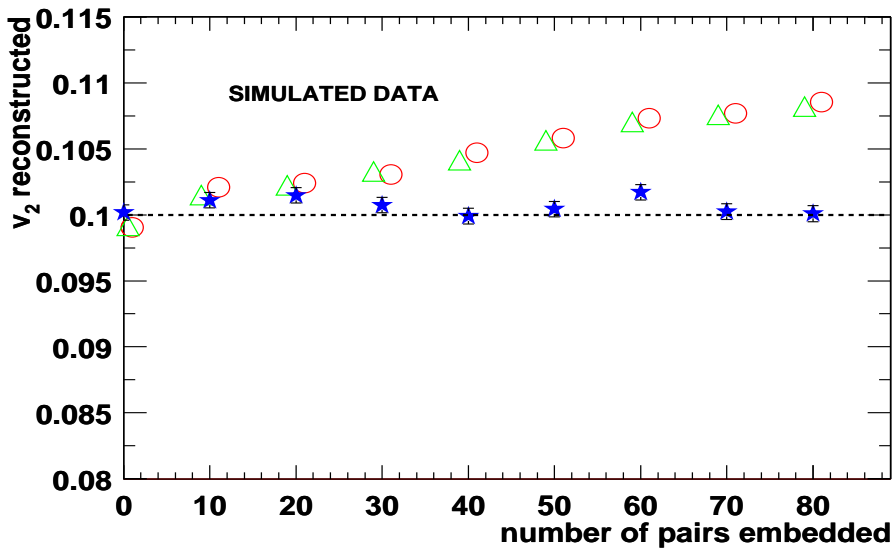


Figure 8.6: Reconstructed  $v_2$  from the conventional method (circles), from the 2nd-order cumulant method (triangles), and from the 4th-order cumulant method (stars), for simulated events as a function of number of embedded back-to-back track pairs. The horizontal dashed line marks the level of the true elliptic flow  $v_2 = 0.10$ , as imposed on the simulated events, including the back-to-back track pairs. The statistical error is smaller than the symbol size. The multiplicity for all events is 500.

that the 4th-order cumulant  $v_2$  always reconstructs the expected 10%  $v_2$ , while the  $v_2$  from the pair correlation analysis methods can only recover the correct input if non-flow pairs are not embedded.

If back-to-back pairs are instead randomly distributed in azimuth, the true flow decreases and the expected variation can be computed knowing the number of random tracks. Fig. 8.7 shows such a simulation, and again it is found that only the 4th-order cumulant  $v_2$  agrees with the expected elliptic flow, while the inferred  $v_2$  based on pair correlation analyses is distorted in the presence of the simulated non-flow effects. The role of resonances produced in real collisions may be closer to one or the other of the above two simulated scenarios, but in either case, the non-flow effect is removed by the 4th-order cumulant analysis.

In Fig. 8.8, consideration is given to the possible effect of resonances which decay with smaller energy release, having an azimuthal opening angle  $\Phi$  in the laboratory. The simulated events were generated with an imposed flow  $v_2 = 0.08$ , while in each event 50 pairs with the same  $\Phi$  were

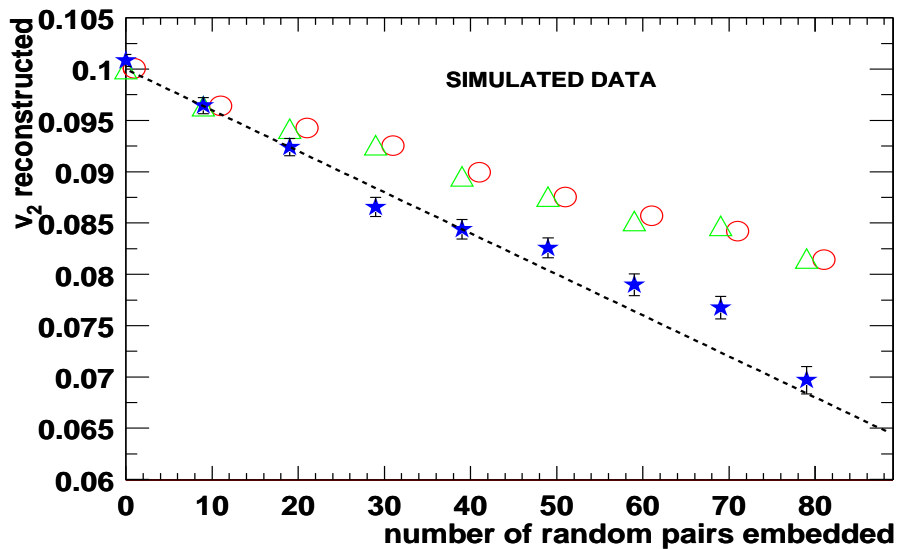


Figure 8.7: Reconstructed  $v_2$  from the conventional method (circles), from the 2nd-order cumulant method (triangles), and from the 4th-order cumulant method (stars), for simulated events as a function of number of embedded back-to-back track pairs. Unlike in the previous figure, the embedded back-to-back pairs are randomly distributed relative to the event plane, and so the true resultant  $v_2$ , indicated by the dashed line, decreases as more pairs are embedded. The multiplicity for all events is 500.

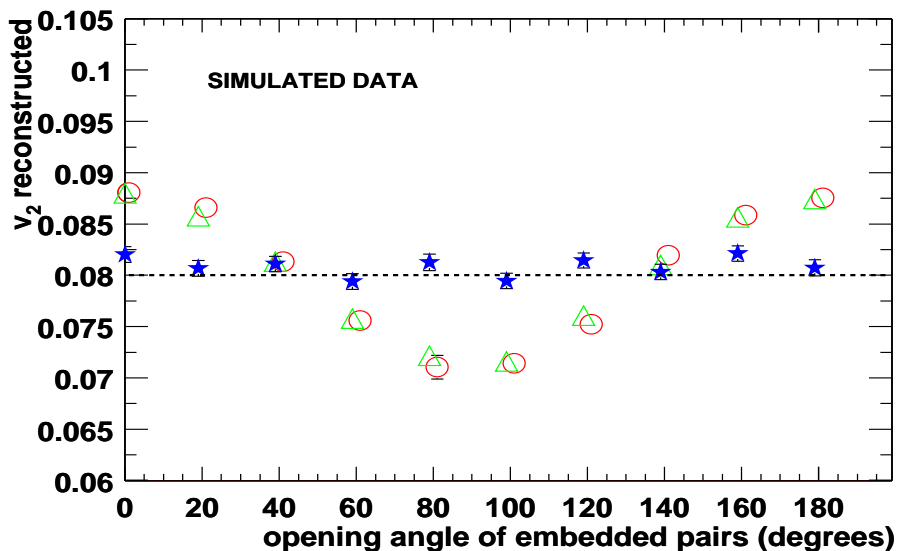


Figure 8.8: Elliptic flow from the conventional method (circles), from the 2nd-order cumulant method (triangles), and from the 4th-order cumulant method (stars), for simulated events as a function of azimuthal angle between the two tracks in each of 50 embedded pairs per event, with the 50 pairs each having random orientation relative to the event plane. The horizontal dashed line marks the level of the true elliptic flow  $v_2 = 0.08$ .

embedded, each such pair having a random orientation relative to the event plane. Ten data sets were produced, with  $\Phi$  (the abscissa in Fig. 8.8) varying in  $20^\circ$  steps between zero and  $180^\circ$ . Again, only the 4th-order cumulant  $v_2$  (stars) recovers the true elliptic flow signal.

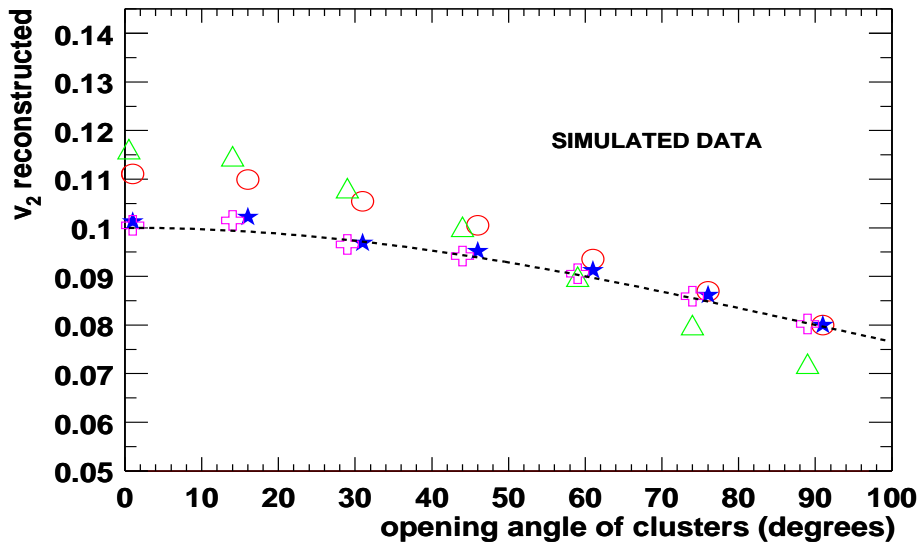


Figure 8.9: Elliptic flow from the conventional method (circles), and from the 2nd-order (triangles), 4th-order (stars), and 6th-order (crosses) cumulant methods. This is for simulated events as a function of azimuthal angle between two back-to-back track pairs. The dashed line marks the level of the true elliptic flow.

In order to test how the various methods respond to non-flow correlations associated with four-particle clusters, the simulated events in Fig. 8.9 were generated with an imposed flow  $v_2 = 0.10$ , after which 25 four-particle clusters were embedded in each event. Each cluster consists of two back-to-back pairs with an azimuthal opening angle  $\Phi$  between them. Seven data sets were produced, with  $\Phi$  (the abscissa in Fig. 8.9) varying in  $15^\circ$  steps between zero and  $90^\circ$ . The clusters were oriented such that a track bisecting  $\Phi$  would contribute to the overall flow with  $v_2 = 0.10$ . The 4th-order cumulant (stars) and the 6th-order cumulant (crosses) both reconstruct the true elliptic flow (dotted line). Note that the four-particle correlation introduced by the clusters is  $1/M^2$  times the pair correlation part, resulting in little difference between  $v_2$  from the 4th- and 6th-order cumulant methods. This result further illustrates the point (see also the end of section 8.3.1) that

non-flow effects are believed to contribute at a negligible level to the four-particle correlation, and for this reason, there may be little advantage in extending cumulant analyses to orders higher than 4.

### 8.3.5 Results from STAR

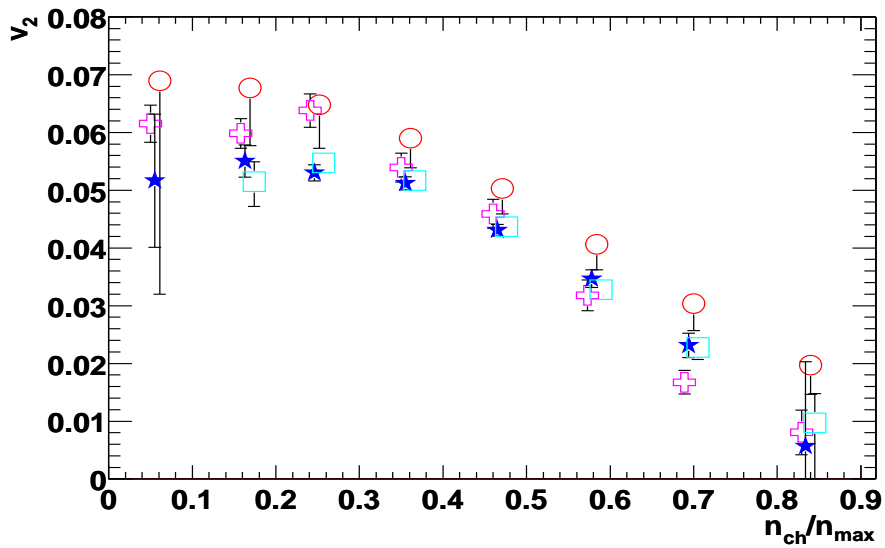


Figure 8.10: Measured elliptic flow versus centrality for Au + Au at  $\sqrt{s_{NN}} = 130$  GeV. The circles show the conventional  $v_2$  with estimated systematic uncertainty due to non-flow [104], the stars show the 4th-order cumulant  $v_2$  from the generating function, the crosses show the conventional  $v_2$  from quarter-events, and the squares show the 4th-order cumulant  $v_2$  from the four-subevent method.

Figure 8.10 shows measured elliptic flow versus centrality, where the latter as usual is characterized by charged particle multiplicity  $n_{ch}$  divided by the maximum observed charged particle multiplicity,  $n_{max}$ . The conventional  $v_2$  (circles), the 4th-order cumulant  $v_2$  from the generating function (stars), and the 4th-order cumulant  $v_2$  from the four-subevent method (squares) are compared. The cross symbols in Fig. 8.10 represent the conventional  $v_2$  signal for the case where each observed event is partitioned into four quarter-events, which are then analyzed like independent events. All tracks in each quarter-event have the same sign of charge, and the same sign of pseudorapidity. Furthermore, the event plane for quarter-events is constructed using only tracks with



$p_t < 0.5 \text{ GeV}/c$ , which serves to minimize the influence of non-flow associated with high- $p_t$  particles. It is clear that the non-flow effect is present at all centralities, and its relative magnitude is least at intermediate multiplicities.

Figure 8.11 shows  $v_2$  as a function of pseudorapidity and Fig. 8.12 shows  $v_2$  as a function of transverse momentum. The eight panels correspond to the eight centrality bins in Fig. 8.10. These results illustrate the main disadvantage of the higher-order cumulant approach compared with any of the two-particle methods, namely, larger statistical errors, and this can be seen to be a serious shortcoming in cases where simultaneous binning in several variables results in small sample sizes.

Figures 8.13 and 8.14 are again plots of elliptic flow versus pseudorapidity and versus transverse momentum, respectively. Here the  $v_2$  is integrated over centrality bins 2 through 7. Bins 1 and 8 are not included in this average, otherwise they would significantly increase the statistical error on the result.

The 4th-order cumulant  $v_2$  is systematically about 15% lower than the conventional pair and cumulant pair calculations, indicating that non-flow effects contribute to  $v_2$  analyses of the latter kind. The  $v_2$  signal based on quarter-events (as defined in the discussion of Fig. 8.10) is closer to the 4th-order cumulant, although still larger on average, implying that this pair analysis prescription is effective in removing some, but not all, non-flow effects.

Figure 8.14 verifies that the  $v_2(p_t)$  curve flattens above  $2 \text{ GeV}/c$  [104]. There is theoretical interest in the question of whether or not  $v_2(p_t)$  continues flat at higher  $p_t$  or eventually goes down [50], but the statistics of year-one data from STAR are not sufficient for addressing this question via a four-particle cumulant analysis.

Figure 8.15 presents the  $p_t$ -dependence of the correction factor for non-flow. Within errors, the non-flow effect is seen to be about the same from zero through  $p_t \sim 4 \text{ GeV}/c$  — a somewhat surprising result, given the presumption that the processes responsible for non-flow are different at low and high  $p_t$ . Figure 8.16, which presents  $v_2$  from quarter-events divided by the conventional

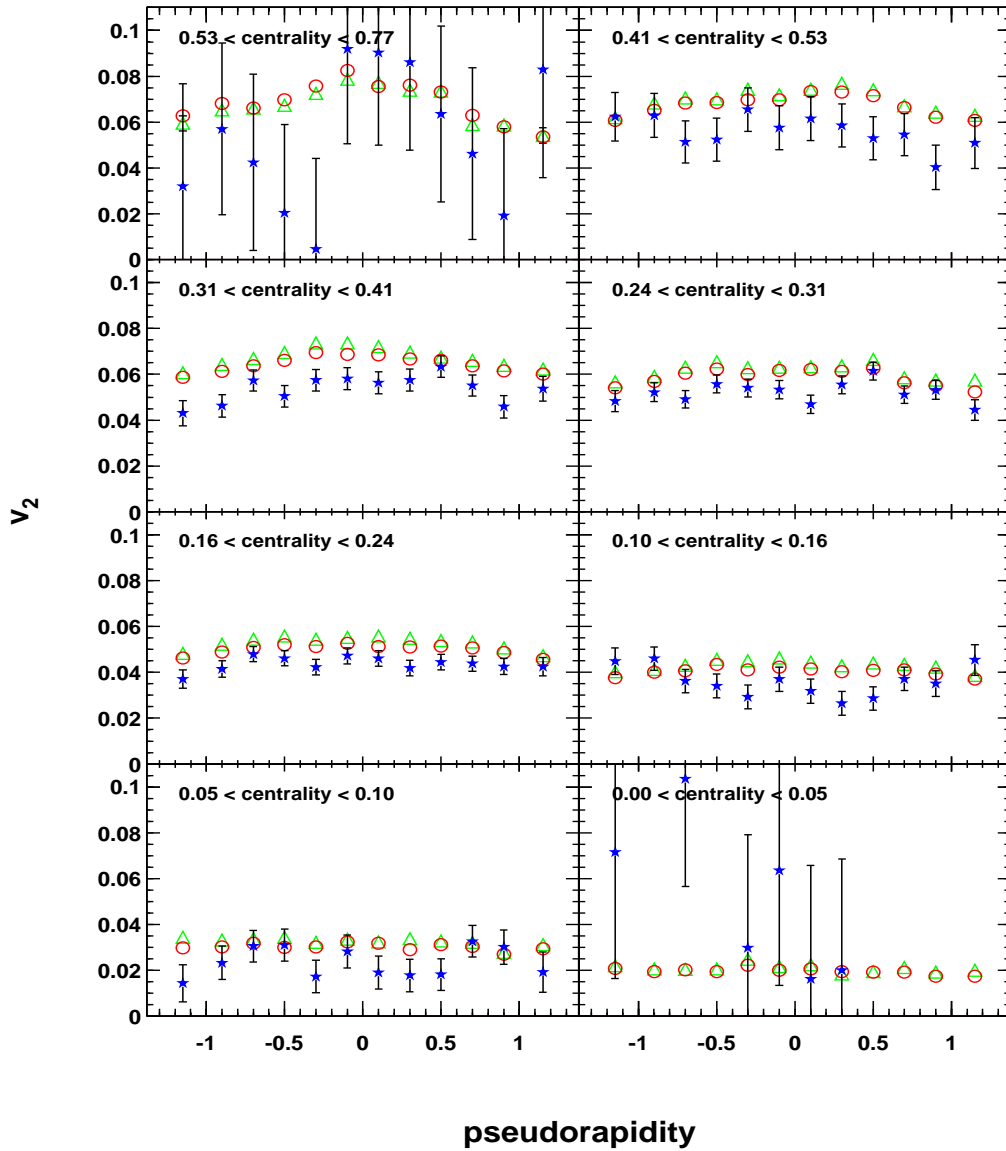


Figure 8.11: Reconstructed  $v_2$  versus pseudorapidity from the conventional method (circles), from the 2nd-order cumulant method (triangles), and from the 4th-order cumulant method (stars), in eight centrality bins. The upper left panel shows the most peripheral events, and the lower right the most central.

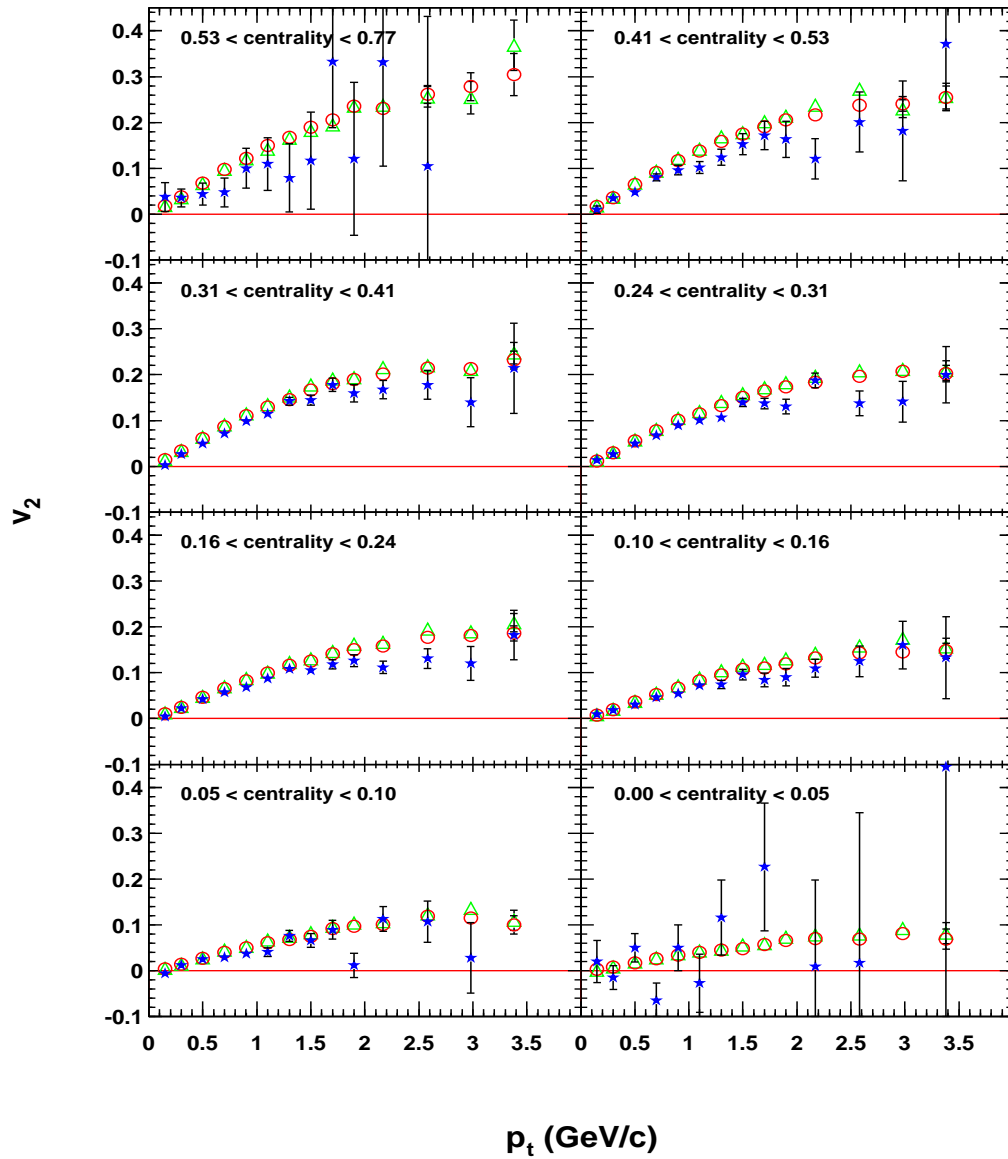


Figure 8.12: Reconstructed  $v_2$  versus  $p_t$  from the conventional method (circles), from the 2nd-order cumulant method (triangles), and from the 4th-order cumulant method (stars), in eight centrality bins. The upper left panel shows the most peripheral events, and the lower right the most central.

$v_2$ , both based on event planes constructed from particles with  $p_t < 0.5$  GeV/ $c$ , offers a useful insight regarding the approximate  $p_t$ -independence of non-flow. This ratio roughly characterizes the contribution to non-flow from resonance decays and from other sources which primarily affect  $v_2$  at lower  $p_t$ , whereas non-flow from (mini)jets ought to be about equally present in the numerator and the denominator of the ordinate in Fig. 8.16. A comparison of Figs. 8.15 and 8.16 accordingly does not contradict the implicit assumption that different phenomena dominate non-flow in different  $p_t$  regions, and implies that the total resultant non-flow correction by coincidence happens to be roughly the same throughout the  $p_t$  range under study.

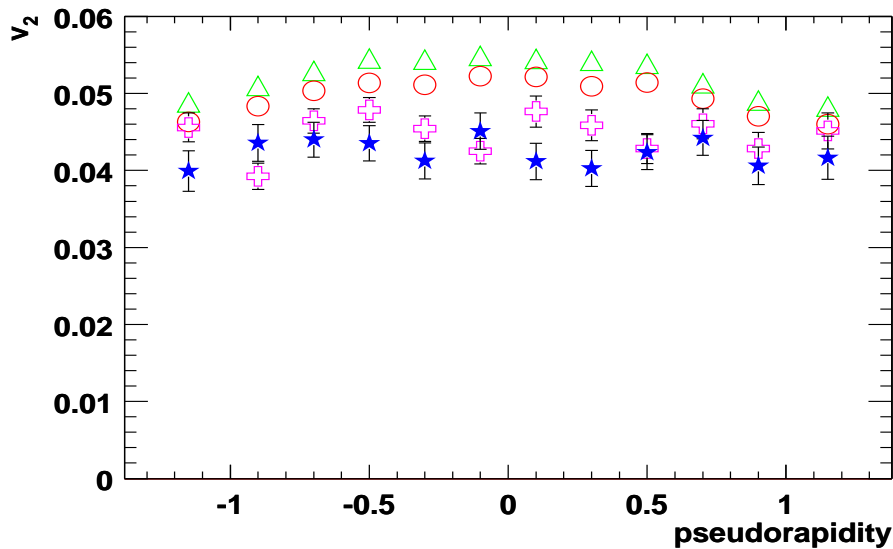


Figure 8.13: Elliptic flow versus pseudorapidity from the conventional method (circles), from the 2nd-order cumulant method (triangles), from quarter-events (crosses), and from the 4th-order cumulant method (stars), averaged over all centralities from bin 2 through 7, as defined in Figs. 8.11 and 8.12.

Following the approach of Section 8.2.2, the options of weighting each track by either unity or  $p_t$  have been compared in the 4th-order cumulant analysis. Fig. 8.17 demonstrates that the STAR results are consistent in the two cases, and the  $p_t$  weighting yields smaller statistical errors. All STAR results presented in this dissertation are computed with  $p_t$  weighting unless otherwise stated.

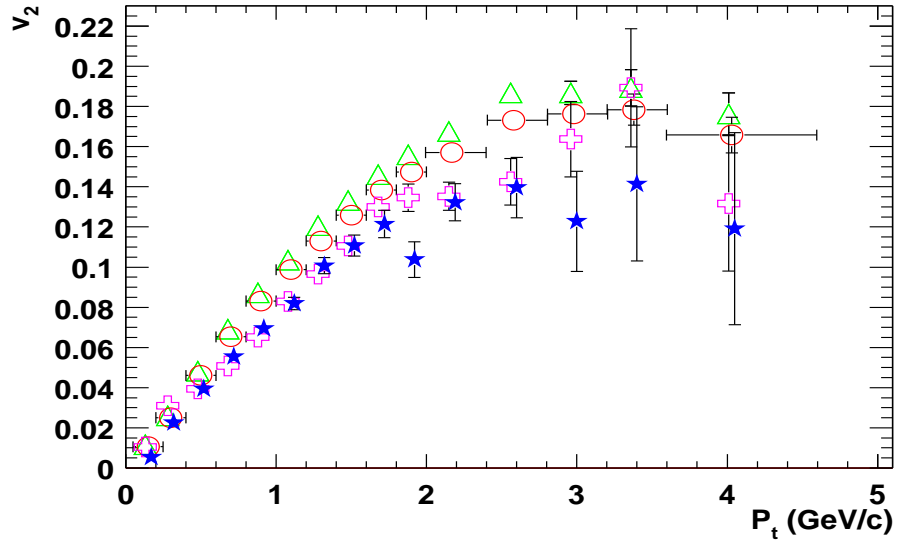


Figure 8.14: Elliptic flow versus transverse momentum from the conventional method (circles), from the 2nd-order cumulant method (triangles), from quarter-events (crosses), and from the 4th-order cumulant method (stars), averaged over all centralities from bin 2 through 7, as defined in Figs. 8.11 and 8.12.

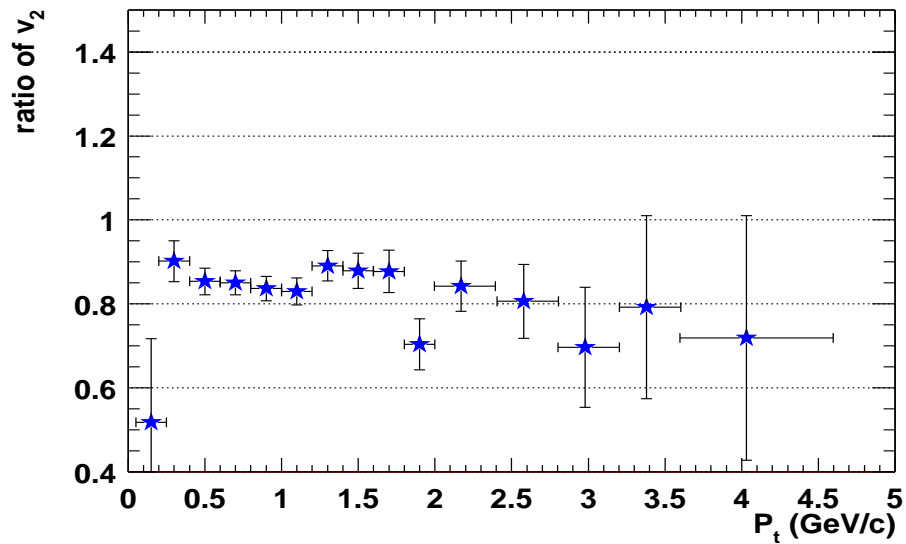


Figure 8.15: The ratio of  $v_2$  from the 4th-order cumulant divided by  $v_2$  from the conventional method as a function of  $p_t$ , averaged over all centralities from bin 2 through 7, as defined in Figs. 8.11 and 8.12.

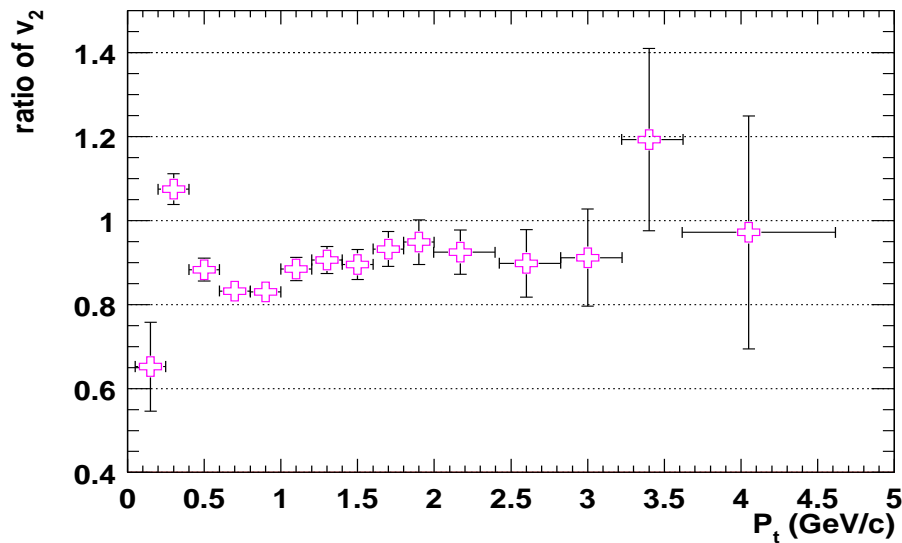


Figure 8.16: The ratio of  $v_2$  from quarter-events divided by the conventional  $v_2$  as a function of  $p_t$ . In both cases, event planes were constructed from low  $p_t$  ( $< 0.5$  GeV/c) particles. The data are averaged over all centralities from bin 2 through 7, as defined in Figs. 8.11 and 8.12.

#### 8.4 Elliptic flow fluctuations

High precision results presented in this dissertation become sensitive to another effect usually neglected in flow analysis, namely, event-by-event flow fluctuations. The latter can have two different origins: “real” flow fluctuations — fluctuations at fixed impact parameter and fixed multiplicity (see, for example [103]) — and impact parameter variations among events from the same centrality bin in a case where flow does not fluctuate at fixed impact parameter. Note that these effects are in principle present in any kind of analysis, including the “standard” one based on pair correlations. The reason is that any flow measurements are based on correlations between particles, and these very correlations are sensitive only to certain moments of the distribution in  $v_2$ . In the pair correlation approach with the reaction plane determined from the second harmonic, the correlations are proportional to  $v^2$ . After averaging over many events, one obtains  $\langle v^2 \rangle$ , which in general is not equal to  $\langle v \rangle^2$ . The 4-particle cumulant method involves the difference between 4-particle correlations and (twice) the square of the 2-particle correlations. Everywhere in this chapter, we assume that this

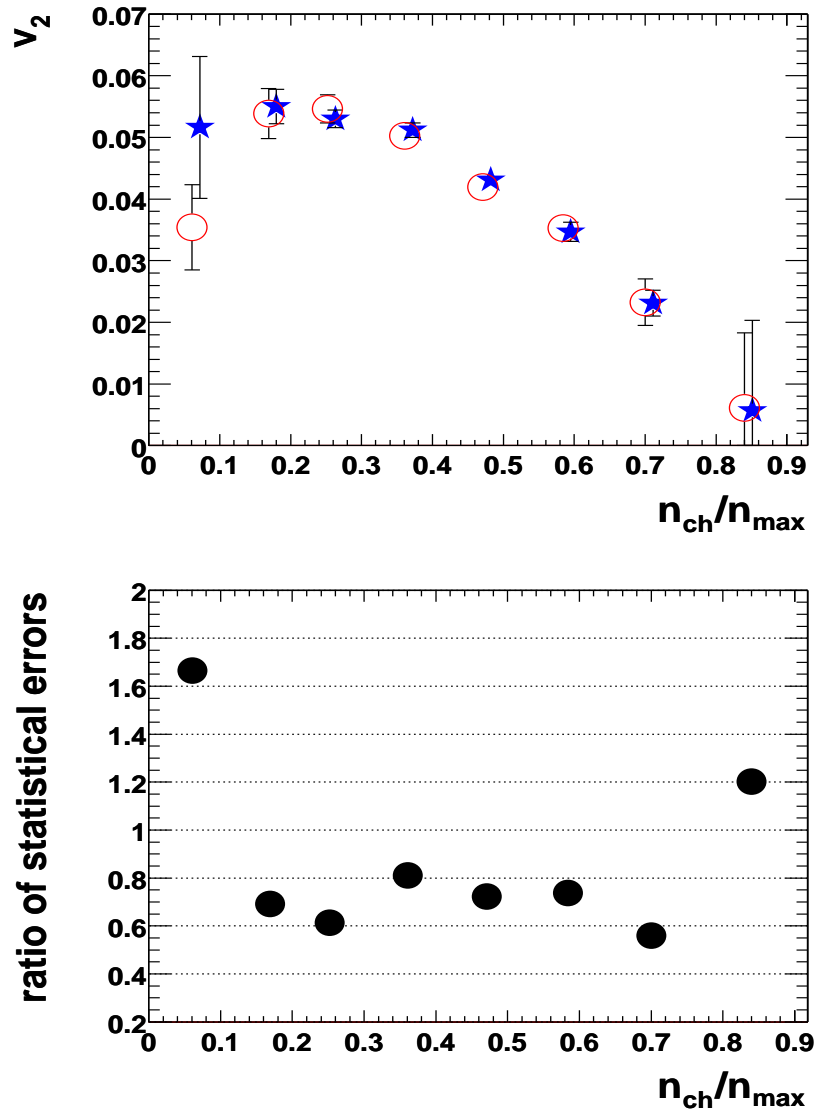


Figure 8.17: Measured  $v_2$  from 4th-order cumulants versus centrality with  $p_t$  weighting (stars) and unit weighting (circles).

difference comes from correlations in the non-flow category. Note, however, that in principle this difference ( $\langle v^4 \rangle - \langle v^2 \rangle^2 \neq 0$ ) could be due to flow fluctuations. Let us consider an example where the distribution in  $v$  is flat from  $v = 0$  to  $v = v_{\max}$ . Then, a simple calculation would lead to the ratio of the flow values from the standard 2-particle correlation method and 4-particle cumulants as large as  $\langle v^2 \rangle^{1/2} / (2\langle v^2 \rangle^2 - \langle v^4 \rangle)^{1/4} = 5^{1/4} \approx 1.5$ .

In this study, we consider the possible bias in elliptic flow measurements under the influence of impact parameter fluctuations within the studied centrality bins. The largest effect is expected within the bin of highest multiplicity, where the impact parameter and  $v_2$  are both known *a priori* to fluctuate down to zero in the limit of the most central collisions. These fluctuations lead to bin-width-dependent bias in the extracted  $v_2$  measurements.

In section 8.3, two approximations were made in order to extract the final flow result,

$$\langle v_n^4 \rangle \simeq \langle v_n^2 \rangle^2 \text{ and } \langle v_n^2 \rangle \simeq \langle v_n \rangle^2 .$$

Taking into account the fluctuation of  $v_n$ ,

$$\langle v_n^4 \rangle = \sigma_{v_n^2}^2 + \langle v_n^2 \rangle^2 \text{ and } \langle v_n^2 \rangle = \sigma_{v_n}^2 + \langle v_n \rangle^2 ,$$

and Eq. (8.19) becomes, after a few steps that are not shown,

$$-v_n^4 - 2\sigma_{v_n}^2 v_n^2 - \sigma_{v_n}^4 + \sigma_{v_n^2}^2 = -v_{\text{meas}}^4 , \quad (8.26)$$

which is a function of  $v_n$  and is solvable for  $v_n$ , if  $\sigma_{v_n}^2$  and  $\sigma_{v_n^2}^2$  are known. A method of calculating both  $\sigma_{v_n}^2$  and  $\sigma_{v_n^2}^2$  is now presented.

First, we need to parameterize  $v_n$  as a function of impact parameter,  $b$ . Consider a polynomial fit  $v_n = a_0 + a_1 b + \dots + a_6 b^6$ , in which case the measured flow is  $\langle v_n \rangle = a_0 + a_1 \langle b \rangle + \dots + a_6 \langle b^6 \rangle$ . The various averages  $\langle b \rangle, \langle b^2 \rangle, \dots, \langle b^{12} \rangle$  can be estimated in each centrality bin from filtered HIJING events. The parameters  $a_i$  have been determined by minimizing  $\chi^2$  in a fit to the eight  $v_2(n_{\text{ch}})$  measurements. In addition, the fit is constrained to go through  $v_2 = 0$  at  $b = 0$  and at  $b = 14.7$  fm [105]. Fig. 8.18 shows the resulting curve:



$$\begin{aligned}
v_2(b) = & -0.000394 b + 0.0021 b^2 \\
& -0.0000706 b^3 - 0.0000320 b^4 + \\
& 0.00000358 b^5 - 1.174 \times 10^{-7} b^6.
\end{aligned} \tag{8.27}$$

In principle, the final corrected  $v_2(n_{\text{ch}})$  should be determined iteratively, but the result is stable on the first iteration.

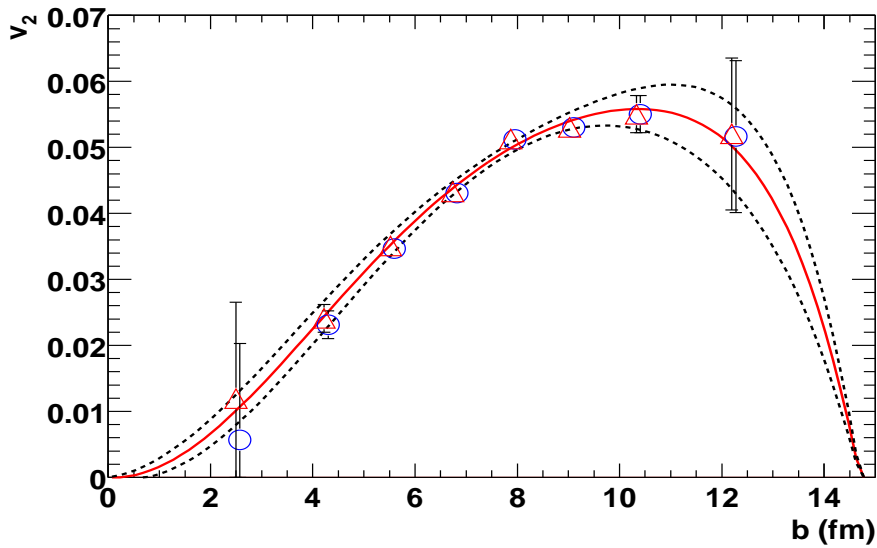


Figure 8.18:  $v_2$  as a function of impact parameter based on measured data, using HIJING to infer the impact parameter. The triangles are the final 4th-order cumulant data after correction for fluctuations as described in Section 8.4, while the circles show the 4th-order cumulant data before this correction. The dashed lines represent the estimated uncertainty in the parametrization represented by the solid curve.

Next we consider

$$\begin{aligned}
\sigma_{v_n}^2 = & \langle v_n^2 \rangle - \langle v_n \rangle^2 = \\
& (a_0^2 + 2a_0 a_1 \langle b \rangle + \dots a_6^2 \langle b^{12} \rangle) - \\
& (a_0 + a_1 \langle b \rangle + \dots a_6 \langle b^6 \rangle)^2,
\end{aligned} \tag{8.28}$$

and again the various averages of powers of  $b$  can be estimated using HIJING.

After computing  $\sigma_{v_n}^2$ ,  $\sigma_{v_2}^2$ , and obtaining  $v_{\text{meas}}$  from the four-particle correlation method, Eq. (8.26) can be solved to extract the  $v_n$  corrected for impact parameter fluctuations. The  $v_2$  bias is found to be entirely negligible in all the studied centrality bins except for the most central, where the correction is about a factor of two (see the leftmost bin in Fig. 8.18). In the present analysis, even a factor of two is not significant due to the large statistical error on  $v_2$  for maximum centrality. However, the correction to  $v_2$  resulting from finite centrality bin width at maximum centrality has been determined with lower uncertainty than  $v_2$  itself, and will become quite important in future studies with large samples of events.

Real event-by-event fluctuation in the flow coefficients would also make the four-particle values lower than the two-particle values. At the moment, there is no way to calculate this effect, although it is expected to be small.

$N_{ch}$	cross section	$b$ (fm)	$\epsilon$	$v_2$
$53_{33}^{47}$	53 – 77%	$12.23 \pm 0.006$	0.420	$0.052 \pm 0.012$
$140_{40}^{40}$	41 – 53%	$10.36 \pm 0.006$	0.415	$0.055 \pm 0.003$
$227_{47}^{43}$	31 – 41%	$9.06 \pm 0.006$	0.371	$0.053 \pm 0.001$
$319_{49}^{41}$	24 – 31%	$7.91 \pm 0.007$	0.319	$0.051 \pm 0.001$
$415_{55}^{45}$	16 – 24%	$6.80 \pm 0.008$	0.261	$0.043 \pm 0.001$
$519_{59}^{41}$	10 – 16%	$5.56 \pm 0.009$	0.197	$0.035 \pm 0.002$
$622_{62}^{38}$	5 – 10%	$4.26 \pm 0.011$	0.131	$0.023 \pm 0.002$
$746_{86}^{124}$	top 5%	$2.53 \pm 0.013$	0.058	$0.012 \pm 0.015$

Table 8.1: Tabulated values of observed charged particle multiplicity, centrality in terms of percent of total geometric cross section, impact parameter inferred from HIJING, the initial spatial anisotropy  $\epsilon$ , and the final corrected elliptic flow based on 4th-order cumulants.

## 8.5 The centrality dependence of elliptic flow

The centrality dependence of elliptic flow is a good indicator of the degree of equilibration reached in the reaction [71, 106]. Following Ref. [105], we compute the initial spatial eccentricity

for a Woods-Saxon distribution with a wounded nucleon model [73] from

$$\epsilon = \frac{\langle y^2 \rangle - \langle x^2 \rangle}{\langle y^2 \rangle + \langle x^2 \rangle}$$

where  $x$  and  $y$  are coordinates in the plane perpendicular to the beam and  $x$  denotes the in-plane direction. The ratio  $v_2/\epsilon$  is of interest because it has been argued to be independent of centrality in a hydrodynamic model with constant speed of sound [4]. Hydrodynamics represents one possible limiting case in describing nuclear collisions — the limit where the mean free path for interaction of the constituents represented by the fluid cells is very small compared with the region of nuclear overlap. The opposite limit, where the mean free path is long (or at least comparable to the dimensions of the nuclear overlap region) is normally known as the Low Density Limit (LDL). In nuclear transport models, the mean number of hard binary interactions per particle is typically small, and the predictions of these models tend to be closer to the low density limit than the hydro limit. In order to judge the proximity of measured flow data to either of these limits, it is useful to plot, as in Fig. 8.19,  $v_2/\epsilon$  versus charged particle density in the form  $(dN/dy)/S$ , where  $dN/dy$  is rapidity density, and the area of the overlap region is  $S = \pi \sqrt{\langle x^2 \rangle \langle y^2 \rangle}$  as computed above. Since  $v_2/\epsilon$  is proportional to  $(dN/dy)/S$  in the LDL case [74, 71], this form of plot offers meaningful insights without reference to detailed theoretical models.

Figure 8.19 presents Au + Au data from AGS/E877 [107, 108], from NA49 [106], as well as the current STAR measurements based on 4th-order cumulants, corrected for fluctuations as detailed in Section 8.4. Alternative forms of the centrality dependence can readily be generated using the tabulated quantities presented in Table 8.1. Generally, the current STAR results underline the need for much increased statistics, particularly for the most central collisions. Within the uncertainties, a smooth trend of increasing  $v_2/\epsilon$  with increasing centrality (larger  $(dN/dy)/S$ ) is observed, without the kink that has been suggested as a phase transition signature [72, 74]. It is noteworthy that the  $v_2/\epsilon$  values reached in the most central RHIC collisions are consistent with the hydrodynamic limit [4, 69, 75], whereas  $v_2/\epsilon$  in central collisions at AGS and SPS is significantly lower. It is

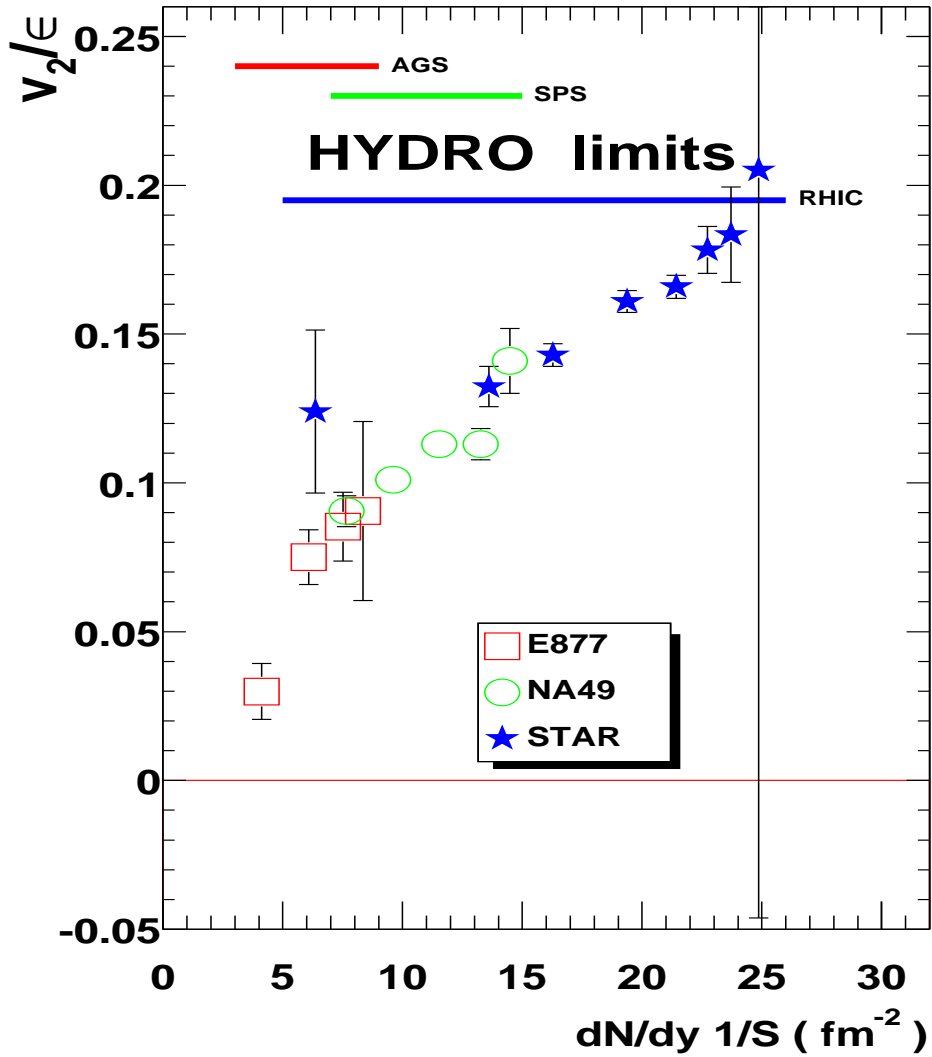


Figure 8.19:  $v_2/\epsilon$  as a function of charged particle density in Au + Au collisions. Data are from E877 at the AGS (squares), NA49 at the SPS (circles), and STAR at RHIC (stars). The STAR measurements are at  $\sqrt{s_{NN}} = 130$  GeV, and correspond to the final corrected elliptic flow based on 4th-order cumulants, and we assume  $dN/dy = dN/d\eta$ . The horizontal shaded bands indicate the hydrodynamic limits for different beam energies.

also worthy of note that while the roughly linear relationship between  $v_2/\epsilon$  and  $(dN/dy)/S$  across the presented beam energies and centralities is consistent with the LDL picture [74], the measured  $v_2(p_t)$  (Fig. 8.14) cannot be explained by current LDL implementations [109], and is much closer to hydrodynamic calculations up to 2 GeV/ $c$  [109].

Our theoretical understanding of the postulated QGP phase of matter remains in a state of flux, and the search for experimental QGP signatures is an on-going effort at RHIC. No single observable such as elliptic flow can provide an unambiguous answer to the main questions, and we must wait for a stable set of measurements covering the full range of signals discussed in Chapter 2. Nevertheless, it is possible to make some predictions about the likely role of the present elliptic flow measurements in complementing the information now emerging from other analyses.

The agreement between hydrodynamic calculations and the integrated elliptic flow in central collisions is consistent with early local thermal equilibrium, and the deviation observed in non-central collisions indicates that the amount of particle rescattering at the larger impact parameters is insufficient to justify the local thermal approximation implicit in hydrodynamical models. The hydrodynamic-motivated blast-wave model [77, 110] suggests that elliptic flow is generated by the combination of an azimuthal velocity variation and a spatially anisotropic freeze-out hypersurface, and it successfully reproduced the mass dependence of  $v_2$  as a function of  $p_t$  in the low  $p_t$  region [90], as well as the invariant  $m_T$  spectra for various particle species [111].

The origin of elliptic flow is the initial spatial anisotropy, which is clearly an elongation in the *out-of-plane* direction. As the collision evolves, it is inferred that the source in momentum space becomes extended in the *in-plane* direction at RHIC energies (see section 4.3 for details). Reaction-plane-sensitive HBT, by taking account of elliptic flow, can measure the elliptic geometry of the source in coordinate space at thermal freeze-out, and also provides information about the time scale of the freeze-out. Preliminary studies [112] indicate an *out-of-plane* source, which is consistent with a short lifetime of the fireball. The evolution of the elliptic geometry of the source can also

be probed by comparing  $v_2$  from short-lived particles, like  $K^*$  [113], to averaged  $v_2$  for all particles. Results also need to be reconciled with balance function analyses [114], which measure the *hadronization* time scale based on the assumption that charge/anti-charge pairs become progressively more separated in rapidity the longer the time during which they undergo rescattering after production.

High  $p_t$  studies [115, 116] show that spectra suppression at high  $p_t$  is in qualitative agreement with the predictions of energy loss by scattered partons traversing a dense medium, and the same argument is supported by the angular correlation among high  $p_t$  particles [117]. The density profile of the medium can be inferred by comparing  $v_2$  at high  $p_t$  to model calculations [50]. To draw meaningful conclusions, accurate measurements of  $v_2$  at high  $p_t$  are necessary. However, as discussed in section 8.3.5,  $v_2$  at high  $p_t$  suffers a significant non-flow contribution from jets, and thus a four-particle flow analysis of the type presented in this dissertation, but with much increased statistics, is of special importance.

## Summary and Outlook

Elliptic flow provides direct insight into the early stage of heavy ion collisions. With other observables, elliptic flow builds the picture of the evolution of the hot dense matter created by the collision. Elliptic flow is the subject of several proposed phase transition signatures, however, many of those proposed signals are subtle effects, and it is thus important to measure the elliptic flow with the least possible systematic uncertainty.

In this work, we provide details of the approach for treating non-flow correlations within the framework of the standard elliptic flow analysis method based on particle pairs. We also compare the standard method with a new and simpler pair analysis based on the scalar product of flow vectors. The latter yields a 15 – 35% reduction in statistical errors, with the best improvement occurring in the case of the most central and the most peripheral events.

It is concluded that four-particle correlation analyses can reliably separate flow and non-flow correlation signals, and the latter account for about 15% of the observed second-harmonic azimuthal correlation in year-one STAR data. The cumulant approach has demonstrated some advantages over the previous alternatives for treating non-flow effects. In particular, 4th-order cumulants allows us to present  $v_2$  measurements fully corrected for non-flow effects, in contrast to the earlier analyses where the non-flow contribution was partly removed and partly quantified by the reported systematic uncertainties. It is observed that non-flow correlations are present in  $\sqrt{s_{NN}} = 130$  GeV Au + Au events throughout the studied region  $|\eta| < 1.3$  and  $0.1 < p_t < 4.0$  GeV/ $c$ , and are present at all centralities. The largest contribution from non-flow correlations is found among the most peripheral and the most central collisions.

On the other hand, a 4th-order cumulant analysis is subject to larger statistical errors than a

conventional pair correlation analysis of the same data set. In the case of year-one data from STAR, the intrinsic advantages of a higher-order analysis are somewhat offset by the increased statistical errors, but in the case of future studies of larger numbers of events, a higher-order analysis will provide a clear advantage.

Fluctuations within the studied multiplicity bins have the potential to bias elliptic flow results. This bias has been estimated and found to be entirely negligible except for the most central multiplicity bin, where the correction is about a factor of two. In the present analysis, even this large bias is only marginally significant, but again, this correction will presumably be quite important in future studies with much improved statistics.

We present STAR data for  $v_2/\epsilon$  — elliptic flow in various centrality bins, divided by the initial spatial eccentricity for those centralities. Mapping centrality onto a scale of charged particle density enables us to study a broad range of this quantity, from peripheral AGS collisions, through SPS, and ending with central RHIC collisions. Within errors, the STAR data follow a smooth trend and show no evidence of predicted phase transition signatures. The three experiments at widely differing beam energies show good agreement in  $v_2/\epsilon$  where they overlap in their coverage of particle density. The pattern of  $v_2/\epsilon$  being roughly proportional to particle density continues over the density range explored at RHIC, which is consistent with a general category of models which approximate the low density limit as opposed to the hydrodynamic limit. On the other hand,  $v_2/\epsilon$  at STAR is consistent with having just reached the hydrodynamic limit for the most central collisions. The present data contains no hint of the expected saturation of  $v_2/\epsilon$  at the hydrodynamic limit. It will be interesting to repeat the study for  $\sqrt{s_{NN}} = 200$  GeV Au + Au events.

The agreement between hydrodynamic calculations and the integrated elliptic flow in central collisions is consistent with early local thermal equilibrium, The same argument is supported by the fact that the hydrodynamic-motivated blast-wave model successfully reproduced the mass dependence of  $v_2$  as a function of  $p_t$  in the low  $p_t$  region, as well as the invariant  $m_T$  spectra for various



particle species. Reaction-plane-sensitive HBT measurements, by taking account of elliptic flow, indicate a short lifetime of the fireball in non-central collisions, which is qualitatively consistent with a delayed hadronization in central collisions suggested by balance function analyses.  $v_2$  at high  $p_t$  is sensitive to initial gluon density but it suffers a significant non-flow contribution from jets, and thus a four-particle flow analysis of the type presented in this dissertation, but with much increased statistics, is of special importance.

This experimental analysis is the first systematic study of elliptic flow based on four particle correlations. The work presented in this dissertation, together with the information emerging from other analyses, is now beginning to build the “big picture” that should soon provide a comprehensive understanding of the exciting physics of heavy ion collisions at the high energy frontier.

## References

- [1] For reviews and recent developments, see Quark Matter 2001 proceedings. (2001).
- [2] W. Reisdorf, and H. G. Ritter, Collective flow in heavy-ion collisions. *Annu. Rev. Nucl. Part. Sci.* **47**, 663 (1997).
- [3] N. Herrmann, J. P. Wessels, and T. Wienold, Collective flow in heavy ion collisions. *Annu. Rev. Nucl. Part. Sci.* **49**, 581 (1999).
- [4] J. -Y. Ollitrault, Anisotropy as a signature of transverse collective flow. *Phys. Rev.* **D46**, 229 (1992).
- [5] S. Voloshin and Y. Zhang, Flow study in relativistic nuclear collisions by fourier expansion of azimuthal particle distributions. *Z. Phys.* **C70**, 665 (1996).
- [6] A. M. Poskanzer and S. A. Voloshin, Methods for analyzing anisotropic flow in relativistic nuclear collisions. *Phys. Rev.* **C58**, 1671 (1998).
- [7] STAR collaboration, K.H. Ackermann *et al.*, Elliptic Flow in Au + Au Collisions at  $\sqrt{s_{NN}} = 130$  GeV. *Phys. Rev. Lett.* **86**, 402 (2001).
- [8] J. Jiang *et al.*, High-order collective-flow correlations in heavy-ion collisions. *Phys. Rev. Lett.* **68**, 2739 (1992).
- [9] A Dumitru, U. Katscher, J. A. Maruhn, H. Stöcker, W. Greiner and D. H. Rischke, Thermal photons as a measure for the rapidity dependence of the temperature. *Z. Phys.* **A353**, 187 (1995)
- [10] J. D. Bjorken, Highly relativistic nucleus-nucleus collisions: the central rapidity region. *Phys. Rev.* **D27**, 140 (1983)
- [11] J. Alam, D. K. Srivastava, B. Sinha and D.N. Basu, Transverse flow effects on high-energy photons emitted by expanding quark-gluon plasma. *Phys. Rev.* **D48**, 1117 (1993)
- [12] A. Dumitru, U. Katscher, J. A. Maruhn, H. Stöcker, W. Greiner and D. H. Rischke, Pion and thermal photon spectra as a possible signal for a phase transition. *Phys. Rev.* **C51**, 2166 (1995)
- [13] J. J. Neumann, D. Seibert and G. Fai, Thermal photon production in high-energy nuclear collisions. *Phys. Rev.* **C51**, 1460 (1995)
- [14] K. Geiger and J. Kapusta, Dilepton radiation from cascading partons in ultrarelativistic nuclear collisions. *Phys. Rev. Lett.* **70**, 1920 (1993)
- [15] B. Kampfer and O. P. Pavlenko, Dilepton radiation from nonequilibrium parton matter produced in ultrarelativistic heavy ion collisions. *Phys. Lett.* **B289**, 127 (1992)

- [16] E. V. Shuryak and L. Xiong, Dilepton radiation from cascading partons in ultrarelativistic nuclear collisions. *Phys. Rev. Lett.* **70**, 2241 (1993)
- [17] S. D. Drell and T. M. Yan, Massive Lepton-Pair Production in Hadron-Hadron Collisions at High Energies. *Phys. Rev. Lett.* **25**, 316 (1970)
- [18] C. Gale and J. I. Kapusta, Dilepton radiation from high temperature nuclear matter. *Phys. Rev.* **C35**, 2107 (1987)
- [19] F. Karsch, K. Redlich, and L. Turko, Chiral symmetry and dileptons in heavy ion collisions. *Z. Phys.* **C60**, 519 (1995)
- [20] D. Lissauer and E. V. Shuryak,  $K$  meson modification in hot hadronic matter may be detected via  $\phi$  meson decays. *Phys. Lett.* **B253**, 15 (1991)
- [21] P. Z. Bi and J. Rafelski, Decay of  $\phi$  in hot matter. *Phys. Lett.* **B262**, 485 (1991)
- [22] M. Asakawa and C. M. Ko, Seeing the QCD phase transition with  $\phi$  mesons. *Phys. Lett.* **B322**, 33 (1994)
- [23] C. M. Ko and D. Seibert, What can we learn from a second  $\phi$  meson peak in ultrarelativistic nuclear collisions? *Phys. Rev.* **C49**, 2198 (1994)
- [24] U. Heinz and K. S. Lee, The  $\rho$  peak in the dimuon spectrum as a clock for fireball lifetimes in relativistic nuclear collisions. *Phys. Lett.* **B259**, 162 (1991)
- [25] T. Matsui and H. Satz,  $J/\psi$  suppression by Quark - Gluon Plasma formation. *Phys. Lett.* **B178**, 416 (1986)
- [26] S. E. Koonin, Proton pictures of high-energy nuclear collisions. *Phys. Lett.* **B70**, 43 (1977)
- [27] F. B. Yano and S. E. Koonin, Determining pion source parameters in relativistic heavy ion collisions. *Phys. Lett.* **B78**, 556 (1978)
- [28] S. Pratt, Pion Interferometry for Exploding Sources. *Phys. Rev. Lett.* **53**, 1219 (1984)
- [29] S. Pratt, Pion interferometry of Quark-Gluon Plasma. *Phys. Rev.* **D33**, 1314 (1986)
- [30] U. Heinz, How to extract physics from HBT radius parameters. *Nucl. Phys.* **A610**, 264c (1996)
- [31] R. Lednicky, V. L. Lyuboshitz, B. Erasmus, D. Nouais, How to measure which sort of particles was emitted earlier and which later. *Phys. Lett.* **B373**, 30 (1996)
- [32] G. Bertsch, Pion interferometry as a probe of the plasma. *Nucl. Phys.* **A498**, 173c (1989)
- [33] J. P. Bailly *et al.*, Strangeness and diquark suppression factors in 360-GeV/c p p interactions. *Phys. Lett* **B195**, 609 (1987)
- [34] P. K. Malhotra and R. Orava, Measurement of strange quark suppression in hadronic vacuum. *Z. Phys.* **C17**, 85 (1983)
- [35] M. Gluck and E. Reya, Duality predictions for the production of heavy quark systems in QCD. *Phys. Lett.* **B79**, 453 (1978)

- [36] T. Alberet *et al.*, Two pion Bose-Einstein correlations in nuclear collisions at 200-GeV per nucleon. *Z.Phys.* **C66**, 77 (1995)
- [37] A. N. Makhlin and Y. M. Sinyukov, Hydrodynamics of hadron matter under pion interferometric microscope. *Z.Phys.* **C39**, 69 (1988)
- [38] H. W. Barz, G. L. Friman, J. Knoll and H. Schulz, Flavor kinetics in an expanding Quark - Gluon Plasma. *Nucl. Phys.* **A484**, 661 (1988)
- [39] H. W. Barz, G. L. Friman, J. Knoll and H. Schulz, Strangeness production in ultrarelativistic heavy ion collisions: flavor kinetics 2. *Nucl. Phys.* **A519**, 831 (1988)
- [40] H. W. Barz, G. L. Friman, J. Knoll and H. Schulz, Production of  $\phi$ ,  $\rho$  and  $\omega$  mesons in the hadronization of a Quark - Gluon Plasma. *Phys.Lett.* **B254**, 315 (1991)
- [41] N. Xu *et al.*, NA44 collaboration, Hadron distributions - Recent Result from the CERN experiment NA44. *Los Alamos Preprint LA-UR-96-2580*, (1996)
- [42] V. Koch, Cold kaons from hot fireballs. *Nucl. Phys.* **A590**, 531c(1995)
- [43] H. Stöcker, A. A. Ogloblin and W. Greiner, Significance of temperature measurements in relativistic nuclear collisions. *Z. Phys.* **A303**, 259 (1981)
- [44] H. Kapusta, S. Pratt, L. Mc Lerran and H. v. Gersdorff, Correlation between transverse momentum and multiplicity for spherically exploding Quark - Gluon Plasmas. *Phys. Lett.* **B163**, 253 (1985)
- [45] J. v. Gersdorff, Exploding Quark - Gluon Plasma and correlation between energy density and mean transverse momentum. *Nucl. Phys.* **A461**, 251c (1987)
- [46] M. H. Thoma and M. Gyulassy, High P(t) probes of nuclear collisions. *Nucl. Phys.* **A538**, 37c (1991)
- [47] S. Mrowczynski, Energy loss of a high-energy parton in the Quark - Gluon Plasma. *Phys.Lett.* **B269**, 383 (1991)
- [48] Y. Koike and T. Matsui, Passage of high-energy partons through a Quark-Gluon Plasma. *Phys. Rev.* **D45**, 3237 (1992)
- [49] A. B. Migdal, *Sov. Phys. JETP* **5**, 527 (1957)
- [50] M. Gyulassy, I. Vitev, and X. N. Wang, High  $p_t$  Azimuthal Asymmetry in Noncentral A + A at RHIC. *Phy. Rev. Lett.* **86**, 2537 (2001).
- [51] L. D. Landau and E. M. Lifshitz, *Statistical Physics*. Pergamon Press, Oxford, third edition, (1980)
- [52] M. B. Tsang *et al.*, Deflection of nonequilibrium light particles by the nuclear mean field. *Phys. Rev Lett.* **57**, 559 (1986)
- [53] W. K. Wilson *et al.*, Azimuthal asymmetry in Ar+V collisions from E/A=35 to 85 MeV. *Phys. Rev.* **C41**, R1881 (1990)

- [54] M.B. Tsang *et al.*, Measurement of complex fragments and clues to the entropy production from 42-MeV/nucleon - 137-MeV/nucleon Ar + Au. *Phys. Rev. Lett* **51**, 1846 (1983)
- [55] C. B. Chitwood *et al.*, Light particle emission in 16 induced reactions on  $^{12}\text{C}$ ,  $^{27}\text{Al}$ , and  $^{197}\text{Au}$  at  $E/A=25$  MeV. *Phys. Rev.* **C34**, 858 (1986)
- [56] H. H. Gutbrod *et al.*, A new component of the collective flow in relativistic heavy ion collisions. *Phys. Lett.* **B216**, 267 (1989)
- [57] C. M. Hung and E. V. Shuryak, Hydrodynamics near the QCD Phase Transition: Looking for the Longest-Lived Fireball. *Phys. Rev. Lett.* **75**, 4003 (1995).
- [58] J. -Y. Ollitrault, Flow systematics from SIS to SPS energies. *Nucl. Phys.* **A638**, 195c (1998).
- [59] D.H. Rischke, Y. Pursun, J.A. Maruhn, H. Stöcker, and W. Greiner, The phase transition to the Quark - Gluon Plasma and its effects on hydrodynamic flow. *Heavy Ion Phys.* **1**, 309 (1995)
- [60] L. P. Csernai and D. Rohrlich, Third flow component as QGP signal. *Phys. Lett.* **B458**, 454 (1999)
- [61] M. M. Agarwal *et al.*, WA98 collaboration, Recent results on Pb+Pb collisions at 158 AGeV from the WA98 experiment at CERN. *Nucl. Phys.* **A638**, 147c (1998)
- [62] H. Appelshäuser *et al.*, NA49 collaboration, Recent results on central Pb+pb collisions from experiment NA49. *Nucl. Phys.* **A638**, 91c (1998)
- [63] F. Ceretto *et al.*, CERES collaboration, Hadron physics with ceres: spectra and collective flow. *Nucl. Phys.* **A638**, 467c (1998)
- [64] D. Keane *et al.*, Proceeding of the Fourth Nuclear Dynamics Workshop. Copper Mountain, Colorado, (1986)
- [65] J. Gosset *et al.*, Nuclear collective flow and charged-pion emission in Ne-nucleus collisions at  $E/A=800$  MeV. *Phys. Rev. Lett* **62**, 1251 (1989)
- [66] B. Adyasevich *et al.*, Universal proton rapidity distributions in high-energy nucleus nucleus collisions. *Nucl. Phys.* **B16**, 419c (1990)
- [67] S. A. Bass *et al.*, Is collective pion flow anticorrelated to nucleon flow? *Phys. Lett* **B302**, 381 (1993)
- [68] J. Barrette *et al.*, E877 Collaboration, Proton and pion production relative to the reaction plane in Au + Au collisions at 11A GeV/c. *Phys. Rev.* **C56**, 3254 (1997)
- [69] P. F. Kolb, J. Sollfrank, and U. Heinz, Anisotropic flow from AGS to LHC energies. *Phys. Lett.* **B459**, 667 (1999)
- [70] P. F. Kolb, J. Sollfrank, P. V. Ruuskanen, and U. Heinz, Hydrodynamic simulation of elliptic flow. *Nucl. Phys.* **A661**, 349c (1999)
- [71] S. A. Voloshin and A. M. Poskanzer, The physics of the centrality dependence of elliptic flow. *Phys. Lett. B* **474**, 27-32 2000

- [72] H. Sorge, Highly Sensitive Centrality Dependence of Elliptic Flow: A Novel Signature of the Phase Transition in QCD. *Phys. Rev. Lett.* **82**, 2048 (1999)
- [73] A. Bialas, M. Bleszynski, and W. Czyz, Multiplicity distributions in nucleus-nucleus collisions at high-energies. *Nucl. Phys.* **B111**, 461 (1976)
- [74] H. Heiselberg and A. -M. Levy, Elliptic flow and Hanbury-Brown-Twiss correlations in non-central nuclear collisions. *Phys. Rev.* **C59**, 2716 (1999).
- [75] P. F. Kolb, J. Sollfrank, U. Heinz, Anisotropic transverse flow and the quark-hadron phase transition. *Phys. Rev.* **C62**, 054909 (2000).
- [76] P. Danielewicz, Flow and the equation of state of nuclear matter. *e-print nucl-th/0009091* (2000).
- [77] P. Hovinen, P. F. Kolb, U. Heinz, P. V. Ruuskanen, S. A. Voloshin, Radial and elliptic flow at RHIC: further predictions. *Phys. Lett.* **B503**, 58 (2001).
- [78] STAR collaboration, K.H. Ackermann *et al.*, The STAR Time Projection Chamber. *Nucl. Phys.* **A661**, 681c (1999).
- [79] The STAR Collaboration, J. W. Harris *et al.*, The STAR experiment at the relativistic heavy ion collider. *Nucl. Phys.* **A566**, 277c (1994).
- [80] J. Seguinot *et al.*, A historical survey of ring imaging Cerenkov counters. *Nucl. Instr. and Meth.* **A343**, 1 (1994).
- [81] T. Ypsilantis *et al.*, Theory of ring imaging Cerenkov counters. *Nucl. Instr. and Meth.* **A343**, 30 (1994).
- [82] L. C. L. Yuan and C.-S. Wu, editors, Methods of Experimental Physics. Academic Press, 1961, Vol. 5A, p. 163
- [83] W.W.M. Allison and P.R.S. Wright, The Physics of Charged Particle Identification: dE/dx, Cerenkov Radiation, and Transition Radiation, p. 371 in *Experimental Techniques in High Energy Physics*, T. Ferbel, editor, (Addison-Wesley 1987)
- [84] L. Landau, On the energy loss of fast particles by ionization. *J. Phys.* **VIII**, 201 (1944)
- [85] D.E. Groom *et al.*, Particle Data Group, *Eur. Phys. Journal*, **C15:1**, (2000)
- [86] A. M. Poskanzer, Anisotropic Flow at the SPS and RHIC. *e-print nucl-ex/0110013* (2001).
- [87] H. Sorge, Elliptical Flow: A Signature for Early Pressure in Ultrarelativistic Nucleus-Nucleus Collisions. *Phys. Rev. Lett.* **78**, 2309 (1997).
- [88] N. Borghini, P. M. Dinh, and J. -Y. Ollitrault, New method for measuring azimuthal distributions in nucleus-nucleus collisions. *Phys. Rev.* **C63**, 054906 (2001).
- [89] N. Borghini, P. M. Dinh, and J. -Y. Ollitrault, Flow analysis from multiparticle azimuthal correlations. *Phys. Rev.* **C64**, 054901 (2001).

- [90] STAR collaboration, C. Adler *et al.*, Identified particle elliptic flow in Au+Au collisions at  $\sqrt{s_{NN}} = 130$  GeV. *Phys. Rev. Lett.* **87**, 182301 (2001).
- [91] P. Danielewicz and G. Odyniec, Transverse momentum analysis of collective motion in relativistic nuclear collisions. *Phys. Lett.* **B157**, 146 (1985)
- [92] P. Danielewicz, Effects of compression and collective expansion on particle emission from central heavy-ion reactions. *Phys. Rev.* **C51**, 716 (1995).
- [93] M. Gyulassy and X.-N. Wang, HIJING 1.0: A Monte Carlo program for parton and particle production in high-energy hadronic and nuclear collisions. *Comput. Phys. Commun.* **83**, 307 (1994);
- [94] X.N. Wang and M. Gyulassy, HIJING: A Monte Carlo model for multiple jet production in pp, pA, and AA collisions. *Phys. Rev.* **D44**, 3501 (1991).
- [95] A. M. Poskanzer and S. A. Voloshin, New Developments in Methods for Anisotropic Flow Analysis. *LBNL Annual Report* <http://ie.lbl.gov/nsd1999/rnc/RNC.htm> R34 (1998).
- [96] P. M. Dinh, N. Borghini and J.-Y. Ollitrault, Effects of HBT correlations on flow measurements. *Phys. Lett. B* **477**, 51 (2000).
- [97] N. Borghini, P. M. Dinh, and J. -Y. Ollitrault, Is the analysis of flow at the CERN Super Proton Synchrotron reliable? *Phys. Rev.* **C62**, 034902 (2000).
- [98] M. Biyajima, Physical meaning of a parameter of the degree of coherence in the modified Kopylov-Podgoretsky-Cocconi formulas: a number of jets versus an adjustable parameter. *Prog. Theor. Phys.* **66**, 1378 (1981).
- [99] R. L. Liboff, Dipole and higher multipole particle creation in the steady state universe. *The Astrophysical Journal* Part 1, vol. 431, no. 1, p. 69-73 (1994).
- [100] H. C. Eggers, P. Lipa, P. Carruthers, and B. Buschbeck, Integral correlation measures for multiparticle physics. *Phys. Rev.* **D48**, 2040 (48).
- [101] N. Borghini, P. M. Dinh, and J.-Y. Ollitrault, Flow analysis from cumulants: a practical guide. *e-print nucl-ex/0110016*.
- [102] R. L. Ray and R. S. Longacre, A Monte Carlo Event Generator for STAR. *e-print nucl-ex/0008009*.
- [103] T.Osada, C.E.Aguiar, Y.Hama, T.Kodama, Event-by-event analysis of ultra-relativistic heavy-ion collisions in smoothed particle. *e-print nucl-th/0102011*.
- [104] R. Snellings *et al.*, STAR collaboration, Elliptic flow in Au + Au collisions. *Quark Matter*, (2001).
- [105] P. Jacobs and G. Cooper, Spatial Distribution of Initial Interactions in High Energy Collisions of Heavy Nuclei. *e-print nucl-ex/0008015*.
- [106] A. M. Poskanzer and S. A. Voloshin, Centrality Dependence of Directed and Elliptic Flow at the SPS. *Nucl. Phys.* **A661**, 341c (1999).

- [107] J. Barrette *et al.*, E877 collaboration, Charged-particle pseudorapidity distributions in Au+Al, Cu, Au, and U collisions at 10.8A GeV/c. *Phys. Rev.* **C51**, 3309 (1995).
- [108] J. Barrette *et al.*, E877 collaboration, Energy and charged particle flow in 10.8A GeV/c Au+Au collisions. *Phys. Rev.* **C55**, 1420 (1997).
- [109] P. F. Kolb, P. Houvinen, U. Heinz, and H. Heiselberg, Elliptic Flow at SPS and RHIC: From Kinetic Transport to Hydrodynamics. *Phys. Lett. B* **500**, 232 (2001).
- [110] P. J. Siemens and J. O. Rasmussen Evidence for a Blast Wave from Compressed Nuclear Matter. *Phys. Rev. Lett.* **42**, 880 (1979).
- [111] M. Kaneta *et al.*, STAR collaboration, Internal STAR analysis meeting. (2001).
- [112] R. wells *et al.*, STAR collaboration, Internal STAR analysis meeting. (2002).
- [113] H. Zhang *et al.*, STAR collaboration, Internal STAR analysis meeting. (2002).
- [114] M. B. Tonjes *et al.*, STAR collaboration, Internal STAR analysis meeting. (2002).
- [115] K. Adcox *et al.*, PHEONIX collaboration, Suppression of Hadrons with Large Transverse Momentum in Central Au+Au Collisions at  $\sqrt{s_{NN}} = 130$  GeV. *Phys. Rev. Lett.* **88**, 022301 (2002).
- [116] P. Jacobs, *et al.*, STAR collaboration, Internal STAR analysis meeting. (2002).
- [117] C. Ogilvie Angular correlations of high  $p_t$  particles. Talk given at “high  $p_t$  phenomena at RHIC” workshop, Brookhaven National Lab, (2001).
- [118] A. Tang *et al.*, STAR collaboration, Flow and non-flow correlations from four-particle multiplets in STAR. *e-print* hep-ex/0108029.



## Appendix A

### The Quark Model

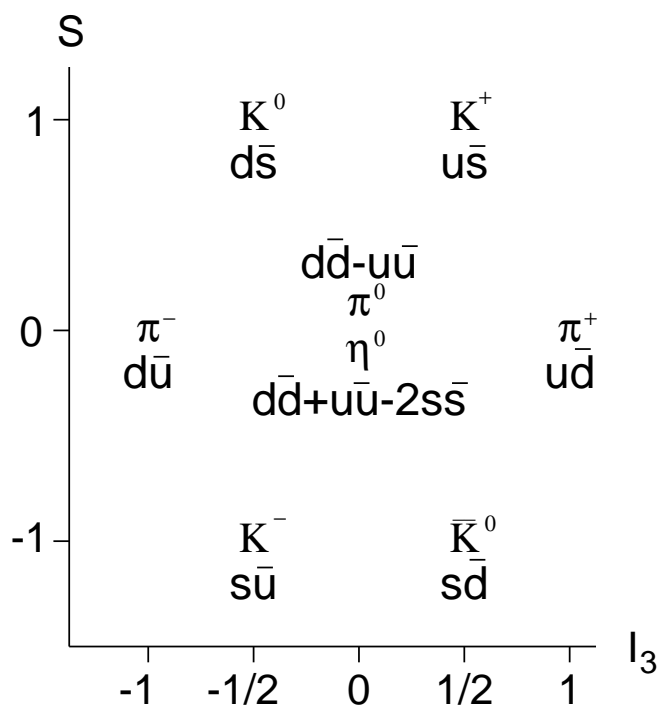
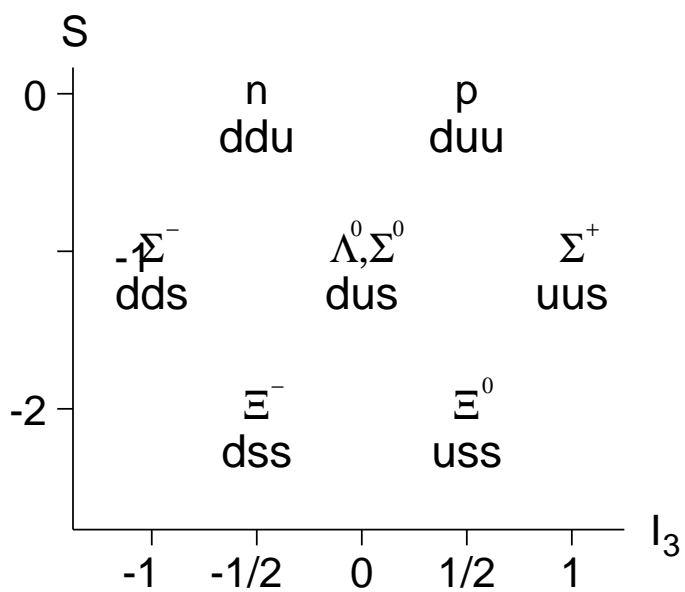
The quark model describes nucleons and other hadrons as consisting of quarks. Baryons, of which the nucleons are two examples, are made up of three quarks whereas mesons, such as pions, consist of a quark and an anti-quark. All hadrons, particles which are affected by the strong force, are thought to be combinations of three quarks, three anti-quarks or a quark with an anti-quark. The hadron spectrum can be accounted for by six flavours of quarks, which are listed in table A.1 with their quantum numbers. The two most massive quark flavours do not feature in heavy-ion collisions, at the energies presently available, due to their high masses.

Quarks are created in quark-anti-quark pairs of the same flavour. Flavour is conserved in the strong interaction but not in weak decays which occur on a much longer time-scale. Some mesons and baryons with their quark content are shown in figures A.1 & A.2.

Even after taking into account the spin of the quarks it would appear that some hadronic states, such as the  $\Delta^{++}$ , violate the Pauli exclusion principle. This resonance consists of three  $u$  quarks and has a spin of  $\frac{3}{2}$  so all three quarks appear to be in identical quantum states. This leads to the

Symbol	Name	Mass	Charge	Quantum no.
u	up	300 MeV	+	$I_3 = +\frac{1}{2}$
d	down	300 MeV	-	$I_3 = -\frac{1}{2}$
s	strange	500 MeV	-	S=-1
c	charm	1.2 GeV	+	C=+1
b	bottom	4.2 GeV	-	B=-1
t	top	170 GeV	+	T=+1

Table A.1: The six quark flavours and their approximate constituent masses.

Figure A.1: Meson octet with  $J^P = 0^-$ Figure A.2: Baryon octet with  $J^P = \frac{1}{2}^+$ .

introduction of a further quantum number which can take on three values for quarks (plus three opposite values for anti-quarks). This quantum number is labelled colour and the values have become known as red, green and blue. Thus, in the  $\Delta^{++}$  resonance the three  $u$  quarks each have a different colour quantum number. The complete Standard Model also includes the leptons and the bosons which mediate the forces. One of these is the gluon which is exchanged in the strong interaction just as electromagnetic interactions exchange photons. However, unlike the photon, the gluon carries the quanta of the force it is mediating. That is to say gluons have colour charge whereas photons do not possess electromagnetic charge. This property means that the gluons can interact amongst themselves leading to qualitative differences between the strong and electromagnetic forces. There are in fact an octet of gluons carrying the different combinations of the colour charge,  $r\bar{b}$ ,  $r\bar{g}$ ,  $b\bar{g}$ ,  $b\bar{r}$ ,  $g\bar{b}$ ,  $g\bar{r}$  and the mixtures  $(r\bar{r} - g\bar{g})/\sqrt{2}$ , and  $(r\bar{r} + g\bar{g} - 2b\bar{b})/\sqrt{6}$ . This scheme allows a quark of any colour to interact with another by exchanging the appropriate gluon.

## Appendix B

### Kinematic Variables

In relativistic heavy ion collisions, it is convenient to use kinematic variables that are Lorentz invariant or transform trivially under Lorentz boost.

Given the  $z$  axis as the direction of the beam, the  $p_t$  (transverse momentum) is defined as:

$$p_t = \sqrt{p_x^2 + p_y^2} . \quad (\text{B.1})$$

$p_t$  is a Lorentz invariant variable since both  $p_x$  and  $p_y$  are unchanged under a Lorentz boost along  $z$  axis.

For identified particles one usually employs the transverse mass

$$m_t = \sqrt{p_t^2 + m^2} , \quad (\text{B.2})$$

where  $m$  is the mass of the particle. The transverse energy of the particle is given by  $m_t - m$ .

In place of longitudinal momenta, it is normal to use the rapidity, defined as

$$y = \frac{1}{2} \ln \left( \frac{E + p_z}{E - p_z} \right) \quad (\text{B.3})$$

$$= \ln \left( \frac{E + p_z}{m_t} \right) \quad (\text{B.4})$$

$$= \tanh^{-1} \left( \frac{p_z}{E} \right) , \quad (\text{B.5})$$

where  $E$  and  $p_z$  are the energy and longitudinal momentum of the particle, respectively.

Under a Lorentz transformation from a reference system  $S$  to a system  $S'$  moving with velocity  $\beta_z$  with respect to  $S$  in the longitudinal direction, the rapidity  $y'$  in the  $S'$  frame is related to  $y$  in the  $S$  frame only by an additive constant:  $y' = y - y_\beta$ , where  $y_\beta$  is the rapidity of the moving frame.

$$y_\beta = \frac{1}{2} \ln \left( \frac{1 + \beta_z}{1 - \beta_z} \right) . \quad (\text{B.6})$$

The additive property of rapidity guarantees that the shape of the corresponding distribution is unchanged under Lorentz boost.

In the limit of  $p \gg m$  and  $p_z/p \gg 1/\gamma$ , the rapidity reduces to to be

$$y = \frac{1}{2} \ln \left( \frac{E + p_z}{E - p_z} \right) \approx \frac{1}{2} \ln \left( \frac{|\vec{p}| + p_z}{|\vec{p}| - p_z} \right) = \ln \left( \sqrt{\frac{1 + \cos \theta}{1 - \cos \theta}} \right) = -\ln (\tan \theta/2) \equiv \eta. \quad (\text{B.7})$$

where  $\eta$  is called pseudorapidity. Note that pseudorapidity, unlike rapidity, can be computed without knowing the mass of the particle.

## Appendix C

### Practical Guide to Cumulant Method in Flow Analysis

In this appendix, the cumulant method for anisotropic flow analysis will be described. The practical usage will be addressed, thus most equations will be presented without derivation. To see the derivation, refer to[89].

#### C.1 Integrated flow

We began with the construction of the real-valued generating function

$$\begin{aligned} G_n(z) &= \prod_{j=1} \left( 1 + \frac{w_j}{M} (z^* e^{in\phi_j} + z e^{-in\phi_j}) \right) \\ &= \prod_{j=1} \left( 1 + \frac{w_j}{M} (2x \cos(n\phi_j) + 2y \sin(n\phi_j)) \right), \end{aligned} \quad (\text{C.1})$$

where  $z^* \equiv x - iy$  denotes the complex conjugate. This generating function can then be averaged over events with the same multiplicity  $M$ . In practice, the variable  $z$  corresponds to interpolation points used to estimate the various quantities encountered in the analysis, and its usage will be clear shortly.

In order to obtain the cumulants, one first averages  $G_n(z)$  over events, which yields an average generating function  $\langle G_n(z) \rangle$ . Then the cumulant  $\mathcal{C}_n(z)$  is defined as

$$\mathcal{C}_n(z) \equiv M \left( \langle G_n(z) \rangle^{1/M} - 1 \right). \quad (\text{C.2})$$

The cumulant of  $2k$ -particle correlations  $\mathcal{C}_n(2k)$  is the coefficient of  $z^{*k} z^k / (k!)^2$  in the power-series expansion of  $\mathcal{C}_n(z)$ . To construct the first three cumulants, one may truncate the series to order  $|z^6|$  and compute  $\mathcal{C}_n(z)$  at the following interpolation points:

$$z_{p,q} \equiv x_{p,q} + iy_{p,q}, \quad x_{p,q} \equiv r_0 \sqrt{p} \cos\left(\frac{2q\pi}{q_{\max}}\right), \quad y_{p,q} \equiv r_0 \sqrt{p} \sin\left(\frac{2q\pi}{q_{\max}}\right). \quad (\text{C.3})$$

for  $p = 1, 2, 3$  and  $q = 0, \dots, q_{\max} - 1$ , where  $q_{\max} \geq 8$ . The parameter  $r_0$  must be chosen as a compromise between errors due to higher order terms in the power-series expansion, which rapidly increase with  $r_0$ , and numerical errors. For the flow analysis in this dissertation, 1.5 is used for  $r_0$ .

Once the values  $\mathcal{C}_n(z_{p,q})$  have been computed, they must be averaged over the phase of  $z$ :

$$C_p \equiv \frac{1}{q_{\max}} \sum_{q=0}^{q_{\max}-1} \mathcal{C}_n z_{p,q}, \quad p = 1, 2, 3. \quad (\text{C.4})$$

The cumulants from 2, 4, and 6 particle correlation are then given respectively by

$$\begin{aligned} c_n\{2\} &= \frac{1}{r_0^2} \left( 3C_1 - \frac{3}{2}C_2 + \frac{1}{3}C_3 \right), \\ c_n\{4\} &= \frac{2}{r_0^4} (-5C_1 + 4C_2 - C_3), \\ c_n\{6\} &= \frac{6}{r_0^6} (3C_1 - 3C_2 + C_3). \end{aligned} \quad (\text{C.5})$$

Then the weighted integrated flow (defined as  $V_n \equiv \langle w e^{in(\phi - \Phi_R)} \rangle$ ) relates to the cumulants by:

$$V_n\{2\}^2 = c_n\{2\}, \quad V_n\{4\}^4 = -c_n\{4\}, \quad V_n\{6\}^6 = c_n\{6\}/4. \quad (\text{C.6})$$

## C.2 Differential flow

The differential flow is the flow from a sub-ensemble of a total ensemble. It could be flow from particles within a  $p_t$  and  $\eta$  window, or flow from a specific particle type. For the sake of simplicity, let's say those particles for differential flow study are protons with azimuthal angle denoted by  $\psi$ , while particles used for studying integrated flow are pions (with azimuthal angle denoted by  $\phi$ ).

We are able to measure flow via particle correlation because  $\langle e^{in(\psi_i - \phi_j)} \rangle$  is a non-zero value, where  $n$  is the harmonic. This condition can be rewritten as  $\langle e^{in(m\psi_i - \phi_1 - \phi_2 - \dots - \phi_m)} \rangle \neq 0$ , which means we correlate  $m$  pions with harmonic  $n$  to get the flow of protons with harmonic  $m \times n$ . For example, we can measure  $v_2$  from proton by

$$v_2 = \langle e^{i(2\psi - \phi_i - \phi_j)} \rangle, \quad (\text{C.7})$$

which is based on three-particle correlation (2 pions and 1 proton) and mixed harmonics (first harmonic for pions, second harmonic for protons).

In order to take such cases into account, an index  $m$  is introduced in the subscripts for differential flow. For instance,  $v_{mn/n}$  means differential flow from correlating one proton with harmonic  $m \times n$  with  $m$  pions with harmonic  $n$ . Then we have two ways to get  $v_2$  from protons: one way is  $(v_{2/2}\{3\})$ , where we correlate one proton with one pion, both in the second harmonic, and the other way is  $(v_{2/1}\{3\})$ , where we correlate one second harmonic proton with two pions in the first harmonic.

The cumulant for differential flow is given by

$$\mathcal{D}_{mn/n}(z) \equiv \frac{\langle e^{imn\psi} G_n(z) \rangle}{\langle G_n(z) \rangle}, \quad (\text{C.8})$$

where the numerator is evaluated over all protons, and the denominator is averaged over all events (it can be obtained from the calculation of integrated flow). If the proton was used in the calculation of the generating function Eq. C.1, one should divide  $G_n(z)$  by  $1 + w_j(z^* e^{im\psi} + z e^{-in\psi})/M$ , where  $\psi$  is the proton azimuthal angle, to avoid autocorrelations.

To extract the cumulants, one computes the product  $z^{*m} \mathcal{D}_{mn/n}(z)$  at the points  $z_{p,q}$ , Eq. C.3; one then takes the real part, and averages over angles:



$$D_p \equiv \frac{(r_0 \sqrt{p})^m}{q_{\max}} \sum_{q=0}^{q_{\max}-1} \left[ \cos \left( m \frac{2q\pi}{q_{\max}} \right) X_{p,q} + \sin \left( m \frac{2q\pi}{q_{\max}} \right) Y_{p,q} \right], \quad (\text{C.9})$$

with  $p = 1, 2, 3$  and  $X_{p,q} + iY_{p,q} \equiv \mathcal{D}_{mn/m}(z_{p,q})$ .

For  $m = 1$  (no harmonic mixed), the lowest order cumulants are given by

$$\begin{aligned} d_{n/n}\{2\} &= \frac{1}{r_0^2} \left( 2D_1 - \frac{1}{2}D_2 \right), \\ d_{n/n}\{4\} &= \frac{1}{r_0^4} (-2D_1 + D_2), \end{aligned} \quad (\text{C.10})$$

while for  $m = 2$  (mixed harmonic),

$$\begin{aligned} d_{2n/n}\{3\} &= \frac{1}{r_0^4} \left( 4D_1 - \frac{1}{2}D_2 \right), \\ d_{2n/n}\{5\} &= \frac{1}{r_0^6} \left( -6D_1 + \frac{3}{2}D_2 \right). \end{aligned} \quad (\text{C.11})$$

These cumulants must then be related to the differential flow. For a perfect detector,

$$v_{n/n}\{2\} = d_{n/n}\{2\}/V_n, \quad v_{n/n}\{4\} = -d_{n/n}\{4\}/V_n^3, \quad (\text{C.12})$$

$$v_{2n/n}\{3\} = d_{2n/n}\{3\}/V_n^2, \quad v_{2n/n}\{5\} = -d_{2n/n}\{5\}/(2V_n^4). \quad (\text{C.13})$$

## Appendix D

### **Author's Contributions to Collaborative Research**

In addition to the physics analysis work described in this dissertation, I have completed a number of “community service” tasks within the STAR collaboration, i.e., tasks that are of benefit to part or all of the entire collaboration and were not a necessary step in carrying out my own physics analysis. I have participated in the installation and testing of the High Voltage supply system for the anode wires of the STAR TPC. During STAR testing in 1999, and data-taking in 2000 and 2001, I manned many additional shifts in the STAR control room beyond the normal allocation expected from each collaborator.

In the area of community service software, I have studied the details of charged particle energy loss ( $dE/dx$ ) in the TPC, including various systematic effects arising from imperfections in the  $dE/dx$  response of the TPC. These studies led to optimum calibration of the  $dE/dx$  signal, and improved the  $dE/dx$  resolution by 13% relative to the case where the imperfections were neglected. This improved resolution directly leads to improved particle identification (PID) in the TPC, and the same amount of improvement by a hardware approach could easily cost on the order of \$1 million. This  $dE/dx$  study is summarized in Chapter 6 of the dissertation. I also developed a software tool for extracting the maximum possible PID information from the  $dE/dx$  signal, and this tool is widely adopted in various physics analyses in STAR.

I participated in the analysis of elliptic flow for the three most abundant species of identified charged particles (pions, kaons and protons) and I am one of the principal authors of a paper on this topic, which has been published in Physical Review Letters [90] (this is the most prestigious journal of the American Physical Society, and publishes important findings from across the entire field of physics). More recently, I have carried out a systematic elliptic flow study using four-particle

correlations — the main topic of this dissertation. The same analysis procedure will be followed in future flow analyses in the STAR experiment, because the only significant disadvantage of this approach is its larger statistical errors, and this is not likely to be of concern in the future because the number of events will be very large. Other heavy-ion experiments will benefit from this work as well. A long paper based on the main content of this dissertation is now approaching the final stage of internal review within the STAR collaboration, and it will soon be submitted for journal publication.

I have presented invited talks on this work at two major conferences — the International Nuclear Physics Conference (INPC 2001) in Berkeley, CA (June 2001), and at the 2001 annual meeting of the American Chemical Society in Chicago (August 2001). I am the sole explicit author of the written proceedings of INPC 2001 [118].

My list of publications can be found in Appendix E. STAR policy, following the normal practice of large collaborations in High Energy and Nuclear Physics, lists all authors on refereed publications strictly in alphabetical order. I am among the principal authors for papers marked with “\*”.

## Appendix E

### List of Publications

- *Elliptic Flow in Au+Au Collisions at  $\sqrt{s_{NN}} = 130$  GeV,*  
K.H. Ackermann *et al.* (STAR Collaboration) Phys. Rev. Lett. **86**, 402 (2001)
- *Mid-rapidity anti-proton to proton ratio from Au+Au Collisions at  $\sqrt{s_{NN}} = 130$  GeV,*  
C. Adler *et al.* (STAR Collaboration) Phys. Rev. Lett. **86**, 4778 (2001)
- *Pion Interferometry Analysis of  $\sqrt{s_{NN}} = 130$  GeV Au+Au Collisions at RHIC,*  
C. Adler *et al.* (STAR Collaboration) Phys. Rev. Lett. **87**, 082301 (2001)
- *Multiplicity distribution and spectra of negatively charged hadrons in Au+Au collisions at  $\sqrt{s_{NN}} = 130$  GeV,*  
C. Adler *et al.* (STAR Collaboration) Phys. Rev. Lett. **87**, 112303 (2001)
- *\*Identified Particle Elliptic Flow in Au+Au Collisions at  $\sqrt{s_{NN}} = 130$  GeV,*  
C. Adler *et al.* (STAR Collaboration) Phys. Rev. Lett. **87**, 182301 (2001)
- *Mid-rapidity phi production in Au+Au collisions at  $\sqrt{s_{NN}} = 130$  GeV,*  
C. Adler *et al.* (STAR Collaboration) accepted by Phys. Rev. C.
- *Antideuteron and Antihelium production in Au+Au collisions at  $\sqrt{s_{NN}} = 130$  GeV,*  
C. Adler *et al.* (STAR Collaboration) Phys. Rev. Lett. **87**,262301-1 (2001)
- *Measurement of inclusive antiprotons from Au+Au collisions at  $\sqrt{s_{NN}} = 130$  GeV,*  
C. Adler *et al.* (STAR Collaboration) Phys. Rev. Lett. **87**,262302-1 (2001)

- *Mid-rapidity Lambda and Lambda bar Production in Au + Au Collisions at  $\sqrt{s_{NN}} = 130$  GeV,*  
C. Adler *et al.* (STAR Collaboration) to be submitted to Phys. Rev. Lett.
- *\*Elliptic flow from two- and four- particle correlations in Au + Au Collisions at  $\sqrt{s_{NN}} = 130$  GeV,*  
C. Adler *et al.* (STAR Collaboration) to be submitted to Phys. Rev. C.

## Appendix F

### The STAR Collaboration

C. Adler<sup>11</sup>, Z. Ahammed<sup>23</sup>, C. Allgower<sup>12</sup>, J. Amonett<sup>14</sup>, B.D. Anderson<sup>14</sup>, M. Anderson<sup>6</sup>, G.S. Averichev<sup>9</sup>, J. Balewski<sup>12</sup>, O. Barannikova<sup>9,23</sup>, L.S. Barnby<sup>14</sup>, J. Baudot<sup>13</sup>, S. Bekele<sup>20</sup>, V.V. Belaga<sup>9</sup>, R. Bellwied<sup>31</sup>, J. Berger<sup>11</sup>, H. Bichsel<sup>30</sup>, L.C. Bland<sup>12</sup>, C.O. Blyth<sup>3</sup>, B.E. Bonner<sup>24</sup>, A. Boucham<sup>26</sup>, A. Brandin<sup>18</sup>, R.V. Cadman<sup>1</sup>, H. Caines<sup>26</sup>, M. Calderón de la Barca Sánchez<sup>33</sup>, A. Cardenas<sup>23</sup>, J. Carroll<sup>16</sup>, J. Castillo<sup>26</sup>, M. Castro<sup>31</sup>, D. Cebra<sup>6</sup>, S. Chattopadhyay<sup>31</sup>, M.L. Chen<sup>2</sup>, Y. Chen<sup>6</sup>, S.P. Chernenko<sup>9</sup>, M. Cherney<sup>8</sup>, A. Chikanian<sup>33</sup>, B. Choi<sup>28</sup>, W. Christie<sup>2</sup>, J.P. Coffin<sup>13</sup>, T.M. Cormier<sup>31</sup>, J.G. Cramer<sup>30</sup>, H.J. Crawford<sup>4</sup>, W.S. Deng<sup>2</sup>, A.A. Derevschikov<sup>22</sup>, L. Didenko<sup>2</sup>, T. Dietel<sup>11</sup>, J.E. Draper<sup>6</sup>, V.B. Dunin<sup>9</sup>, J.C. Dunlop<sup>33</sup>, V. Eckardt<sup>16</sup>, L.G. Efimov<sup>9</sup>, V. Emelianov<sup>18</sup>, J. Engelage<sup>4</sup>, G. Eppley<sup>24</sup>, B. Erazmus<sup>26</sup>, P. Fachini<sup>2</sup>, V. Faine<sup>2</sup>, K. Filimonov<sup>16</sup>, E. Finch<sup>33</sup>, Y. Fisyak<sup>2</sup>, D. Flierl<sup>11</sup>, K.J. Foley<sup>2</sup>, J. Fu<sup>16</sup>, C.A. Gagliardi<sup>27</sup>, N. Gagunashvili<sup>9</sup>, J. Gans<sup>33</sup>, L. Gaudichet<sup>26</sup>, M. Germain<sup>13</sup>, F. Geurts<sup>24</sup>, V. Ghazikhanian<sup>6</sup>, O. Grachov<sup>31</sup>, V. Grigoriev<sup>18</sup>, M. Guedon<sup>13</sup>, E. Gushin<sup>18</sup>, T.J. Hallman<sup>2</sup>, D. Hardtke<sup>16</sup>, J.W. Harris<sup>33</sup>, S. Heppelmann<sup>21</sup>, T. Herston<sup>23</sup>, B. Hippolyte<sup>13</sup>, A. Hirsch<sup>23</sup>, E. Hjort<sup>16</sup>, G.W. Hoffmann<sup>28</sup>, M. Horsley<sup>33</sup>, H.Z. Huang<sup>6</sup>, T.J. Humanic<sup>20</sup>, G. Igo<sup>6</sup>, A. Ishihara<sup>28</sup>, Yu.I. Ivanshin<sup>10</sup>, P. Jacobs<sup>16</sup>, W.W. Jacobs<sup>12</sup>, M. Janik<sup>29</sup>, I. Johnson<sup>16</sup>, P.G. Jones<sup>3</sup>, E.G. Judd<sup>4</sup>, M. Kaneta<sup>16</sup>, M. Kaplan<sup>7</sup>, D. Keane<sup>14</sup>, J. Kiryluk<sup>6</sup>, A. Kisiel<sup>29</sup>, J. Klay<sup>16</sup>, S.R. Klein<sup>16</sup>, A. Klyachko<sup>12</sup>, A.S. Konstantinov<sup>23</sup>, M. Kopytine<sup>14</sup>, L. Kotchenda<sup>18</sup>, A.D. Kovalenko<sup>9</sup>, M. Kramer<sup>19</sup>, P. Kravtsov<sup>18</sup>, K. Krueger<sup>1</sup>, C. Kuhn<sup>13</sup>, A.I. Kulikov<sup>9</sup>, G.J. Kunde<sup>23</sup>, C.L. Kunz<sup>7</sup>, R.Kh. Kutuev<sup>10</sup>, A.A. Kuznetsov<sup>9</sup>, L. Lakehal-Ayat<sup>26</sup>, M.A.C. Lamont<sup>3</sup>, J.M. Landgraf<sup>2</sup>, S. Lange<sup>11</sup>, C.P. Lansdel<sup>28</sup>, B. Lasiuk<sup>33</sup>, F. Laue<sup>2</sup>, A. Lebedev<sup>2</sup>, R. Lednicky<sup>9</sup>, V.M. Leontiev<sup>22</sup>, M.J. LeVine<sup>2</sup>, Q. Li<sup>31</sup>, S.J. Lindenbaum<sup>18</sup>, M.A. Lisa<sup>20</sup>, F. Liu<sup>22</sup>, L. Liu<sup>32</sup>, Z. Liu<sup>32</sup>, Q.J. Liu<sup>30</sup>, T. Ljubicic<sup>2</sup>, W.J. Llope<sup>24</sup>, G. LoCurto<sup>16</sup>, H. Long<sup>6</sup>, R.S. Longacre<sup>2</sup>, M. Lopez-Noriega<sup>20</sup>, W.A. Love<sup>2</sup>, D. Lynn<sup>2</sup>, R. Majka<sup>33</sup>, S. Margetis<sup>14</sup>, C. Markert<sup>33</sup>, L. Martin<sup>26</sup>, J. Marx<sup>16</sup>, H.S. Matis<sup>16</sup>, Yu.A. Matulenko<sup>22</sup>, T.S. McShane<sup>8</sup>, F. Meissner<sup>16</sup>, Yu. Melnick<sup>22</sup>, A. Meschanin<sup>22</sup>, M. Messer<sup>2</sup>, M.L. Miller<sup>33</sup>, Z. Milosevich<sup>7</sup>, N.G. Minaev<sup>22</sup>, J. Mitchell<sup>24</sup>, V.A. Moiseenko<sup>10</sup>, C.F. Moore<sup>28</sup>, V. Morozov<sup>16</sup>, M.M. de Moura<sup>31</sup>, M.G. Munhoz<sup>26</sup>, J.M. Nelson<sup>3</sup>, P. Nevski<sup>2</sup>, V.A. Nikitin<sup>10</sup>, L.V. Nogach<sup>22</sup>, B. Norman<sup>14</sup>, S.B. Nurushev<sup>22</sup>, G. Odyniec<sup>16</sup>, A. Ogawa<sup>21</sup>, V. Okorokov<sup>18</sup>, M. Oldenburg<sup>16</sup>, D. Olson<sup>16</sup>, G. Paic<sup>20</sup>, S.U. Pandey<sup>31</sup>, Y. Panebratsev<sup>9</sup>, S.Y. Panitkin<sup>2</sup>, A.I. Pavlinov<sup>31</sup>, T. Pawlak<sup>29</sup>, V. Perevoztchikov<sup>2</sup>, W. Peryt<sup>29</sup>, V.A. Petrov<sup>10</sup>, J. Pluta<sup>29</sup>, N. Porile<sup>23</sup>, J. Porter<sup>2</sup>, A.M. Poskanzer<sup>16</sup>, E. Potrebenikova<sup>9</sup>, D. Prindle<sup>30</sup>, C. Pruneau<sup>31</sup>, J. Putschke<sup>16</sup>, G. Rai<sup>16</sup>, O. Ravel<sup>26</sup>, R.L. Ray<sup>28</sup>, S.V. Razin<sup>9,12</sup>, D. Reichhold<sup>8</sup>, J.G. Reid<sup>30</sup>, F. Retiere<sup>16</sup>, A. Ridiger<sup>18</sup>, H.G. Ritter<sup>16</sup>, J.B. Roberts<sup>24</sup>, O.V. Rogachevski<sup>9</sup>, J.L. Romero<sup>6</sup>, C. Roy<sup>26</sup>, V. Rykov<sup>31</sup>, I. Sakrejda<sup>16</sup>, S. Salur<sup>33</sup>, J. Sandweiss<sup>33</sup>, A.C. Saulys<sup>2</sup>, I. Savin<sup>10</sup>, J. Schambach<sup>28</sup>, R.P. Scharenberg<sup>23</sup>, N. Schmitz<sup>16</sup>, L.S. Schroeder<sup>16</sup>, A. Schütttauf<sup>16</sup>, K. Schweda<sup>16</sup>, J. Seger<sup>9</sup>, D. Seliverstov<sup>18</sup>, P. Seyboth<sup>16</sup>, E. Shahaliev<sup>9</sup>, K.E. Shestermanov<sup>22</sup>, S.S. Shimanski<sup>9</sup>, V.S. Shvetcov<sup>10</sup>, G. Skoro<sup>9</sup>, N. Smirnov<sup>33</sup>, R. Snellings<sup>16</sup>, P. Sorensen<sup>6</sup>, J. Sowinski<sup>12</sup>, H.M. Spinka<sup>1</sup>, B. Srivastava<sup>23</sup>, E.J. Stephenson<sup>12</sup>, R. Stock<sup>11</sup>, A. Stolpovsky<sup>31</sup>, M. Strikhanov<sup>18</sup>, B. Stringfellow<sup>23</sup>, C. Struck<sup>11</sup>, A.A.P. Suaide<sup>31</sup>, E. Sugarbaker<sup>20</sup>, C. Suire<sup>13</sup>, M. Šumbera<sup>20</sup>, T.J.M. Symons<sup>16</sup>, A. Szanto de Toledo<sup>26</sup>, P. Szarwas<sup>29</sup>, A. Tai<sup>6</sup>, J. Takahashi<sup>26</sup>, A.H. Tang<sup>14</sup>, J.H. Thomas<sup>16</sup>, M. Thompson<sup>3</sup>, V. Tikhomirov<sup>18</sup>, M. Tokarev<sup>9</sup>, M.B. Tonjes<sup>17</sup>, T.A. Trainor<sup>30</sup>, S. Trentalange<sup>6</sup>, R.E. Tribble<sup>27</sup>, V. Trofimov<sup>18</sup>, O. Tsai<sup>6</sup>, K. Turner<sup>2</sup>, T. Ullrich<sup>2</sup>, D.G. Underwood<sup>1</sup>, G. Van Buren<sup>2</sup>, A.M. VanderMolen<sup>17</sup>, I.M. Vasilevski<sup>10</sup>, A.N. Vasiliev<sup>22</sup>, S.E. Vigdor<sup>12</sup>, S.A. Voloshin<sup>31</sup>, F. Wang<sup>23</sup>, H. Ward<sup>28</sup>, J.W. Watson<sup>14</sup>, R. Wells<sup>20</sup>, T. Wenaus<sup>2</sup>, G.D. Westfall<sup>17</sup>, C. Whitten Jr.<sup>6</sup>, H. Wieman<sup>16</sup>, R. Willson<sup>20</sup>, S.W. Wissink<sup>12</sup>, R. Witt<sup>32</sup>, J. Wood<sup>6</sup>, N. Xu<sup>16</sup>, Z. Xu<sup>2</sup>, A.E. Yakutin<sup>22</sup>, E. Yamamoto<sup>16</sup>, J. Yang<sup>6</sup>, P. Yepes<sup>24</sup>, V.I. Yurevich<sup>9</sup>, Y.V. Zanevski<sup>9</sup>, I. Zborovsky<sup>9</sup>, H. Zhang<sup>33</sup>, W.M. Zhang<sup>14</sup>, R. Zoulkarneev<sup>10</sup>, A.N. Zubarev<sup>9</sup>

- <sup>1</sup> Argonne National Laboratory, Argonne, Illinois 60439,  
<sup>2</sup> Brookhaven National Laboratory, Upton, New York 11973,  
<sup>3</sup> University of Birmingham, Birmingham, United Kingdom,  
<sup>4</sup> University of California, Berkeley, California 94720,  
<sup>5</sup> University of California, Davis, California 95616,  
<sup>6</sup> University of California, Los Angeles, California 90095,  
<sup>7</sup> Carnegie Mellon University, Pittsburgh, Pennsylvania 15213,  
<sup>8</sup> Creighton University, Omaha, Nebraska 68178,  
<sup>9</sup> Laboratory for High Energy (JINR), Dubna, Russia,  
<sup>10</sup> Particle Physics Laboratory (JINR), Dubna, Russia,  
<sup>11</sup> University of Frankfurt, Frankfurt, Germany,  
<sup>12</sup> Indiana University, Bloomington, Indiana 47408,  
<sup>13</sup> Institut de Recherches Subatomiques, Strasbourg, France,  
<sup>14</sup> Kent State University, Kent, Ohio 44242,  
<sup>15</sup> Lawrence Berkeley National Laboratory, Berkeley, California 94720,  
<sup>16</sup> Max-Planck-Institut fuer Physik, Munich, Germany,  
<sup>17</sup> Michigan State University, East Lansing, Michigan 48824,  
<sup>18</sup> Moscow Engineering Physics Institute, Moscow Russia,  
<sup>19</sup> City College of New York, New York City, New York 10031,  
<sup>20</sup> Ohio State University, Columbus, Ohio 43210,  
<sup>21</sup> Pennsylvania State University, University Park, Pennsylvania 16802,  
<sup>22</sup> Institute of High Energy Physics, Protvino, Russia,  
<sup>23</sup> Purdue University, West Lafayette, Indiana 47907,  
<sup>24</sup> Rice University, Houston, Texas 77251,  
<sup>25</sup> Universidade de Sao Paulo, Sao Paulo, Brazil,  
<sup>26</sup> SUBATECH, Nantes, France,  
<sup>27</sup> Texas A & M, College Station, Texas 77843,  
<sup>28</sup> University of Texas, Austin, Texas 78712,  
<sup>29</sup> Warsaw University of Technology, Warsaw, Poland,  
<sup>30</sup> University of Washington, Seattle, Washington 98195,  
<sup>31</sup> Wayne State University, Detroit, Michigan 48201,  
<sup>32</sup> Institute of Particle Physics, Wuhan, Hubei 430079 China, and  
<sup>33</sup> Yale University, New Haven, Connecticut 06520